INFRARED SIGNATURE MODIFICATIONS.   VOLUME I

.

PHYSICAL SCIENCES, INCORPORATED

PREPARED FOR

AIR FORCE OFFICE OF SCIENTIFIC RESEARCH

MARCH 1976
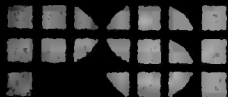
ADA024653

INFRARED SIGNATURE MODIFICATIONS

FINAL REPORT

VOLUME I

G. E. Caledonia

March 1976

D D C
RECEIVED
MAY 12 1976
B

Jointly Sponsored by

PHYSICAL SCIENCES INC.

18 LAKESIDE OFFICE PARK, WAKEFIELD, MASSACHUSETTS

DISCLAIMER NOTICE

THIS DOCUMENT IS BEST QUALITY AVAILABLE. THE COPY FURNISHED TO DTIC CONTAINED A SIGNIFICANT NUMBER OF PAGES WHICH DO NOT REPRODUCE LEGIBLY.

SECURITY CLASSIFICATION OF THIS PAGE (When Data Entered)

REPORT DOCUMENTATION PAGE	READ INSTRUCTIONS BEFORE COMPLETING FORM

1. REPORT NUMBER	2. GOVT ACCESSION NO.	3. RECIPIENT'S CATALOG NUMBER
AFOSR TR - 76 - 0436		

4. TITLE (and Subtitle)	5. TYPE OF REPORT & PERIOD COVERED
INFRARED SIGNATURE MODIFICATIONS Volume I	FINAL 1 Jan 75 - 31 Jan 76
	6. PERFORMING ORG. REPORT NUMBER PSI TR-48

7. AUTHOR(s)	8. CONTRACT OR GRANT NUMBER(s)
GEORGE E CALEDONIA	F44620-75-C-0039

9. PERFORMING ORGANIZATION NAME AND ADDRESS	10. PROGRAM ELEMENT, PROJECT, TASK AREA & WORK UNIT NUMBERS
PHYSICAL SCIENCES INC 18 LAKESIDE OFFICE PARK WAKEFIELD, MA 01880	681308 9711-02 61102F

11. CONTROLLING OFFICE NAME AND ADDRESS	12. REPORT DATE
AIR FORCE OFFICE OF SCIENTIFIC RESEARCH/NA BUILDING 410 BOLLING AIR FORCE BASE, D C 20332	March 1976
	13. NUMBER OF PAGES 95

14. MONITORING AGENCY NAME & ADDRESS(If different from Controlling Office)	15. SECURITY CLASS. (of this report)
	UNCLASSIFIED
	15a. DECLASSIFICATION DOWNGRADING SCHEDULE

16. DISTRIBUTION STATEMENT (of this Report)

Approved for public release; distribution unlimited.

17. DISTRIBUTION STATEMENT (of the abstract entered in Block 20, if different from Report)

18. SUPPLEMENTARY NOTES

19. KEY WORDS (Continue on reverse side if necessary and identify by block number)

WAKES	Al_2O_3
INFRARED RADIATION	
CHEMICAL KINETICS	C
VIBRATIONAL KINETICS	
PARTICULATES	ZrO_2

20. ABSTRACT (Continue on reverse side if necessary and identify by block number)
This report deals with the prediction of non-equilibrium infrared radiation signatures in the wakes of re-entry vehicles. The first section deals with the prediction of non-LTE wake molecular radiation for ablating vehicles. The second section discusses the radiation signatures which can result from the injection of small particles into the wakes.

DD FORM 1 JAN 73 1473 EDITION OF 1 NOV 65 IS OBSOLETE

PSI TR-48

INFRARED SIGNATURE MODIFICATIONS

FINAL REPORT

VOLUME I

G. E. Caledonia

March 1976

//

ABSTRACT

This report deals with the prediction of non-equilibrium infrared radiation signatures in the wakes of re-entry vehicles. The first section deals with the prediction of non-LTE wake molecular radiation for ablating vehicles. The second section discusses the radiation signatures which can result from the injection of small particles into the wakes.

SPONSORSHIP ACKNOWLEDGEMENT

TABLE OF CONTENTS

Preceding page blank

LIST OF ILLUSTRATIONS

LIST OF ILLUSTRATIONS (Cont.)

LIST OF ILLUSTRATIONS (Cont.)

I. INTRODUCTION

The general subject of this report is the prediction of non-equilibrium infrared radiation signatures in the wakes of re-entry vehicles. The subject matter presented is broken into two distinct parts. The first, presented in Section II, deals specifically with the prediction of non-equilibrium wake radiative histories of ablating vehicles. A vibrational and chemical kinetic scheme appropriate for vehicles with heat shields composed of the elements carbon, hydrogen and fluorine is presented. Detailed, two-dimensional, non-equilibrium radiation predictions for both laminar and turbulent wakes are provided for a generic re-entry vehicle over the altitude range of 69 - 38 km. The relationship between the predicted radiative behavior and the non-equilibrium vibrational and chemical kinetics is discussed.

In Section III the radiative behaviour which can result from the injection of small particles into the wake is examined. A model is developed to describe the interaction between the particles and wake molecules. The model, valid in the limit of free molecular flow, includes the phenomena of gas/particle collision dynamics, vaporization and radiative losses. The model is then exercised for typical particle materials and sizes in order to elucidate the importance of the gas/particle interaction to both spoofing and masking applications.

II. INFRARED WAKE RADIATION SIGNATURES OF ABLATING RE-ENTRY VEHICLES

A. Introduction

In recent years considerable effort has been directed towards the prediction of the infrared radiation histories of the wakes of ablating vehicles. Such predictions were initially performed[1] under the assumptions of frozen wake chemistry and vibrational/translation equilibration. More recently[2,3] detailed predictions have been provided which include the effects of non-equilibrium vibrational and chemical kinetics. These latter calculations have been limited to laminar wakes and did not include the appropriate vibrational kinetics for HF, a species which can be of some importance for specific heat shield combinations.

This section is concerned with the details of the techniques used in performing such calculations and the generic dependences of wake infrared histories on such parameters as altitude and ablation products. The basic model used for the calculations is described in Sec. B. Specific vibrational/chemical/radiative predictions for a "typical" re-entry vehicle are presented in Sec. C along with an overview of kinetic considerations.

B. Modeling

A basic computer code package used for the prediction of laminar wake infrared radiation histories has been developed over the last several years and has recently been documented in some detail.[3] The basic input to this package is the ablation history for a specified trajectory of the re-entry vehicle of interest. A series of computer codes are then used to determine the flux of the various chemical species which enter the wake, with the individual species concentrations being determined through use of a partial equilibrium boundary layer model. These species fluxes are then

used as input for a two-dimensional axi-symmetric wake code which incorporates the non-equilibrium vibrational and chemical kinetics. This code is the heart of the computer package and provides as output the space-time vibrational/chemical histories of all wake species. This output may then be used in conjunction with a radiation code to provide wake infrared radiation histories in specified bandpasses.

This basic computer package[3] was taken as the starting point for the present calculations, however a few modifications were made. In terms of the computer programs the major modification was performed on the two-dimensional wake code. Since this code requires the integration of a large number of "stiff" differential equations in two dimensional space (i. e. the chemi/vibro-relaxation equations), the computer calculations are both lengthy and costly. The predictor-corrector integration scheme used in the code was originally derived by Lewis,[4] who has recently[5] developed a somewhat more sophisticated technique. The computer code has now been modified to include this new integration scheme and it has been found that the program running time has been reduced by a factor of 1.7 with no loss in accuracy.

The second major modification in the computer package involved the vibrational/chemical kinetic scheme used. This scheme was originally developed several years ago[2] and included all important chemical reactions involving the species H, O, N, CO, H_2, NO, N_2, OH, O_2, CO_2 and H_2O. With regard to vibrational kinetics NO and OH were taken to be in equilibrium in order to minimize the number of reactions. All other vibrational reactions of importance were included. In the modeling each important vibrational mode of a molecule was treated as an independent species and only those vibrational modes which had significant populations at temperatures of $2500^\circ K$, the approximate peak wake temperature, were included. As might be expected this involves a large number of vibrational reactions, some of which had not been studied, and a number of the rate constants (or the temperature dependence of rate constants) had to be estimated.

-4-

This kinetic package has been updated under the present program. Furthermore the vibrational kinetics of HF have been added to the scheme inasmuch as this species can be the dominant wake radiator in the $3-4\mu m$ wavelength region. The update was an indepth one, utilizing the recent reviews by Lewis and Trainor[6] and by Taylor[7] as well as a large number of relevant measurements published in the last few years. This overall review resulted in some fifty changes, additions or deletions in the kinetic package. The updated kinetic scheme used may be found in Appendix A. There are of course still a number of rate constants which required estimation, however it is felt that for the most part the dominant reaction mechanisms are well defined.

There is one point which should be made relative to the chemical reactions. Since each vibrational mode is treated as a distinct species the individual chemical reactions of excited states must also be specified. This turns out to be an advantage since it allows a convenient method for incorporation of chemi-excitation effects such as enhancement of reaction rate constants due to vibrational excitation of the reactants and the creation of reaction products in non-equilibrium state distributions. The only chemi-excitation reactions of importance in the present kinetic scheme are the binary processes for production of HF*

$$H + F_2 \rightarrow HF^* + F \tag{1}$$

$$F + H_2 \rightarrow HF^* + H \tag{2}$$

Both of these reactions can produce HF in highly excited vibrational levels, up to $v = 6$, and a very large kinetic scheme would be required in order to include all reactions of importance between these vibrational levels.[8] In the present work it has been assumed that reactions (1) and (2)

produce HF only in the first vibrational state. Although this is a poor
approximation, it turns out that for the cases considered chemical
production of HF in the wake is not the dominant source of HF, i.e., it
originates in the equilibrium boundary layer. Care should be taken how-
ever when applying this kinetic scheme to other systems.

C. Predictions

1. Initial conditions

Wake calculations have been performed over an altitude range of
69 - 38 km for a generic medium-sized slender vehicle. Re-entry velocity
was taken to be approximately 7 km/sec with initial wake velocities relative
to the body of approximately 6 km/sec. All wake calculations were initiated
at a temperature of $2500^{\circ}K$ with initial temperature, velocity and species
profiles specified as radially constant across the wake. Past experience
has shown that such top-hat profiles rapidly decay to the standard
Gaussian-like profiles in the near wake. Wake edge conditions were as
specified by the standard atmosphere tables[9].

In order to include a large variety of chemical species in the wake
the vehicle was taken to be composed of a teflon nose with a carbon
phenolic frustrum. The initial near wake mole fractions (moles/original
mole) used in the calculations are shown in Table I. These are deduced
by integrating over the predicted partial equilibrium boundary layer species
profiles.

For the case considered, fluorine-containing species represent the
dominant contaminants at higher altitudes since the teflon nose is heated
to ablation temperatures more rapidly than the phenolic afterbody. Thus
at the higher altitudes most of the hydrogen is tied up in the species HF and
the concentration of water vapor is minimal. As the altitude decreases
the afterbody heats, the level of carbon phenolic ablation increases, and
relatively large concentrations of H_2O, H_2 and OH are found in the wake.
It should be noted that there are significant concentrations of free radicals
such as O, H, F, OH, etc. at all altitudes and thus there is a strong poten-
tial for chemical reaction in the wake.

TABLE I

INITIAL WAKE SPECIES MOLE FRACTIONS

SPECIES	H = 69 km	H = 61 km	H = 53 km	H = 46 km	H = 38 km
F	1.10×10^{-2}	1.03×10^{-2}	3.78×10^{-3}	6.76×10^{-4}	3.95×10^{-4}
H	1.04×10^{-3}	3.00×10^{-3}	9.82×10^{-3}	3.89×10^{-2}	7.08×10^{-2}
O	8.07×10^{-2}	7.61×10^{-2}	6.45×10^{-2}	4.01×10^{-2}	2.24×10^{-2}
CO	6.52×10^{-3}	1.27×10^{-2}	1.96×10^{-2}	5.27×10^{-2}	9.68×10^{-2}
F_2	1.00×10^{-5}	1.00×10^{-5}	1.00×10^{-5}	1.00×10^{-5}	1.00×10^{-5}
HF	4.59×10^{-3}	1.29×10^{-2}	2.08×10^{-2}	2.58×10^{-2}	2.42×10^{-2}
H_2	1.17×10^{-6}	1.16×10^{-5}	2.33×10^{-5}	6.87×10^{-3}	2.78×10^{-2}
N_2	7.71×10^{-1}	7.60×10^{-1}	7.48×10^{-1}	7.00×10^{-1}	6.41×10^{-1}
NO	7.88×10^{-3}	8.97×10^{-3}	9.67×10^{-3}	9.12×10^{-3}	7.40×10^{-3}
OH	1.36×10^{-4}	4.70×10^{-4}	2.74×10^{-3}	1.17×10^{-2}	1.38×10^{-2}
O_2	1.58×10^{-1}	1.53×10^{-1}	1.49×10^{-1}	1.20×10^{-1}	9.35×10^{-2}
CO_2	2.95×10^{-3}	5.42×10^{-3}	8.23×10^{-3}	1.87×10^{-2}	2.16×10^{-2}
H_2O	6.23×10^{-7}	7.20×10^{-6}	1.23×10^{-3}	1.43×10^{-2}	2.53×10^{-2}

Non-equilibrium chemical/vibration wake predictions have been made at the five altitudes listed in Table I. The calculations at the highest four altitudes were performed for the case of a laminar wake with the standard molecular viscosities applied to the diffusion equations. The calculation at 46 km was carried to a shorter distance downstream than those at higher altitudes in order to account for the fact that the length of laminar wake, i.e. distance behind the vehicle prior to turbulent transition, decreases with decreasing altitude.

At the lower altitude considered, 38 km, turbulent transition was assumed to occur directly behind the body and the two-dimensional wake code was modified in order to allow the prediction of turbulent wake characteristics. This was accomplished by providing an option to use a turbulent rather than laminar viscosity in the calculation. The turbulent eddy viscosity applied was that developed by Donaldson and Gray,[10] defined by the relationship

$$\epsilon = 0.08 \, r' \, (U_{1/2} - U_c) \sqrt{\frac{\rho_e}{\rho_c}} \, \exp\left(-\frac{1}{2} \, (r'/r')^2\right) \quad (3)$$

where the subscripts e and c correspond to wake edge and centerline properties respectively. In the above equation ρ is density, U wake velocity, r radius and

$$U_{1/2} = \frac{U_c + U_e}{2} . \quad (4)$$

Lastly r' is that value of wake radius where

$$U(r') = (U_c - U_e) \, e^{-2} + U_e \quad (5)$$

-8-

2. Chemical kinetics

Examples of the effect of chemistry on wake species concentrations are shown in Figs. 1-5. Wake centerline histories of the mole fraction of H_2O at the five altitudes considered are displayed in Fig. 1. At the highest altitudes shown wake chemical kinetic times are typically slow because of the low wake densities, thus, significant concentration changes due to chemical reaction are not to be expected. There is, however, a noticeable increase in the H_2O concentration at the altitudes of 61 and 69 km, mostly resulting from the reaction

$$OH + OH \longrightarrow H_2O + O \qquad (6)$$

This increase occurs because H_2O is a minor ablation product species at these altitudes and therefore a small production rate can produce a significant concentration change. Indeed it can be seen that at the lower altitudes of 53 and 46 km where the initial H_2O concentration is higher there is little change in the H_2O concentration. This is partially due to the fact that the centerline wake temperature is $\sim 2300 - 2500^{\circ}K$ over this length of wake. Off wake axis, where the temperature is lower, there is some production of H_2O at these altitudes.

The H_2O mole fraction prediction at 38 km is quite different than those for higher altitudes. The drop in H_2O concentration is a result of rapid dilution resulting from the fast growth of the turbulent wake. Although it cannot be deduced from the centerline history shown, there has been a significant conversion of H and OH to H_2O at this altitude. In other words the total flux of H_2O in the wake has increased; although the local mole fraction is smaller, the total wake area has increased in compensation.

Centerline histories of the mole fractions of CO and CO_2 for altitudes of 61 and 46 km are shown in Fig. 2. At the highest altitude the [CO] and [CO_2] mole fractions both decrease slowly due to laminar diffusion. Since the total wake flux of elemental carbon must be conserved, chemistry
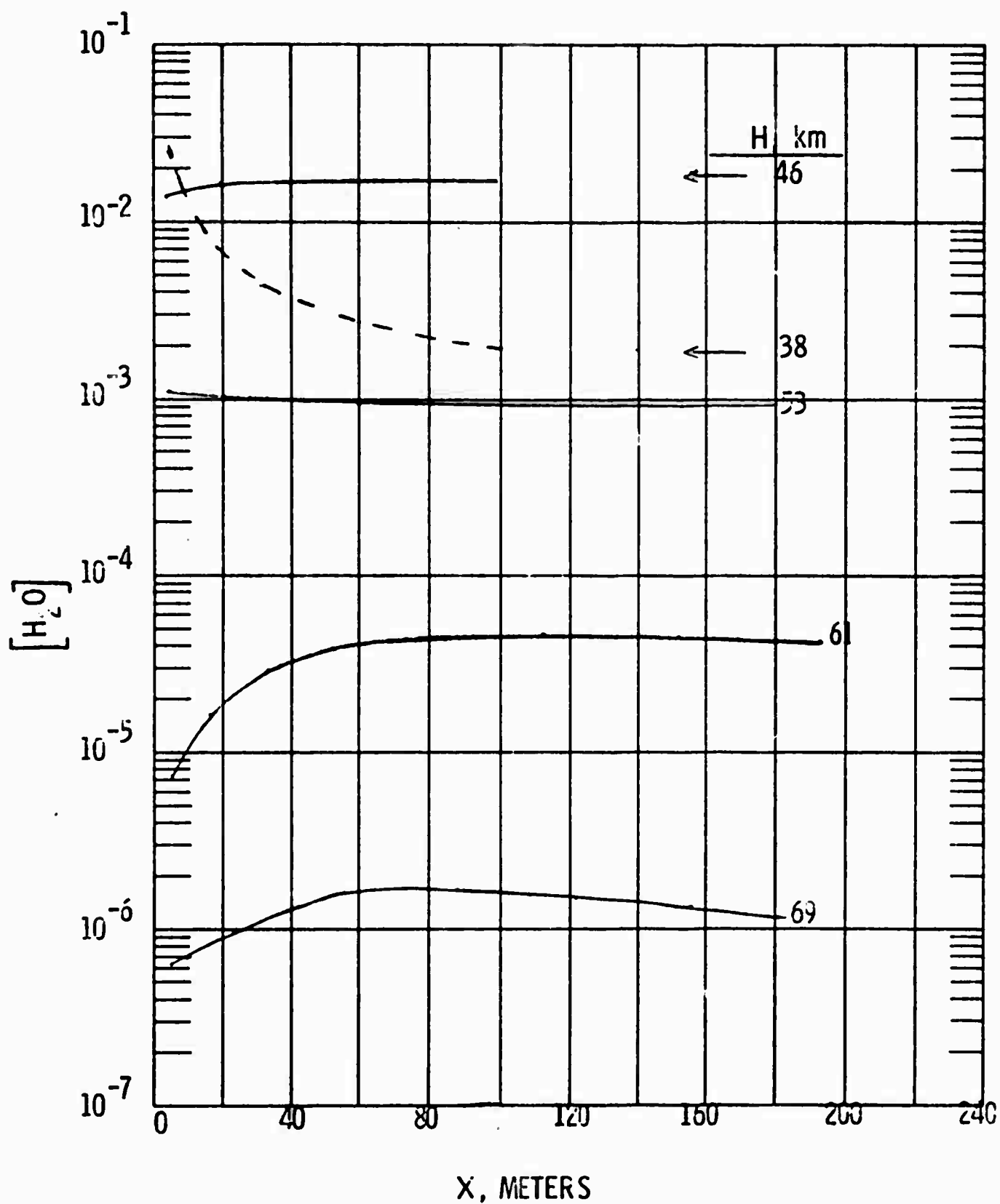
Fig. 1   Wake Centerline H_2O Mole Fraction vs. Distance.
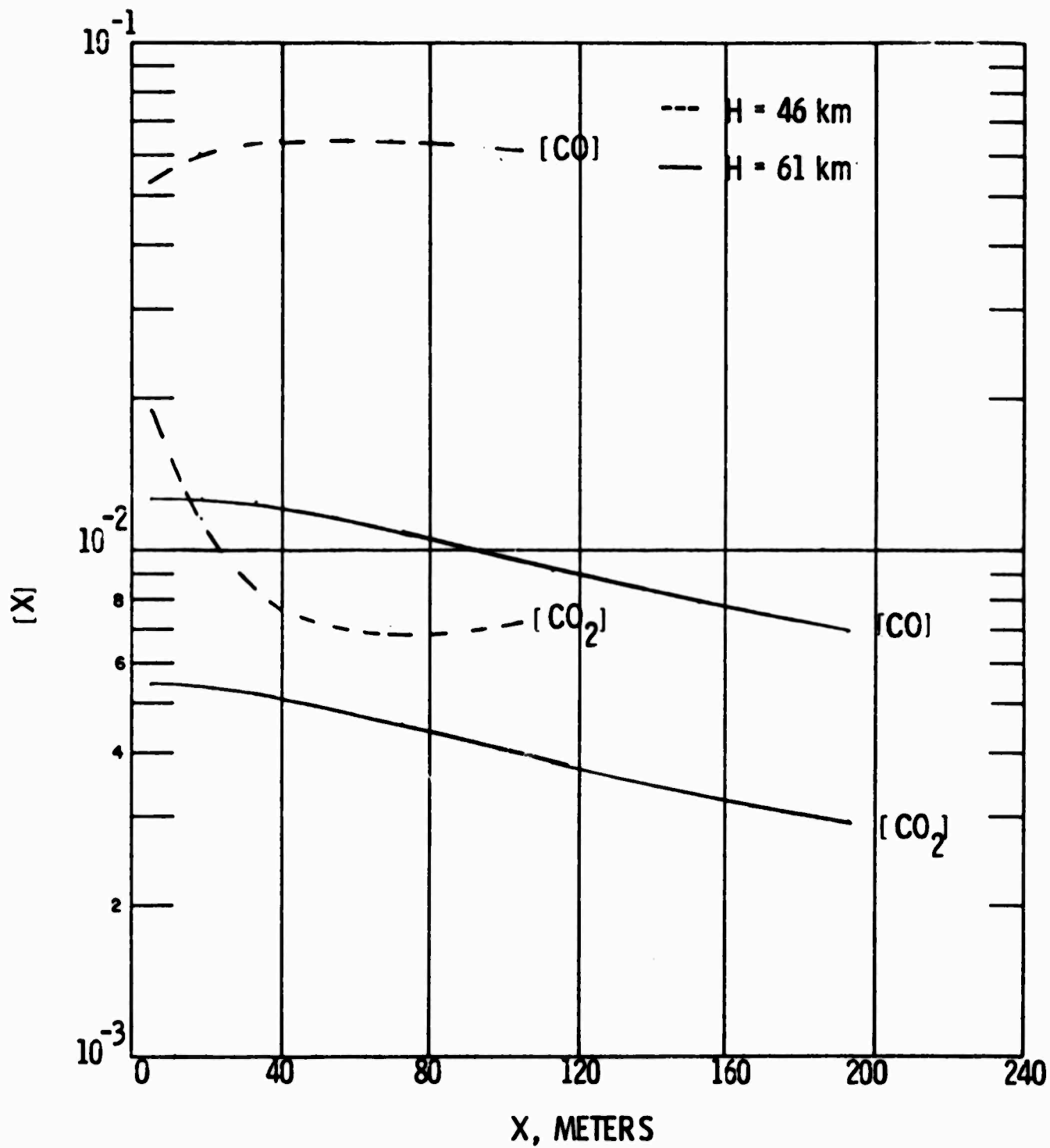
Fig. 2   Wake Centerline CO and CO_2 Mole Fractions vs. Distance

will only effect the ratio of CO and CO_2 and not the sum of the two. As can be seen this ratio does not change at the higher altitude and thus chemical reaction is unimportant.

This situation is reversed at the altitude of 46 km where chemical kinetics does play a role. As can be seen from the histories in Fig. 2, CO_2 is being dissociated to CO in the near wake. This trend reverses at a distance of about 80 meters where it can be seen that the $[CO_2]$ mole fraction begins to increase while that for $[CO]$ decreases. In general, this byplay is a result of the reaction

$$CO + OH \longleftrightarrow CO_2 + H \cdot \qquad (7)$$

At the near wake centerline temperatures of $\sim 2500^o K$ the reverse of this reaction is favored and thus CO_2 is converted to CO. Further downstream in the wake, where the temperature is somewhat lower, the reaction proceeds in the forward direction converting CO to CO_2. The far wake behaviour, which is not shown, is that the CO is completely oxidized to CO_2.

This effect is best seen by considering the radial profiles of CO and CO_2 shown in Figs. 3-5 for wake distances of 20, 60 and 100 meters and an altitude of 46 km. An inert species, not present in the ambient atmosphere, would have a Gaussian-like radial distribution much like that shown for CO in Figs. 3-5. The wake temperature profile would also have a similar shape. The CO_2 profiles shown in Figs. 3-5 are quite non-Gaussian because of chemical effects. As can be seen the profiles exhibit an off-axis peak which tends to move toward wake center with increasing distance behind the wake. This behaviour results from the fact that the forward direction of reaction (7) is favored in the lower temperature regions of the wake.
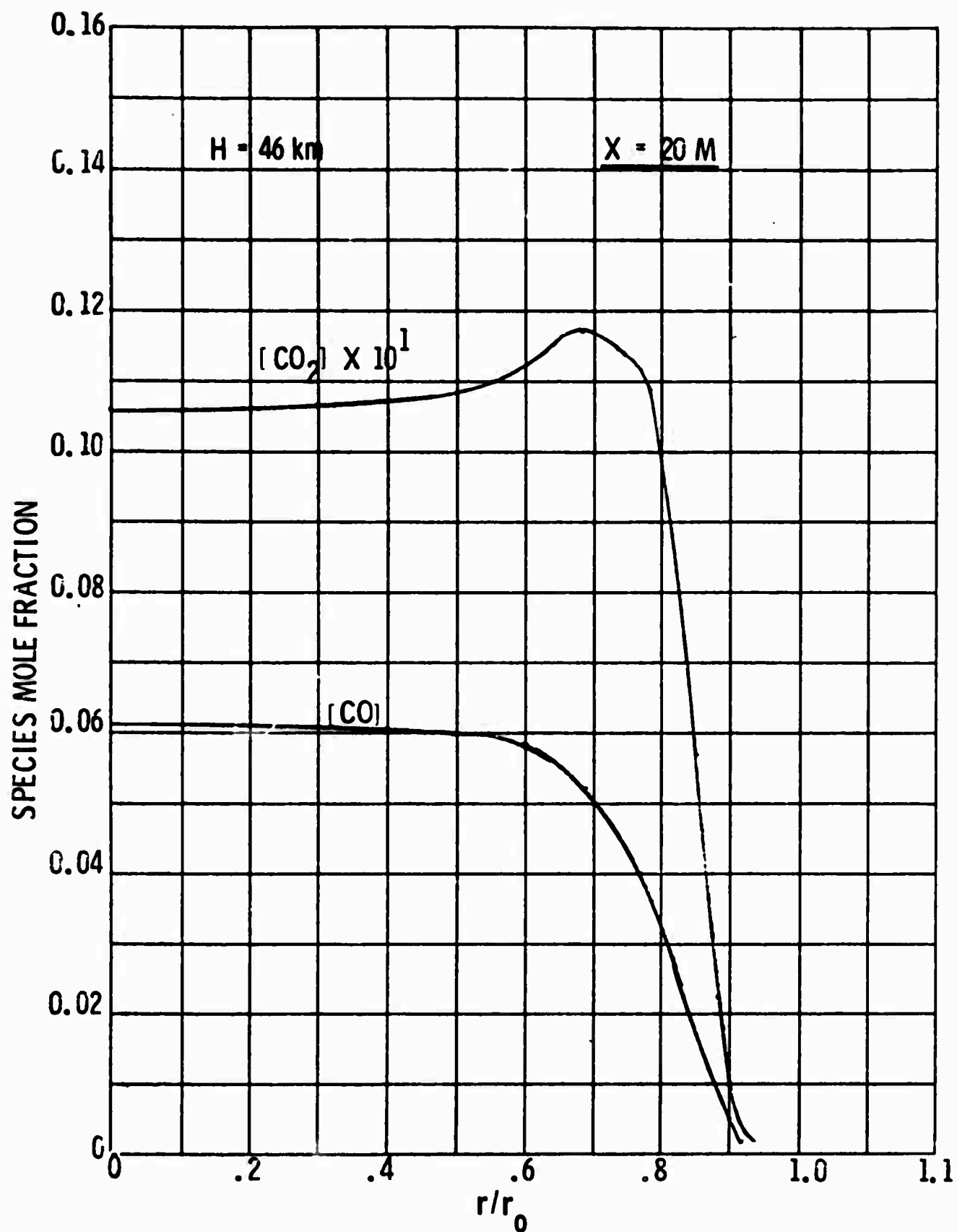
Fig. 3   CO and CO_2 Mole Fraction vs. Normalized Wake Radius, X = 20 M

-13-
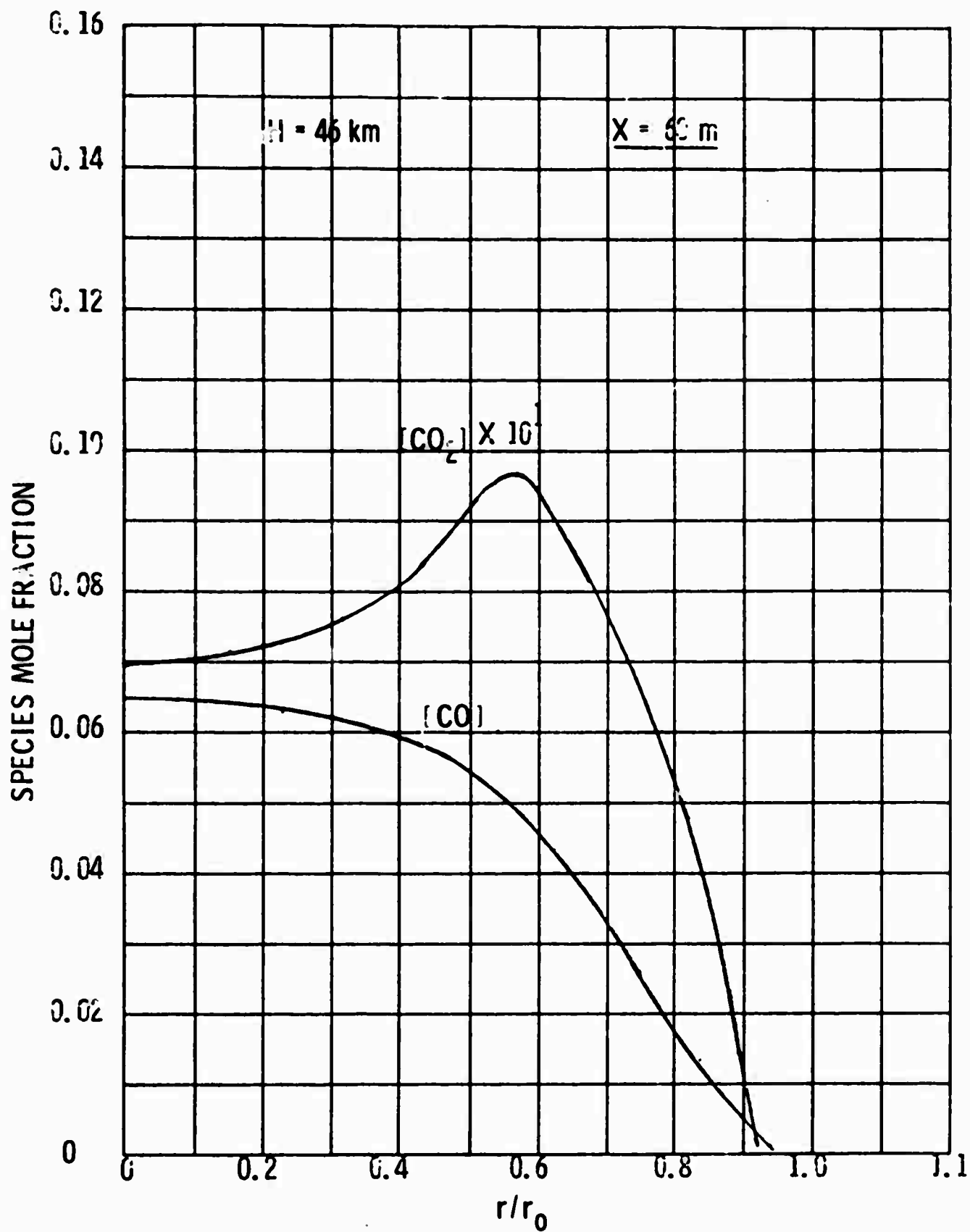
Fig. 4   CO and CO_2 Mole Fraction vs. Normalized Wake Radius, X = 60 M
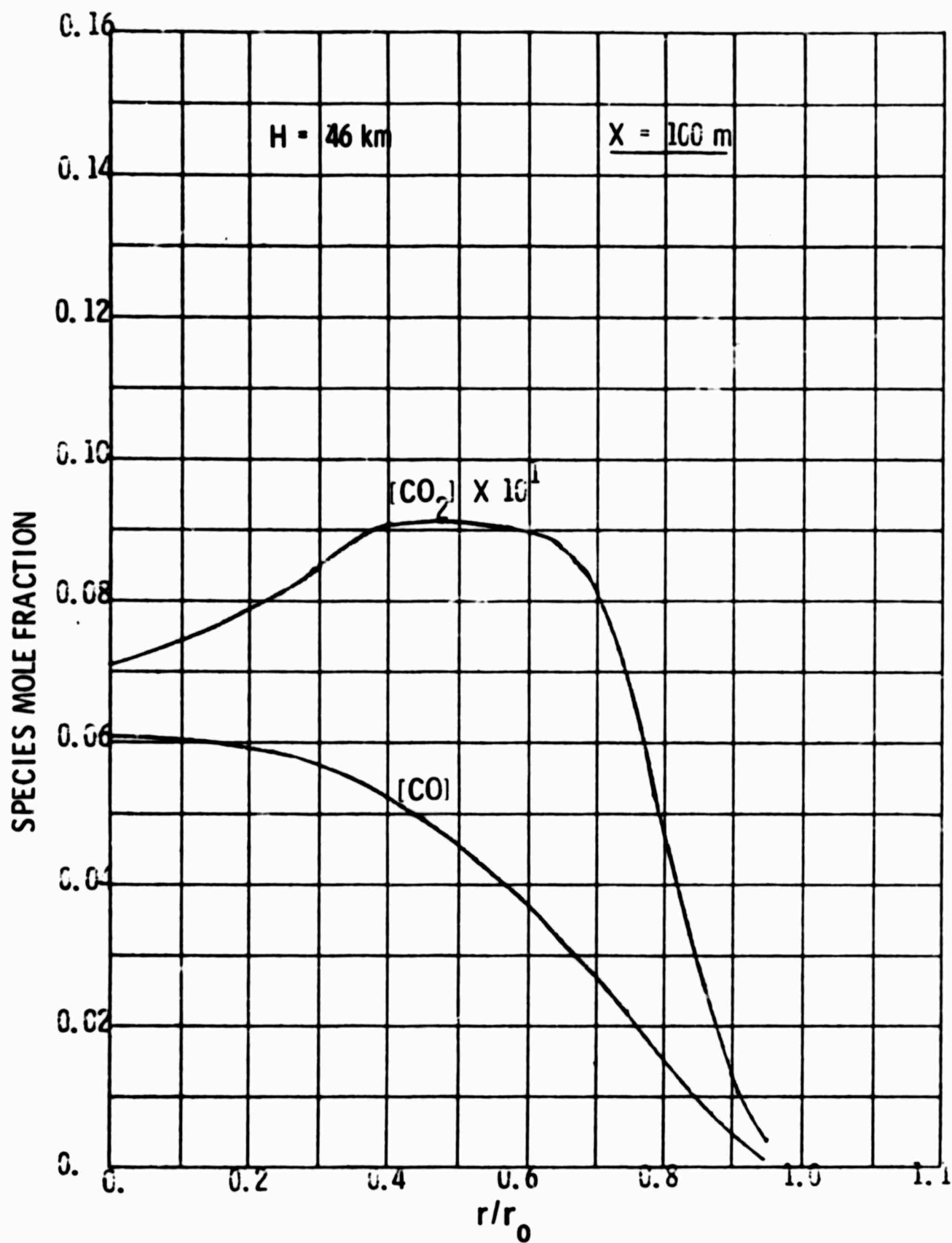
Fig. 5 CO and CO₂ Mole Fraction vs. Normalized Wake Radius, X = 100 M

In summary, at the highest altitudes considered chemical effects are unimportant except for the production of trace species. On the other hand at the lower altitudes the chemical processes tend to convert free radicals to more stable molecules. This conversion can be deterred in laminar wakes since the temperatures can be large enough to allow significant equilibrium concentrations of free radicals. This, however, does not occur in the turbulent wake at the lowest altitude considered where the temperature drops rapidly.

3. Vibrational kinetics

The detailed vibrational kinetic scheme employed in the wake calculations involves some 117 reactions, as seen in Appendix A. However, the general vibro-relaxation phenomenology may best be understood by reference to the vibrational mode energy level diagram shown in Fig. 6, which was excerpted from Ref. 6.

As can be seen, the CO_2 molecule has three vibrational modes. These modes are coupled to each other by kinetic mechanisms and the ν_2 mode is strongly coupled to the translational temperature because of its low vibrational energy. CO_2 can vibrationally communicate with other molecules, predominantly through the ν_3 mode which is in near energy resonance with both CO and N_2. The ν_3 mode also has a very short radiative lifetime, ~ 2.5 msec, and this will play an important role in the calculations as will be seen.

The H_2O molecule also has three modes which are coupled together, at low temperatures even more strongly than the modes of CO_2. The shortest radiative lifetime for H_2O is an order of magnitude larger than that for the $CO_2(\nu_3)$ state. Although H_2O can vibrationally communicate with H_2 and O_2 there are not efficient vibrational exchange mechanisms between H_2O and CO, N_2 and CO_2.

The molecule, HF, which was added to the kinetic scheme in the present work, adds a new dimension to the vibrational phenomenology since
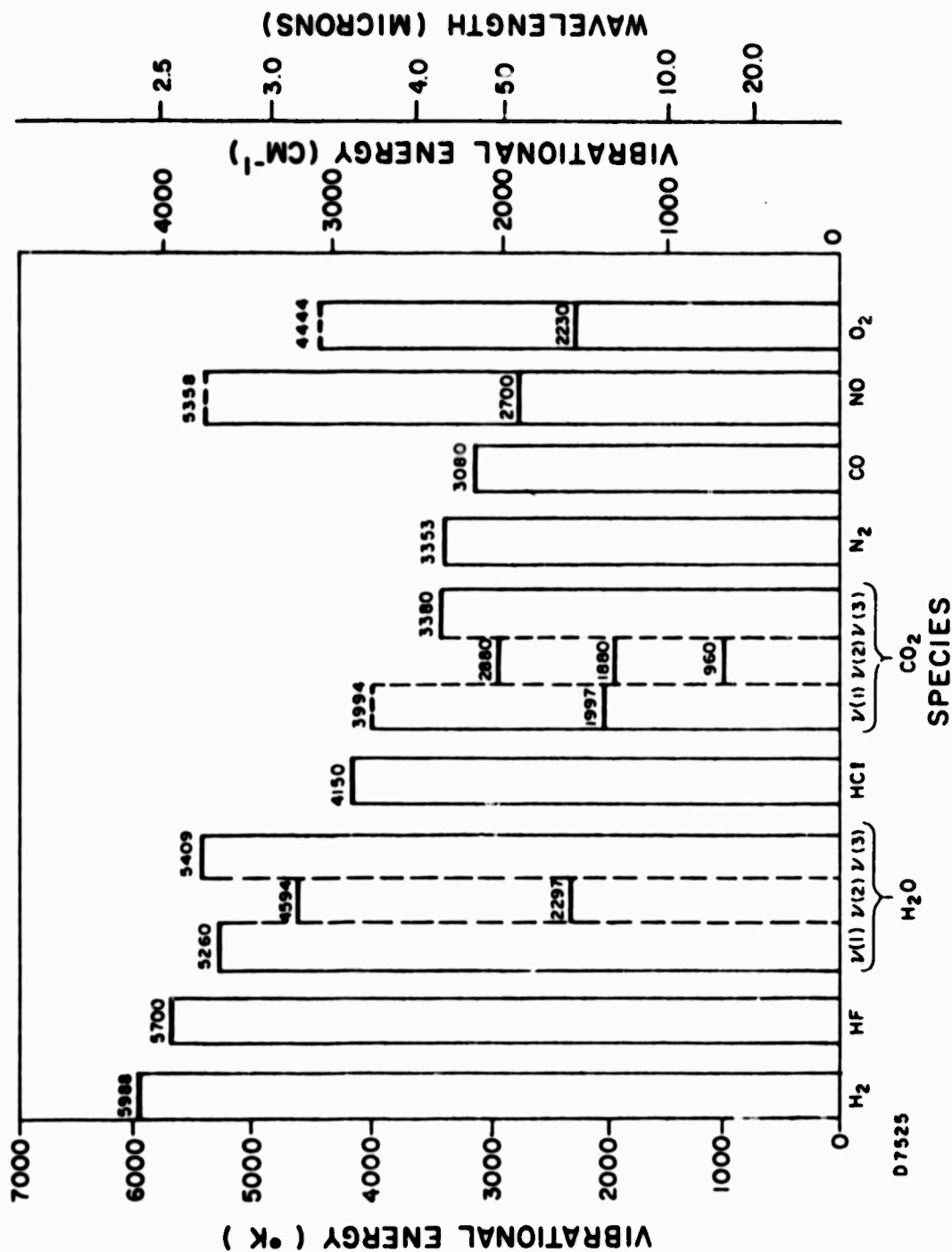
Fig. 6 Vibrational Energy Spacings for Molecules of Interest. Figure taken from Ref. 6.

-17-

it can undergo a rapid vibrational exchange reaction with both H_2O and CO_2 and thus effectively provides a coupling mechanism between these two molecules. Furthermore, since the radiative lifetime of HF is considerably shorter than that for H_2O, the strong vibrational coupling between H_2O and HF can lead to vibrational depopulation of H_2O via HF radiative decay.

Two simplifying approximations have been made in the vibrational kinetic scheme listed in Appendix A. (1), In actuality the CO_2 ν_2 mode is degenerate with degeneracy $(v + 1)$ in vibrational level v. However, the vibrational coupling reactions can be greatly simplified if it is assumed that each level of the ν_2 mode is doubly degenerate. This assumption has been made and it can readily be shown that the total vibrational energy in ν_2 is the same in either case. (2), The radiative lifetimes of the H_2O ν_1 and ν_3 modes differ by a factor of twenty with that for the ν_3 mode being the shorter. It is felt on theoretical grounds that the modes will be strongly collisionally coupled to each other. Therefore the lifetimes of the two modes have been set equal to each other to ensure that decoupling will not occur in the computer predictions.

Shown in Figs. 7 - 11 are predicted wake centerline temperature histories for the altitudes of 69, 61, 53, 46 and 38 km, respectively. In each figure the translational temperature and the vibrational temperatures of CO, HF, $CO_2 (\nu_2)$, $CO_2 (\nu_3)$ and $H_2O (\nu_3)$ are displayed. In can be seen that at the highest altitude the vibrational modes are severely collision limited, i.e., radiative decay is more rapid than collision deactivation, so that the characteristic vibrational temperatures are significantly lower than the translational temperature. This effect becomes less pronounced with decreasing altitude and by 46 km the vibrational temperatures are almost in equilibrium with translation. Although not shown, this same behaviour, ie., collision limiting, is also observed off axis in the wake at these altitudes. The vibrational temperature can be higher than translation in the far wings of the wake, however, the contaminant species concentrations are very low there.

-18-
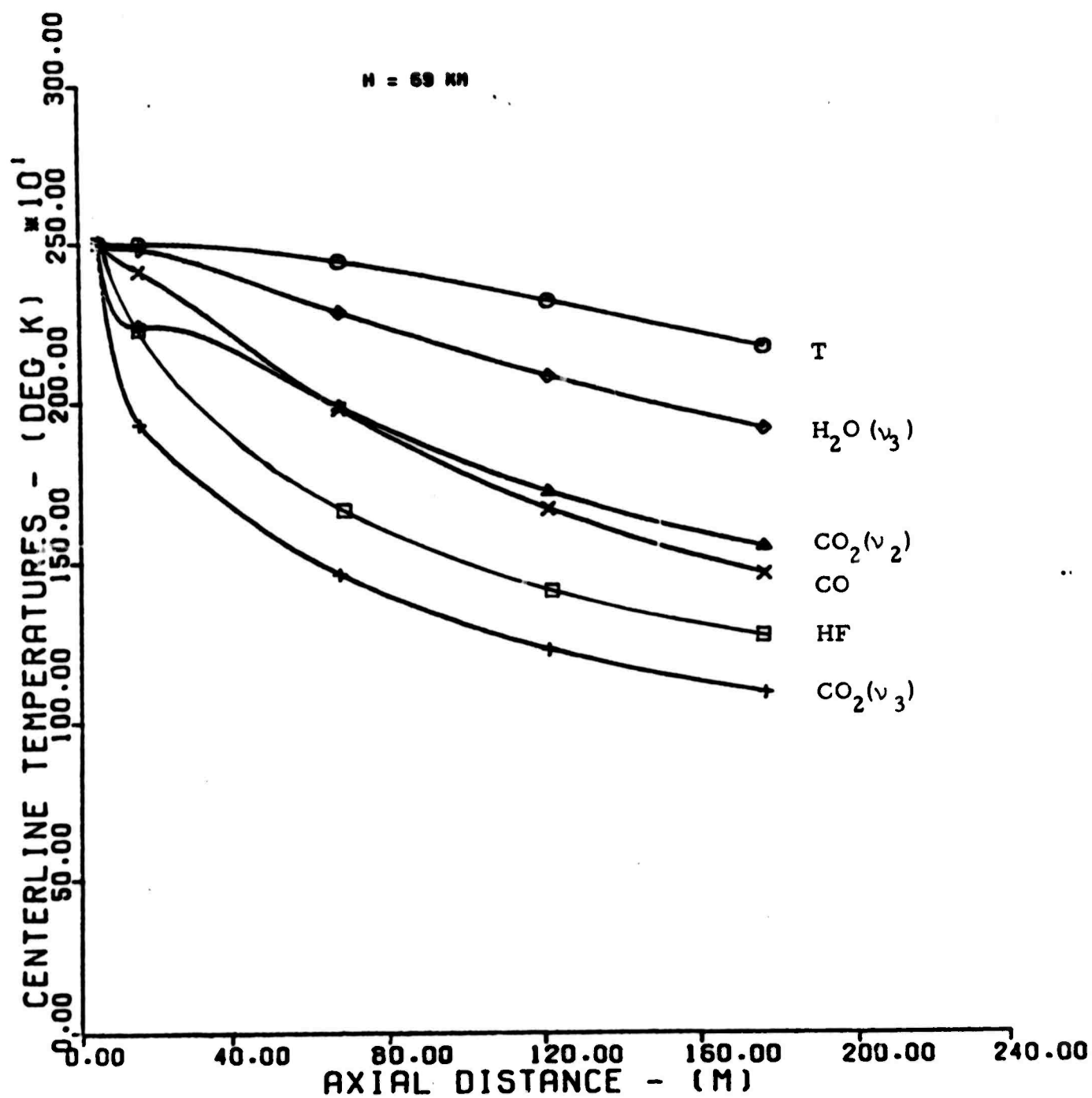
Fig. 7   Predicted Wake Centerline Temperatures vs. Distance, H = 69 km
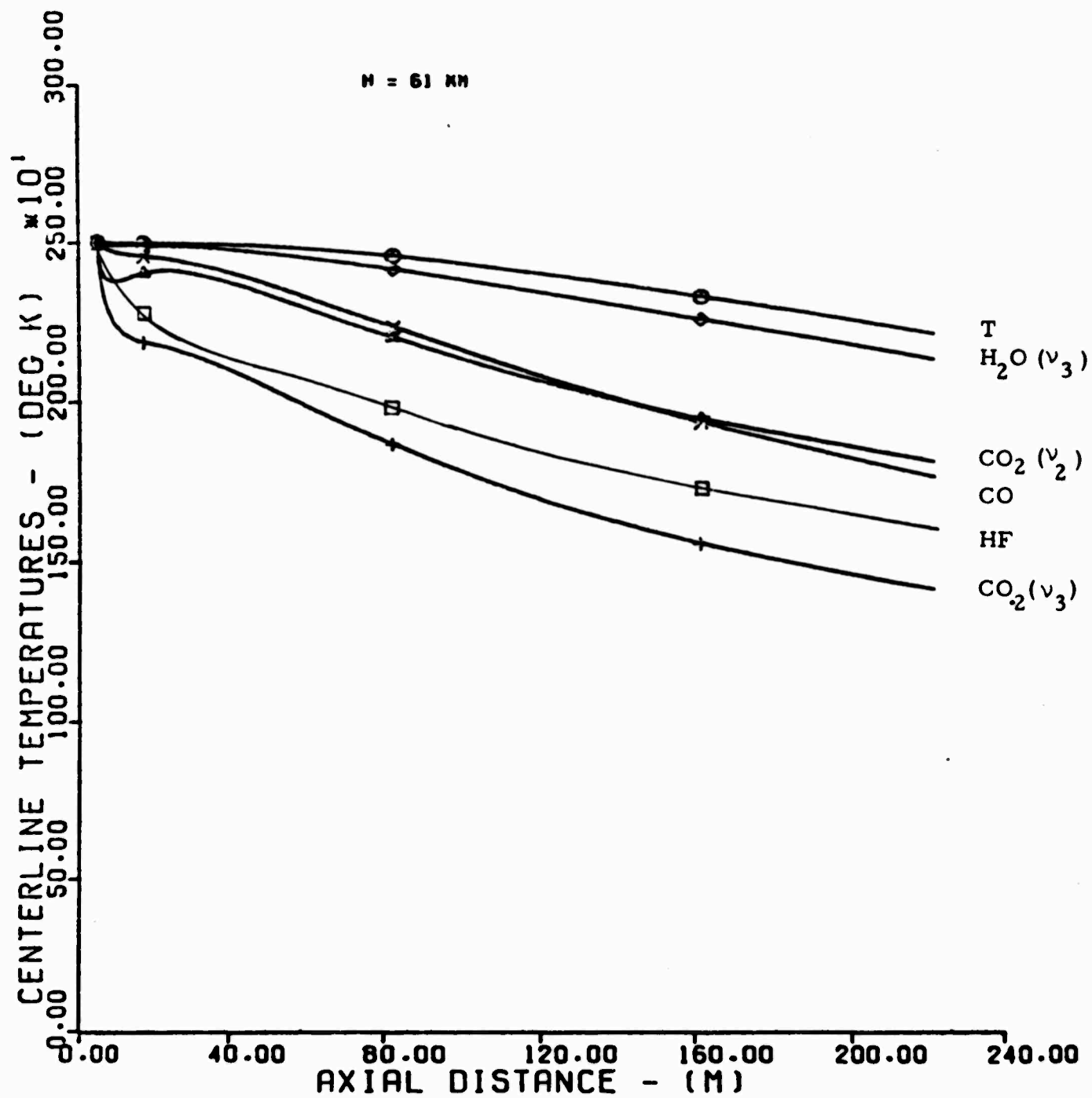
Fig. 8   Predicted Wake Centerline Temperatures vs. Distance, H = 61km
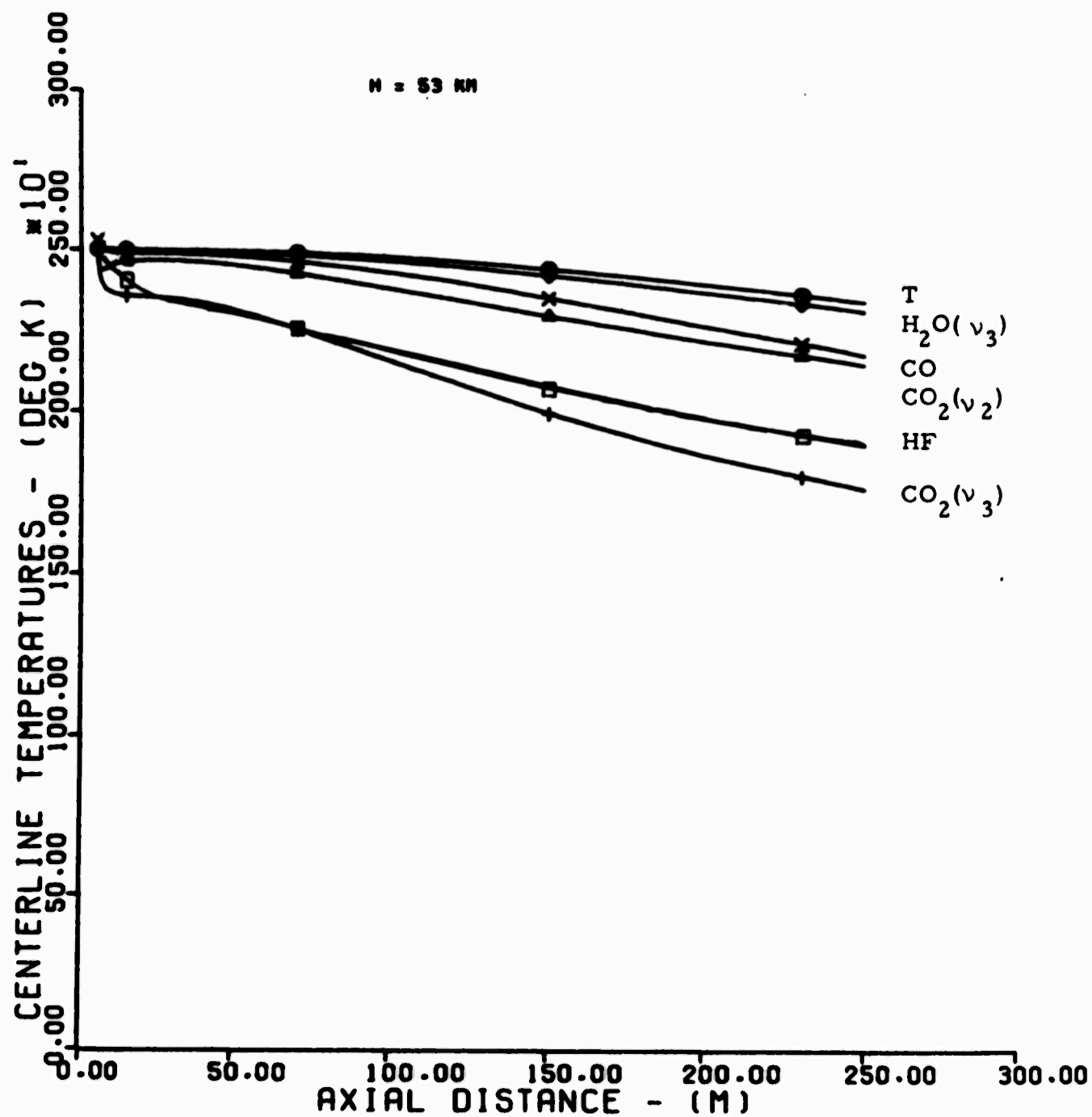
Fig. 9   Predicted Wake Centerline Temperatures vs. Distance, H = 53 km
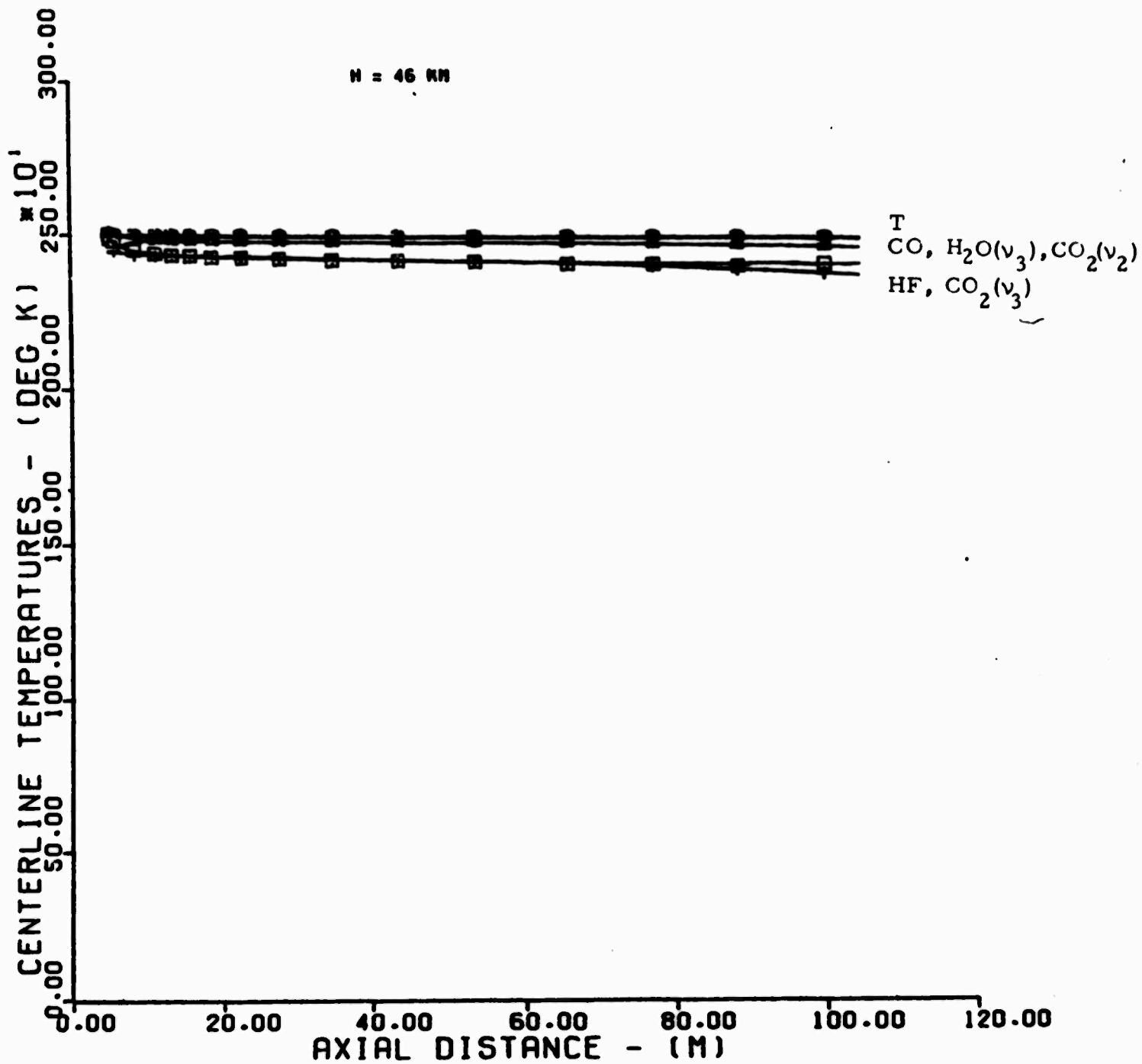
Fig. 10   Predicted Wake Centerline Temperatures vs. Distance, H = 46 km
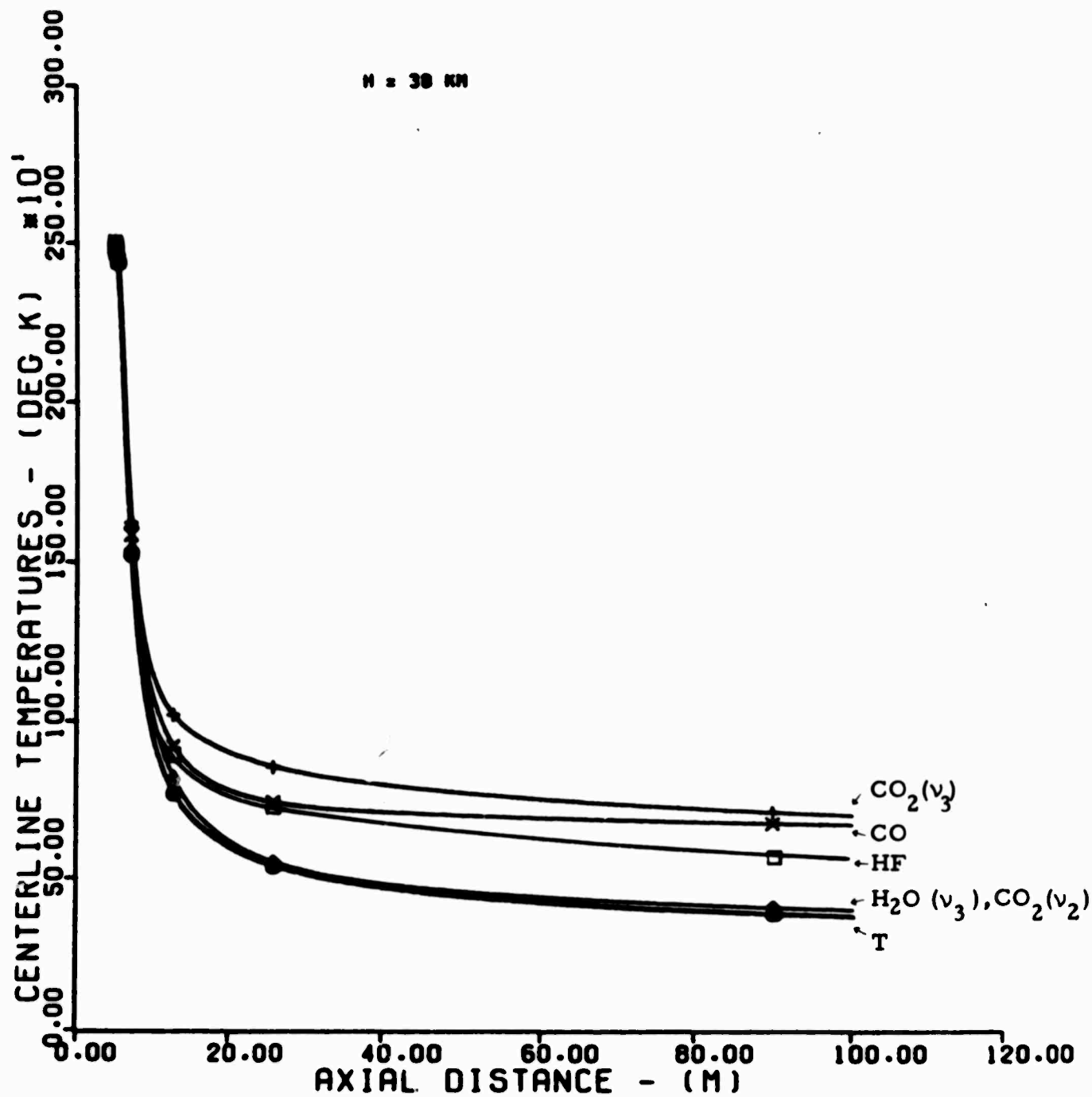
Fig. 11   Predicted Wake Centerline Temperatures vs. Distance, H = 38 km

Note the dramatic effect of the turbulent wake.

This behavior can be readily understood in terms of the radiative lifetimes and kinetics described previously. For example, considering Fig. 7, corresponding to the highest altitude, the CO_2 (ν_3) mode which has the shortest radiative lifetime exhibits the most precipitous drop. Although the CO_2 (ν_2) mode has a lifetime of 0.3 sec., its characteristic temperature also falls below the translational temperature since the CO_2 (ν_3) and (ν_2) modes are strongly coupled at these wake temperatures. HF also falls off quite rapidly in line with its short radiative lifetime. The CO profile decreases more slowly, although still falling significantly below the translational temperature. This behavior is due both to radiative decay and the vibrational coupling between CO and CO_2 (ν_3)

An effect of the chemical kinetics may be observed in the H_2O (ν_3) profiles shown in Figs. 7-8. The radiative decay time for the H_2O (ν_3) state is similar to that for CO and furthermore the ν_3 state can vibrationally exchange with HF; thus one would expect it to be collision limited. Nonetheless, the H_2O (ν_3) temperature closely follows the translational temperature. It will be recalled that H_2O is a trace species at the higher altitudes and that its concentration increases with wake distance through chemical production. Since the model assumes that H_2O produced by chemical reaction is created in vibrational equilibrium with translation, the chemical reaction acts to drive the H_2O (ν_3) vibrational temperature towards the translational temperature in opposition to the radiative/vibrational kinetics. Similar phenomena, although less pronounced, affect the CO and CO_2 (ν_3) temperatures in the mid-range of altitudes shown.

The temperature histories for the turbulent wake shown in Fig. 11 are quite different from those shown earlier for laminar wakes. In this case the wake temperature decays very rapidly because of cold gas entrainment. The vibrational temperatures initially follow this rapid decrease but then begin to freeze out at a wake temperature of approximately $1000^{\circ}K$. Although the CO_2 (ν_2) and H_2O (ν_3) temperatures remain close to the translational temperature throughout, the vibrational temperature of HF, CO

-24-

and CO_2 (ν_3) are as much as a factor of two higher than the translational temperature at a distance 100 meters downstream of the vehicle. Basically what occurs is that the ablation product species become so diluted in the wake that the only important collision partner is nitrogen. The diatomic molecules cannot be rapidly deactivated by nitrogen near room temperature and furthermore, the coupling between the ν_3 and ν_2 modes of CO_2, with nitrogen as the collisional partner, is an inefficient process at these low temperatures.

The behaviour exhibited in Figs. 7 - 11 is typical of polar molecules in general; (i.e., molecules which have a dipole moment and so radiate spontaneously,) and can be readily understood from kinetic considerations. The characteristic time for a gas kinetic collision between any two molecules is defined by

$$\tau_k = Z^{-1} = (NV\sigma)^{-1} \tag{8}$$

where Z is the collision frequency, N the total particle number density, V the mean random molecular speed, and σ the gas kinetic molecular cross section. Even at the laminar wake temperatures of $2500^{\circ}K$, it is rare to find a vibrational process more efficient than a tenth gas kinetic, and furthermore such efficient reactions generally involve contaminant species having mole fractions of order one percent. Thus, although collision times will vary from reaction to reaction a characteristic collision time for vibrational exchange or de ation in re-entry wakes at temperatures near $2500^{\circ}K$ would be $\sim 10 \, \tau_k$.

Shown plotted in Fig. 12 are several multiples of the gas kinetic collision time vs. altitude for a temperature of $2500^{\circ}K$. Also shown as horizontal lines are the radiative lifetimes of several of the vibrational species of interest in the present calculations. If the radiative lifetime of a species is of the same order of magnitude as the characteristic time for
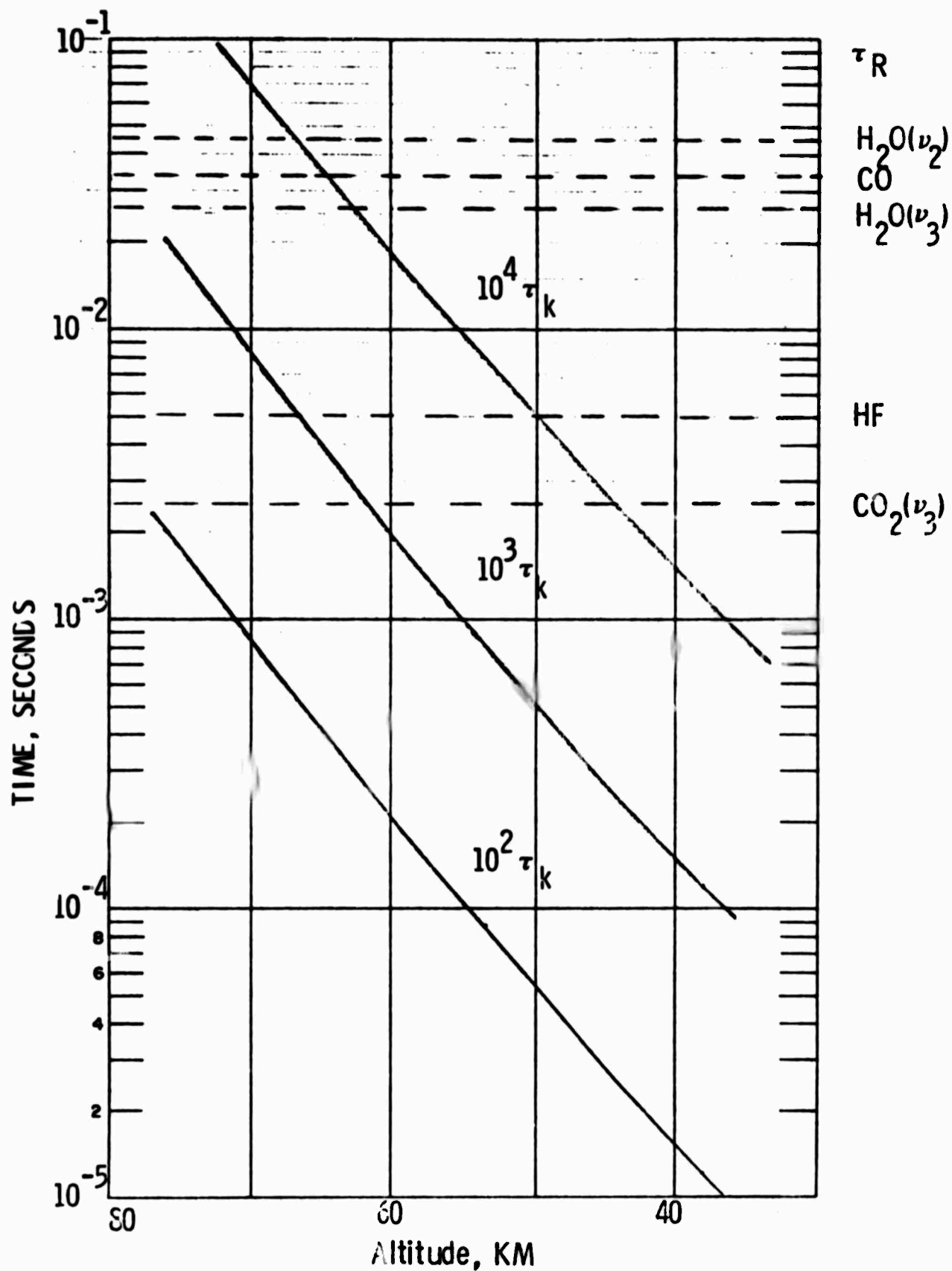
Fig. 12   Multiples of the Gas Kinetic Collision Time vs. Altitude.
Also shown are the radiative lifetimes for the vibrational modes
of several wake molecules.

vibrational exchange/deactivation collisions, that species will be collision limited with a vibrational temperature less than that of translation. Thus it can be seen from Fig. 12 that if the characteristic time for vibrational collision is of order $10^3 \tau_k$ both HF and the $CO_2 (\nu_3)$ mode will be collisionally limited at altitudes above 48 km as was predicted by the detailed calculations. Thus other species which might be introduced into the wake, with similar radiative lifetimes, could also be expected to be collision limited.

The above discussion is valid for the case of a relatively constant temperature laminar wake. In the case of a turbulent wake, with a rapidly decaying translational temperature, the phenomenon of vibrational freezing, rather than collisional limiting, becomes of interest. Vibrational freezing will occur when there are insufficient vibrational deactivation collisions within the flow time to allow the vibrational temperature to drop with the translational temperature. As a specific example consider the calculation at 38 km shown in Fig. 11. The wake temperature fell below 1000°K within the first twenty meters of wake, corresponding to a flow time of $\sim 3 \times 10^{-3}$ sec. From examination of Fig. 12 it can be seen that this flow time corresponds to a collision time of $\sim 10^4 \tau_k$ (note τ_k scales as $T^{-1/2}$). Thus, if the vibrational deactivation efficiency of a species is $\leq O(10^{-4})$ at temperatures below 1000°K, the species will vibrationally freeze. This was indeed the case with CO, HF and the $CO_2 (\nu_3)$ mode as can be seen from the rate constants listed in Appendix A. (Note both CO and $CO_2 (\nu_3)$ can vibrationally exchange with N_2 however the N_2 vibrational temperature is also frozen at this altitude).

4. Radiation predictions

Given the defined axial and radial wake temperature and species profiles, infrared radiation predictions may be specified in any desired bandwidth. Since wake radiation levels in atmospheric windows are of

-27-

particular interest, radiation predictions have been provided for the respresentative bandwidths of 3 - 4 μm, 3 - 5 μm, 10.2 - 12.6 μm, and 17.2 - 22.8 μm. The important radiators in each of these bandpasses are listed in Table II. This tabulation does not imply that the main portion of the bands listed fall in the specified bandwidth; indeed this is generally not the case. For example, the $H_2O(\nu_3)$ and $CO_2(\nu_1, \nu_3)$ bands peak at 2.7 μm, and the center of the HF fundamental vibration band is at 2.5 μm.

It is to be noted that the radiation processes in the 3 - 5 μm region are dominantly vibrational bands and thus the predictions in this wavelength region will be affected by the vibrational relaxation phenomena discussed earlier. This is not the case in the higher wavelength region which is dominated by radiation from pure rotational bands. The wake chemical kinetics will be most important in this latter region as well as the fluid dynamics which establishes the translational/rotational temperature of the wake gases.

Predictions of wake radiation per unit length for these bandwidths at altitudes of 69 and 46 km respectively are shown in Figs. 13 - 20. The history of each band is shown separately. The 69 km case is characterized by severely collision limited vibrational temperatures and near frozen chemistry whereas the 46 km predictions correspond to near vibration/ translation equilibrium and rapid chemical reaction.

The 69 km case corresponded to a negligible H_2O concentration relative to HF. Thus HF is the dominant radiator in the 3 - 4, 10.2 - 12.6 and 17.2 - 22.8 μm bands as seen in Figs. 13, 15, 16. The decrease in the HF fundamental vibrational band radiation with distance is quite sharp (see Fig. 13) due both to collisional limiting and to the fact that only a portion of the P branch of the band falls in the 3 - 4 μm region. It can be seen in the 3 - 5 μm region, shown in Fig. 14, that radiation from CO and CO_2 strongly dominate that from HF. This is true at all altitudes and indeed the

TABLE II

VIBRATION/ROTATION BANDS
IN SPECIFIED BANDWIDTHS

BANDWIDTH	RADIATORS
$3 - 4 \, \mu m$	HF FUNDAMENTAL BAND
	$CO_2 \, (\nu_1, \nu_3)$ COMBINATION BANDS
	$H_2O \, (\nu_3)$ BAND
	OH PURE ROTATION BAND
$3 - 5 \, \mu m$	ALL BANDS LISTED ABOVE
	CO FUNDAMENTAL BAND
	$CO_2 \, (\nu_3)$ BAND
	$H_2O \, (\nu_3 \rightarrow \nu_2)$ BAND
$10.2 - 12.6 \, \mu m$	$CO_2 (\nu_2)$ BAND
	HF PURE ROTATION BAND
	OH PURE ROTATION BAND
	H_2O PURE ROTATION BAND
$17.2 - 22.8 \, \mu m$	SAME AS FOR $10.2 - 12.6 \, \mu m$
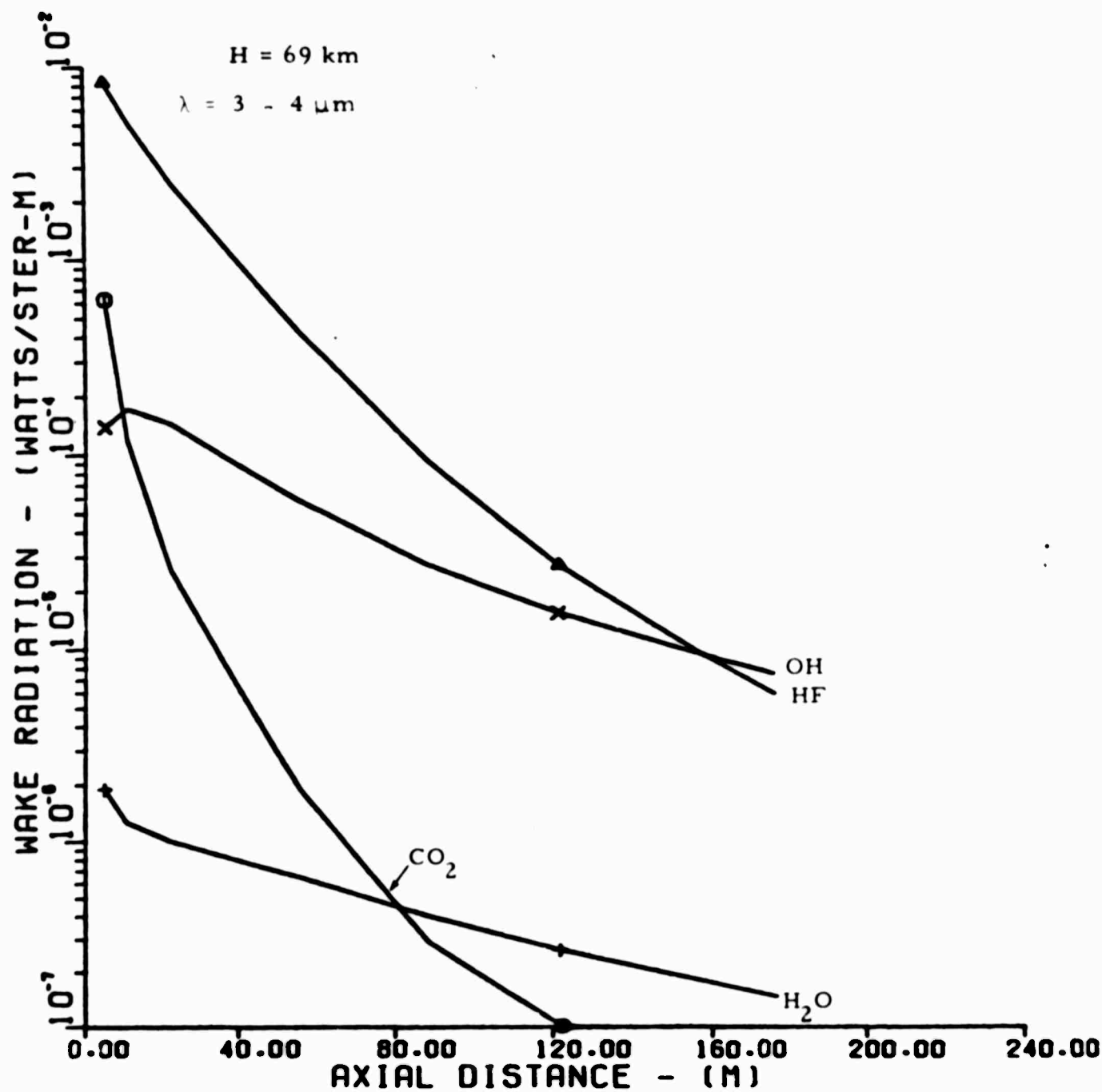
Fig. 13   Wake Radiation vs. Distance for the 3 - 4 μm Bandwidth, H = 69 km
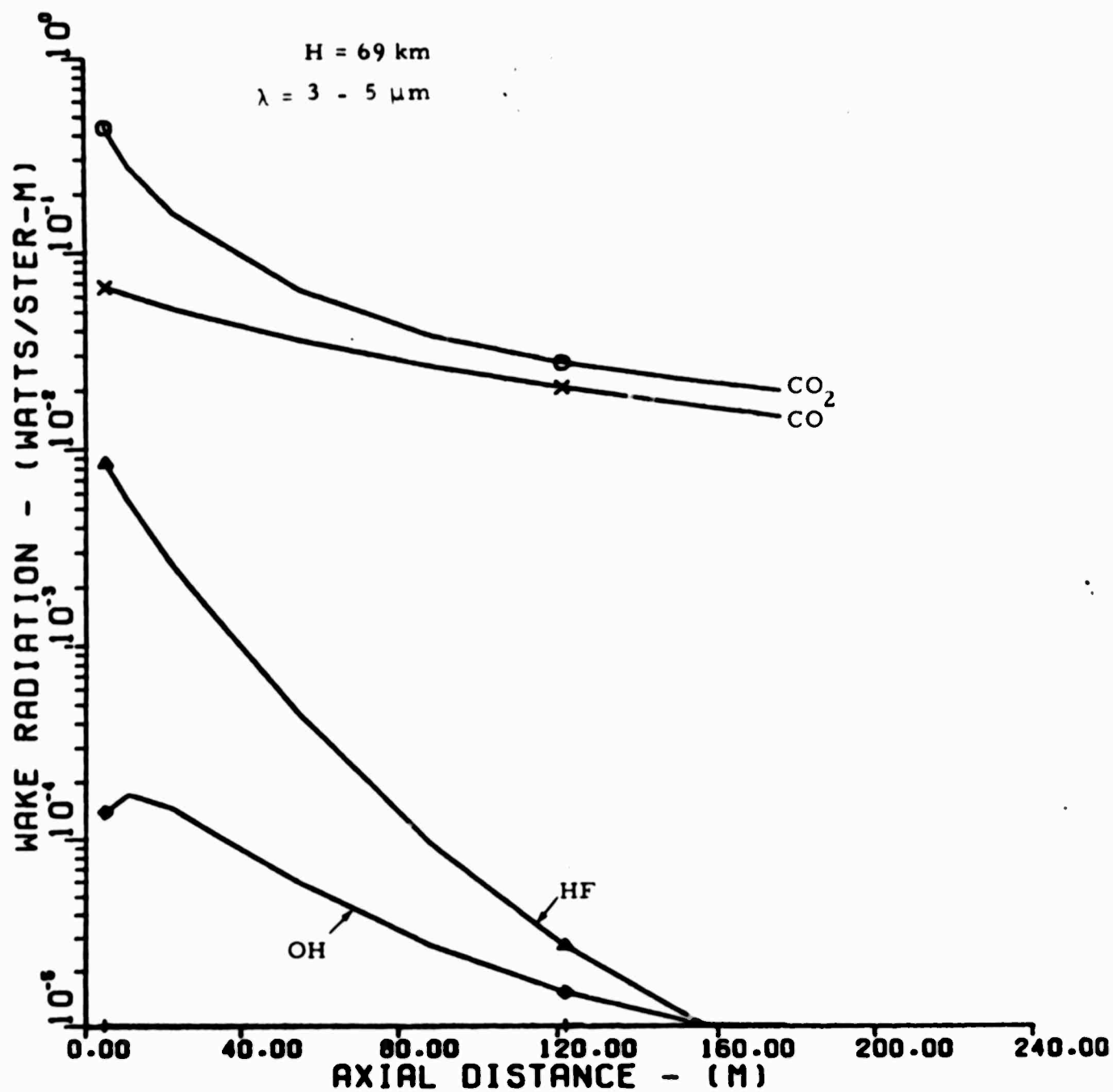
Fig. 14   Wake Radiation vs. Distance for the 3 - 5 μm Bandwidth, H = 69 km
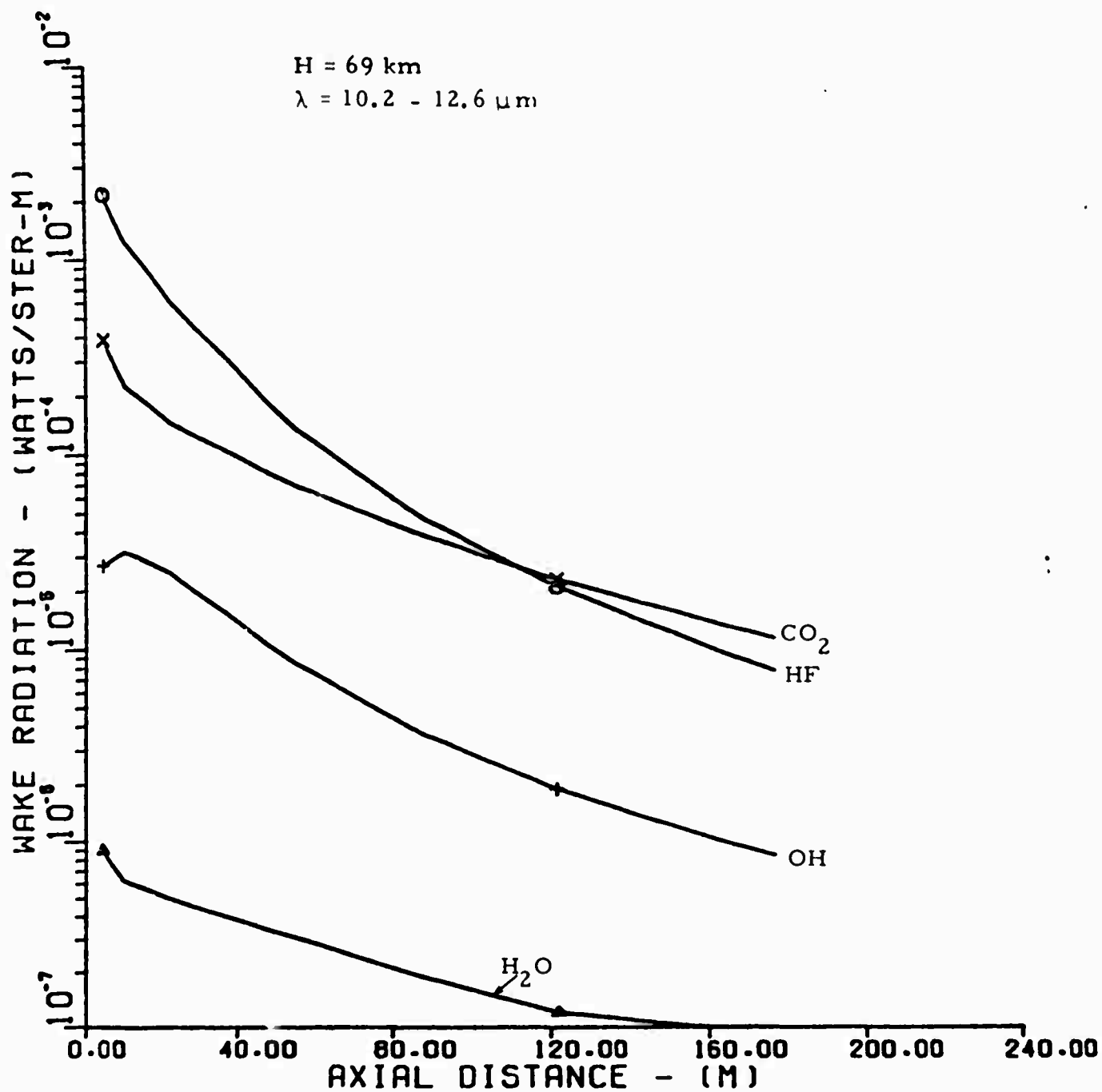
Fig. 15   Wake Radiation vs. Distance for the 10.2 - 12.6 μm Bandwidth,
H = 69 km
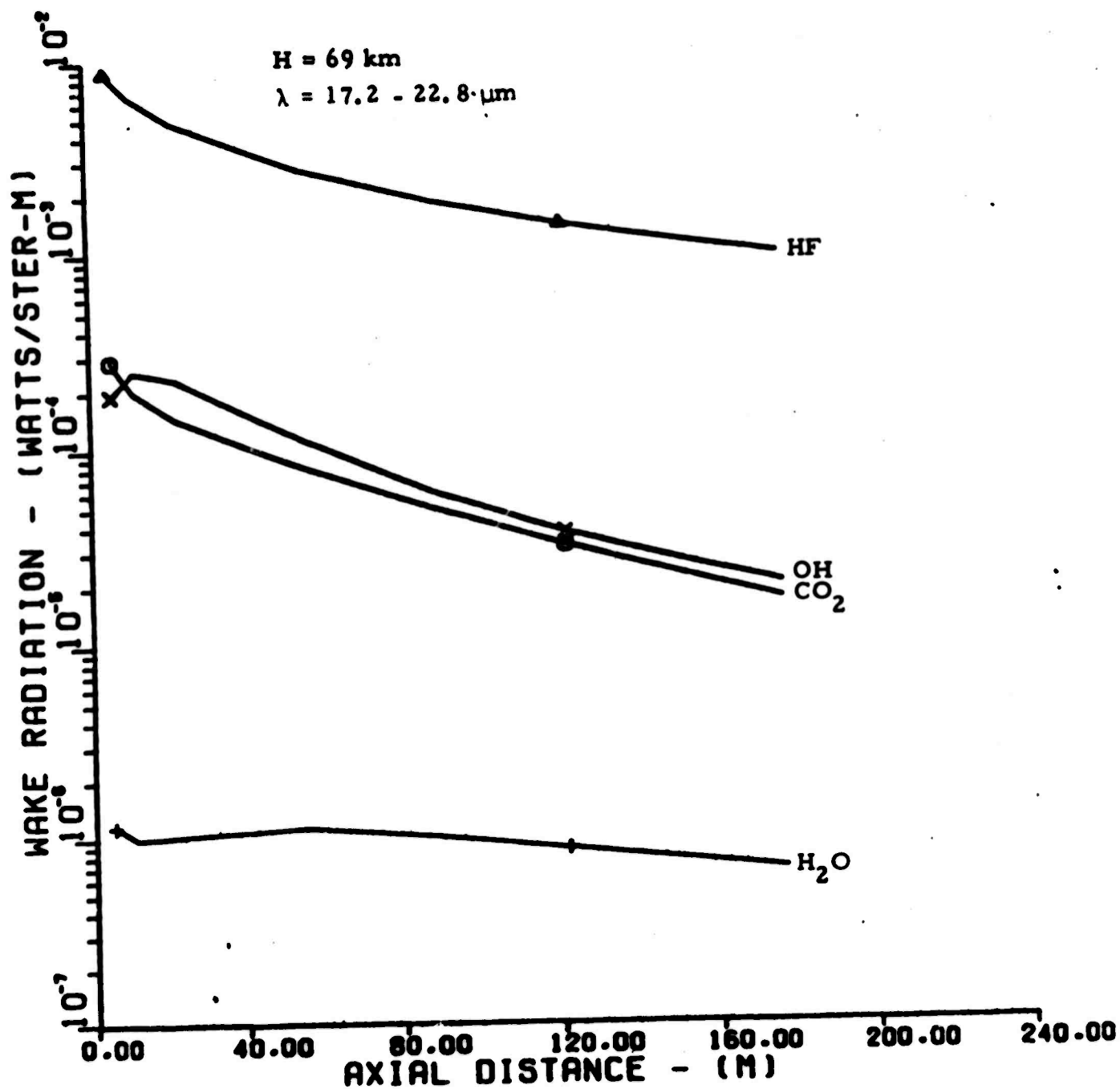
Fig. 16 Wake Radiation vs. Distance for the 17.2 - 22.8 μm Bandwidth,
H = 69 km
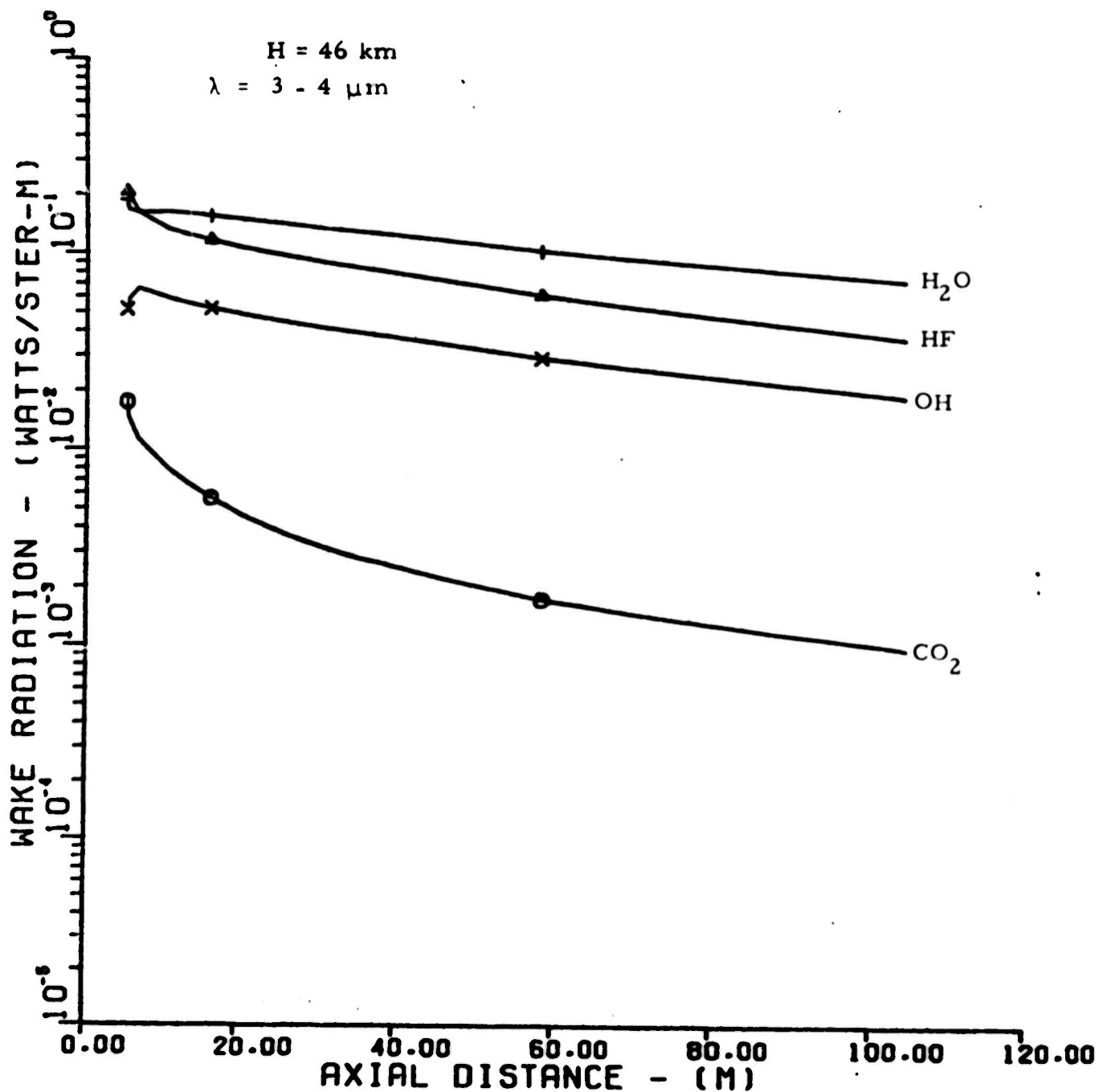
Fig. 17   Wake Radiation vs. Distance for the 3 - 4 μm Bandwidth, H = 46 km
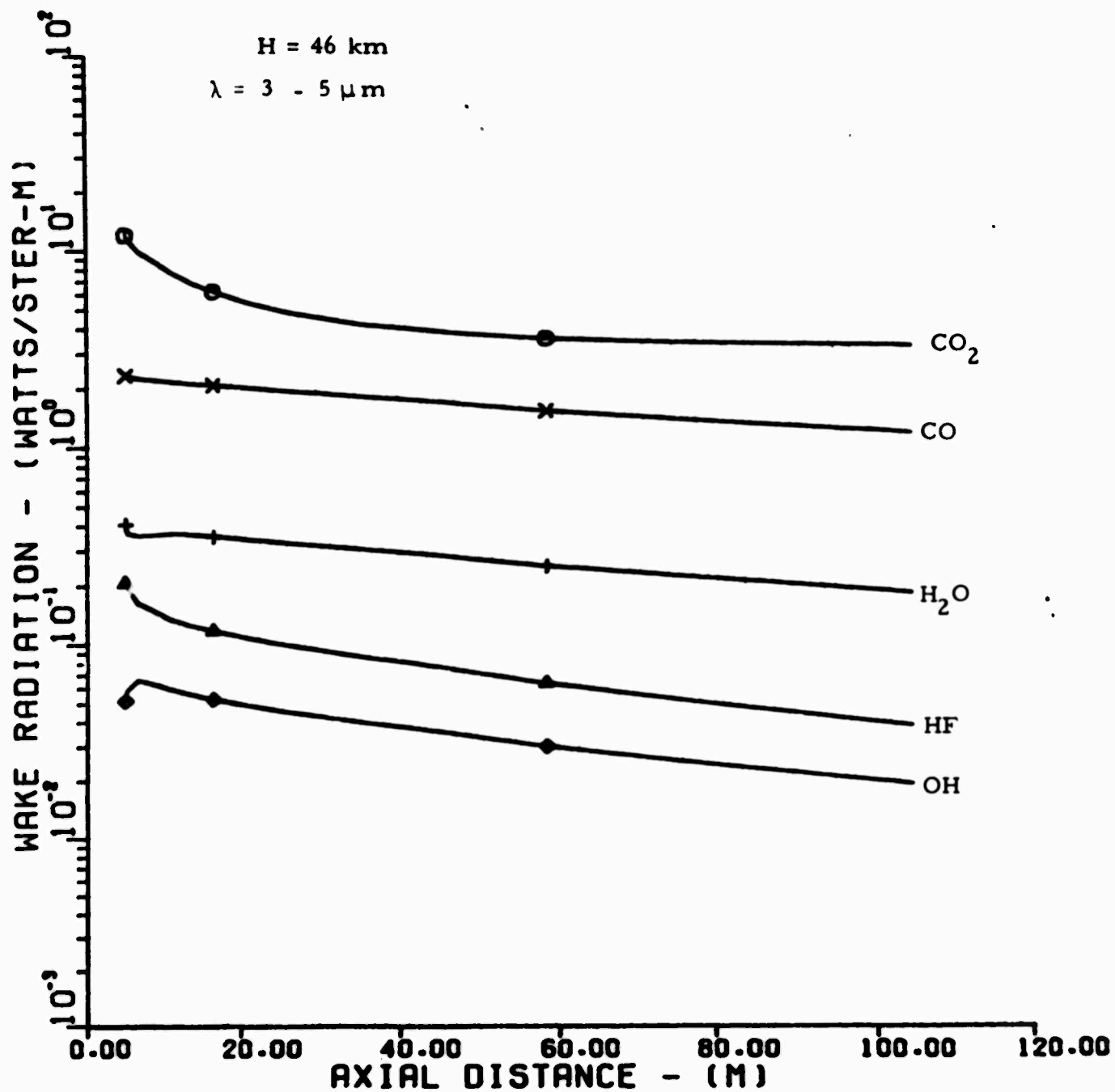
Fig. 18   Wake Radiation vs. Distance for the 3 - 5 µm Bandwidth, H = 46 km
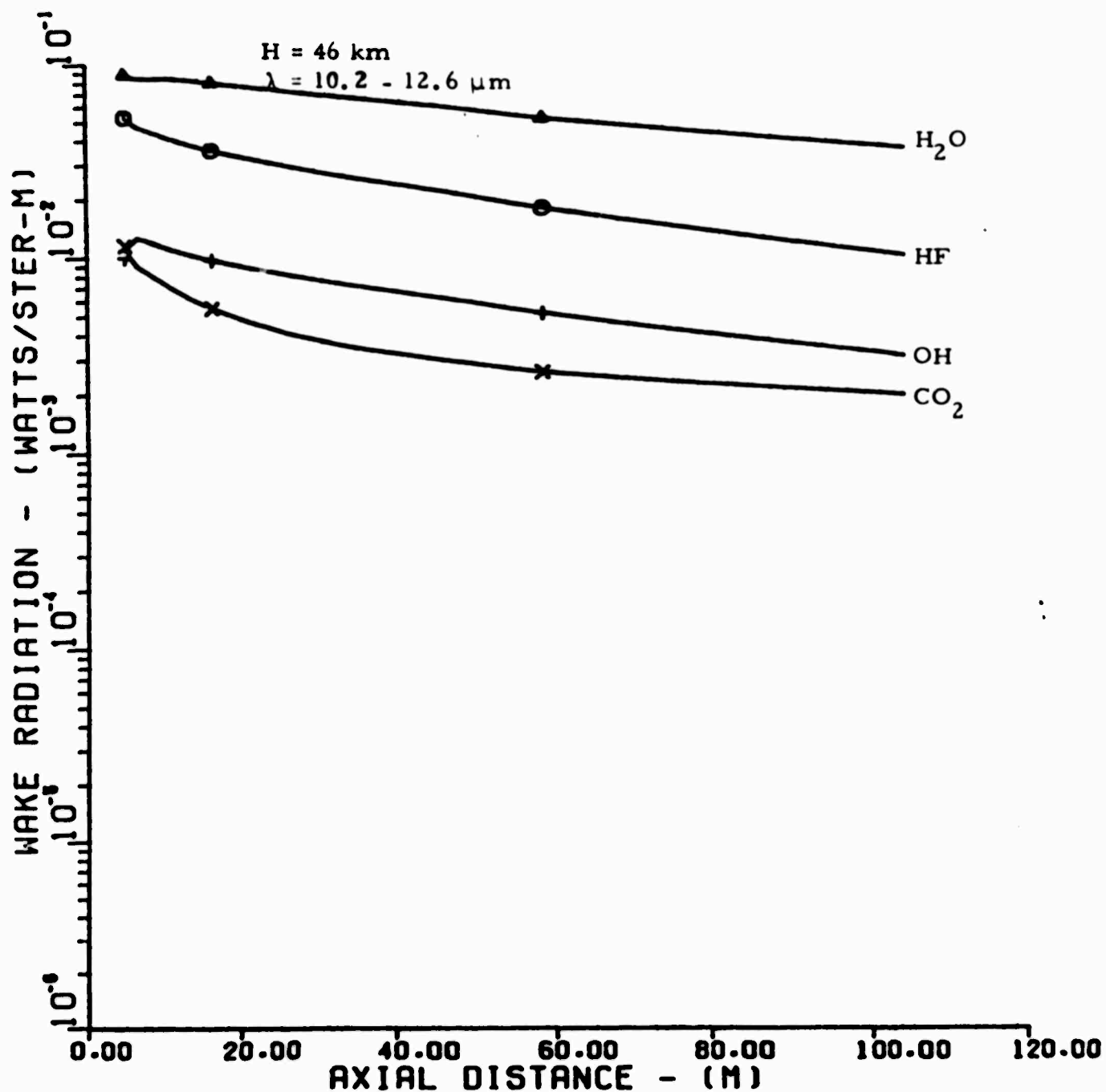
Fig. 19   Wake Radiation vs. Distance for the 10.2 - 12.6 μm Bandwidth,
           H = 46 km.
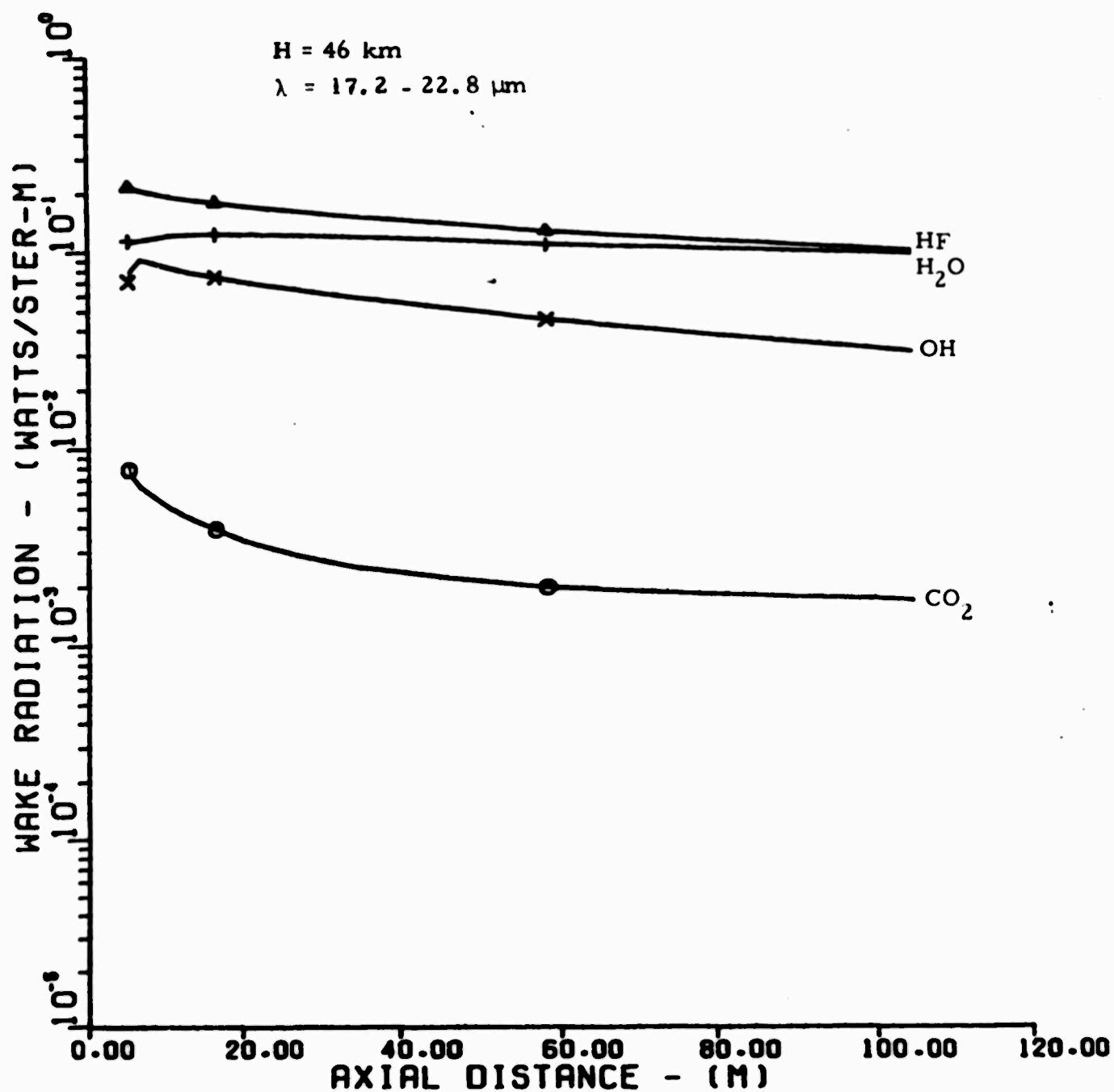
Fig. 20   Wake Radiation vs. Distance for the 17.2 - 22.8 μm Bandwidth,
H = 46 km

total radiation in the $3-5\,\mu m$ bandwidth is typically one to two orders of magnitude higher than that in the $3-4\,\mu m$ bandwidth. Lastly, it should be noticed that radiation from OH is unimportant in all bandwidths.

The situation is somewhat different at 46 km. It can be seen in Fig. 17 that the $H_2O\,(\nu_3)$ band now dominates HF in the $3-4\,\mu m$ band. Furthermore, the H_2O and HF rotational bands are of about equal importance in the $10.2-12.6$ and $17.2-22.8\,\mu m$ band widths. CO and CO_2 are still the dominant radiators in the $3-5\,\mu m$ band and it is to be noted that the radiation histories in the $3-4$ and $3-5\,\mu m$ bandwidths decrease only slightly with distance mirroring the close coupling between vibration and translation.

The laminar wake radiation histories vary uniformly between these two altitudes. The turbulent wake radiation histories which have not been shown exhibit an initial precipitous decrease, resulting from the sharp near wake temperature drop, followed by a low level plateau. The net effect of this behaviour is that the total radiation in the first 100 meters of wake at 38 km is less than that at 46 km. A more detailed discussion of wake radiation predictions for specific re-entry vehicles of interest may be found in a companion report.[11]

III. PARTICULATE RADIATION

A. Introduction

In certain circumstances it may be advantageous to int oduce foreign
substances into the wake of a re-entry vehicle in order to enhance the wake
infrared radiation either in a specific bandpass or over the whole of the
infrared region. Two possible techniques to achieve this goal would be
(1) the injection of foreign gases, and (2) the introduction of particulate
matter into the wake. Much of the phenomenology to be expected in con-
junction with foreign gas injection may be deduced from the previous dis-
cussion on "baseline" wake radiation. In particular, it appears that the
potential radiation available from molecules at high altitudes can be
severely diminished by the effects of collision limiting. Specifically,
a criterion for optimal injectant molecules would be that they be strong
radiators, but conversely, by definition, strong radiators have short
radiative lifetimes and thus would be most affected by collision limiting.

It is the purpose of this section to examine the infrared performance
of particles injected into the wake at high altitudes. Of course it must
first be ascertained as to whether one can achieve the same radiation
per unit mass from particles as from gases. Be it particle or gas,
optimum radiation per unit mass is obtained under optically thin condi-
tions. The absorptivity of small optically thin particles is generally
specified in terms of α, the volume absorption coefficient, which may be
related to the absorption cross section σ_a by the relationship

$$\sigma_a = 4/3 \ \pi R_p^3 \ \alpha \tag{9}$$

where R_p is the particle radius. In general this quantity α must be evaluated
through use of Mie theory and is a function of particle size, wavelength and

the materials' index of refraction. The total radiation from an optically thin particle at a given frequency ν is

$$I_p = 4/3 \; \pi \; R_p^3 \; \alpha \; (2 \; h\nu^3/c^2) \; e^{-h\nu/kT} \tag{10}$$

This is to be compared to the radiation from a molecule having a band centered at frequency ν with bandstrength S in $ama^{-1}\text{-}cm^{-2}$

$$I_M = \frac{S}{N_o \; \Delta\nu} \; \frac{2 \; h\nu^3}{c^2} \; (e^{h\nu/kT} - 1)^{-1} \tag{11}$$

where $\Delta\nu$ is the bandpass of the band and N_o is Loschmidt's number.

Both of these quantities can be converted to radiation per unit mass, J, upon introduction of the particles specific density ρ_p and the molecules molecular weight M. It can then be shown that

$$J_p/J_M = \frac{\alpha \; \Delta\nu \; M}{2.2 \times 10^4 \; \rho_p \; S} \; (1 - e^{-h\nu/kT}) \tag{12}$$

As a specific numerical example take $\Delta\nu = 250 \; cm^{-1}$, M = 100 gms/mole, $\rho_p = 3$ gm/cc, $\nu = 1000 \; cm^{-1}$, and T = 2500°K, values typical of the mid IR and a laminar wake. Thence,

$$J_p/J_M = \alpha / (4S) \tag{13}$$

For the proper choice of particle size, values of α of order $10^4 \; cm^{-1}$ may be readily obtained and furthermore molecular bandstrengths of several thousand $ama^{-1}\text{-}cm^{-2}$ are quite large. Thus, in principle, particles may be used in place of molecules as wake infrared sources with no great increase in weight penalty.

The remainder of this section is concerned with the dynamic and radiative phenomenology of particle/wake interactions. The theoretical analysis of the particle/wake interaction is developed in section B and applied to various scenarios in section C.

B. Flow Modeling

The scenario considered is that of small particles ejected from the base of a re-entry vehicle and having relatively little or no initial velocity relative to the vehicle (thus having a high velocity relative to ground). Since the near wake velocity is low relative to the vehicle velocity, $\sim 0.1\ U_{\infty}$, these particles initially have significantly higher velocity than the wake molecules. Thus, particle/molecule collisions result in momentum and energy exchange which have the net effect of slowing and heating the particles.

The first step in the fluid dynamical modeling is to define the appropriate flow regime of the particle-gas interaction. The flow will be free molecular if the Knudsen number, i.e., the ratio of the gaseous mean free path to particle size, is greater than ten. Probstein[12] has shown that in the case of hypersonic flow the hyperthermal rather than ambient mean free path should be applied. The hyperthermal mean free path is essentially that between ambient molecules and those which have undergone perfectly accommodating collisions with the particle and may be defined by[12]

$$\lambda_H = \frac{V\ (T_p)}{U_{REL}}\ \lambda_a \tag{14}$$

where U_{REL} is the relative velocity between the particle and the ambient gas, λ_a is the ambient mean free path and $V\ (T_p)$ is the mean Maxwellian molecular velocity at the particle temperature T_p. The hyperthermal mean free path is tabulated in Table III for typical initial values of particle temperature and relative velocity. As the particles slow down and heat up, the hyperthermal mean free path will approach that of the wake which is also tabulated. It is clear from Table III that the flow will be free molecular over the full altitude range of interest for particle sizes less than 1 μm. Since, as will be seen, the particle sizes required for optically thin radiation are of the order of 1 μm or less, the remaining analysis will be limited to the free molecular flow regime.

-41-

TABLE III

AMBIENT AND HYPERTHERMAL MEAN FREE PATHS VS. ALTITUDE

$$T = 2500\,^{\circ}K, \quad T_p = 300\,^{\circ}K, \quad U_{REL} = 6 \times 10^5 \; cm/sec$$

H, km	λ_a, cm	λ_H, cm
69	1.1×10^0	8.8×10^{-2}
61	3.0×10^{-1}	2.4×10^{-2}
53	1.2×10^{-1}	9.6×10^{-3}
46	4.4×10^{-2}	3.5×10^{-3}
38	1.5×10^{-2}	1.2×10^{-3}

In the free molecular flow limit the equations governing the heating and deceleration of the particles may be deduced straightforwardly from the equations of conservation of energy and momentum which describe the "hard sphere" collision between the particle and a molecule. The one complication in this analysis is the introduction of the accommodation coefficient α_T. If a collision is perfectly inelastic, that is if after the collision the gas molecule has the temperature and velocity of the particle, the accommodation coefficient is unity. At the other extreme, a completely elastic collision where after the collision the molecule maintains its original temperature and absolute velocity, the accommodation coefficient is zero. These two limits obviously provide for quite different collisional momentum and energy exchanges. Little information on the magnitude of α_T is available although measured values for air/metallic interfaces are near unity[13]. The situation is further complicated by the fact that the different degrees of freedom of the molecule may have different accommodation coefficients and furthermore that the accommodation coefficient may vary with the angle of the collision.

In the analysis to follow it will be assumed that the accommodation efficiency may be defined by the one coefficient α_T. The Schaaf-Chambre[13] model has been used to describe the kinetic phenomenology. This model includes the effect of the Maxwellian velocity distribution of the molecules, assumes the molecular component is a constant bath, and only involves the relative velocity between molecules and particles. The Schaaf-Chambre model has been extended in the present work to include the two additional effects of particle vaporization and radiative loss. Vaporization is also a kinetic process in the free molecular flow regime and the vaporization rate must be defined in terms of a "sticking" coefficient α_v, which is essentially a measure of the fraction of vapor molecules which will adhere to the particle surface upon collision.

If Q is defined as the thermal heat content of the particle, i.e., for a uniform temperature particle

$$Q = 4/3 \pi R_p^3 \rho_p \int C_p \, dT \tag{15}$$

where ρ_p and C_p are the particles density and specific heat respectively, then the particle heating phenomenology is defined by the relationship

$$dQ/dt = dQ/dt \Big|_{COLL.} - dQ/dt \Big|_{RAD} - dQ/dt \Big|_{VAP} \tag{16}$$

where from the Schaaf-Chambre model

$$dQ/dt \Big|_{COLL.} = A(S) (2 R_g T)^{1/2} 4 \pi R_p^2 \rho_g C_{p_g} (T_r - T_p) \alpha_T (\nu + 1)/\nu \tag{17}$$

where T, R_g, ρ_g, C_{p_g} and γ are the gas temperature, specific gas constant, density, specific heat at constant pressure and ratio of specific heats respectively, and S is the normalized relative velocity between the particle and gas, i.e.,

$$S = (U_g - V_p) / (2 R_g T)^{1/2} \tag{18}$$

The quantity $A(S)$ is defined by

$$A(S) = (8 S)^{-1} [S^2 + S \, \mathrm{ierfc}(S) + 1/2 \, \mathrm{erf}(S)] \tag{19}$$

where erf is the error function. T_r is a modified recovery temperature defined by

$$T_r = \left[B(S) \, \frac{\gamma - 1}{\nu + 1} S^2 + 1 \right] T \tag{20}$$

and

$$B(S) = \frac{(2 S^2 + 1)[S^2 + S \, \mathrm{ierfc}(S)] + (2 S^2 - 1) \, \mathrm{erf}(S)/2}{S^2 [S^2 + S \, \mathrm{ierfc}(S) + \mathrm{erf}(S)/2]} \tag{21}$$

(this last expression has been corrected for typographical errors found in the original text[13]).

The radiative loss is defined by

$$dQ/dt\Big|_{RAD} = 4\pi R_p^2 \epsilon (n, R_p, T_p) \sigma T_p^4 \tag{22}$$

where $\epsilon (n, R_p, T_p)$ is the size and temperature dependent particle emissivity which must be deduced by use of Mie theory (which requires knowledge of the complex index of refraction n of the particle material) and σ is the radiation constant, $0.57 \times 10^{-4} \; erg/cm^2/sec/ (^{o}K)^4$.

Lastly the vaporization loss is defined by

$$dQ/dt\Big|_{VAP.} = 4\pi R_p^2 \alpha_v \overline{V} \Delta H_v \rho_v \tag{23}$$

where

$$\overline{V} = (R_v T_p/2\pi)^{1/2} , \tag{24}$$

R_v is the specific gas constant of the vapor, ΔH_v is the heat of vaporization, and ρ_v is the vapor density at the particle surface as defined by the Clausius -Clapeyron relationship, i.e.,

$$\rho_v = P_B/(R_v T_p) \exp [\Delta H_v (T_p - T_B)/ (R_v T_p T_B)] \tag{25}$$

where $P_B = 10^6 \; dynes/cm^2$ and T_B is the normal boiling temperature of the particle material.

With the definitions of Eqs. (17) to (23), Eq. (11) simplifies to

$$d T_p/dt = 3 (C_p \rho_p R_p)^{-1} \left\{ A(S) (2 R_g T)^{1/2} \rho_g C_{P_g} \alpha_T (T_r - T_p) (\gamma + 1)/\gamma \tag{26} \right.$$
$$\left. - \epsilon (n, R_p, T_p) \sigma T_p^4 - \alpha_v \overline{V} \Delta H_v \rho_v \right\}$$

where it is to be noted that, with the exception of the emissivity, the heating

-45-

rate is inversely proportional to particle size.

The remaining equations required to define the particle/gas inter-action are the momentum equation

$$d V_p/dt = 3 C_D (S) (8 \rho_p R_p)^{-1} \rho_g (U_g - V_p)^2 \qquad (27)$$

where C_D is a modified drag coefficient defined by the Schaaf-Chambre model as

$$C_D (S) = S^{-3} [(4S^4 + 4S^2 - 1) erf(S)/(2 S) + (2 S^2 + 1) \pi^{-1/2} e^{-S^2/2}]$$

$$+ 2/3 \alpha_T S^{-1} (\pi T_p/T)^{-1/2} \qquad (28$$

and the equation for the rate of change of particle size resulting from vaporization

$$d R_p/d t = - \alpha_v \overline{V} \rho_v/\rho_p \quad . \qquad (29)$$

It is to be noted that the phenomenon modeled is only dependent upon the relative velocity between particle and molecules. For simplicity the above equations have been derived in a coordinate system where the initial particle velocity is zero. This coordinate system is the equivalent to body centered coordinates when the particles are injected initially at rest rela-tive to the body. In this case

$$U_g = U_\infty - U_w \qquad (30)$$

where U_∞ is the body velocity and U_w the wake velocity, which is typically $\sim 0.1 U_\infty$ in the near laminar wake. In this instance time may be directly related to distance behind the body by the relationship

$$x(t) = \int\limits_{o}^{t} V_p \, dt \quad . \tag{31}$$

If the particles are injected with a finite velocity U_p relative to the body then Eqs. (30) and (31) must be replaced by

$$U_g = U_\infty - U_p - U_w \tag{32}$$

and

$$x(t) = U_p t + \int\limits_{o}^{t} V_p \, dt \; . \tag{33}$$

Eqs. (26) - (33) with all peripheral definitions have been computer programmed and the model has been exercised for a number of scenarios as discussed in the next section.

C. Particle Heating and Radiation Predictions

The desired end result of this analysis is a prediction of the near wake infrared radiation history of specific particles. The choice of particle material and size will of course be dictated by the application. As alluded to earlier there are two distinct forms of infrared wake enhancement which are of interest. The first of these, spoofing, involves introducing an additive which will increase the IR radiation in one of the atmospheric windows but not in the others, for example, introducing a species which will radiate in the 10 - 12 μm but not in the 3-5 μm wavelength region. Spoofing is a possible countermeasure to the use of two channel infrared discriminants as is discussed in some detail in the companion report[11]. The alternate technique is masking which requires an additive which will radiate strongly throughout the entire infrared. The purpose of this technique is to provide an additional IR radiation source which will exceed that of the total uncontaminated body and near wake radiation.

Particulate materials can readily be specified to satisfy either of these criteria. For example, the infrared spectral volume absorption co-efficients for pure SiO_2, Al_2O_3 and carbon are shown in Fig. 21. These volume absorption coefficients have been calculated in the Rayleigh limit corresponding to particle sizes much smaller than the radiation wavelength. In this limit α is related to the materials complex index of refraction n by the relationship

$$\alpha = - \frac{6\pi}{\lambda} I_m \left\{ \frac{n^2 - 1}{n^2 + 2} \right\} . \tag{34}$$

Detailed information on the spectral variation of the complex index of refraction of various materials is generally hard to locate and is clearly an area which requires more research. The values of the complex index of refraction used in evaluating Eq. (34) were taken from various sources and do exhibit uncertainties although the general spectral variations are correct. The data for Al_2O_3 was taken from the review of Gal and Kirch[14] and are appropriate for a temperature of 2000°K. The data for SiO_2 is from
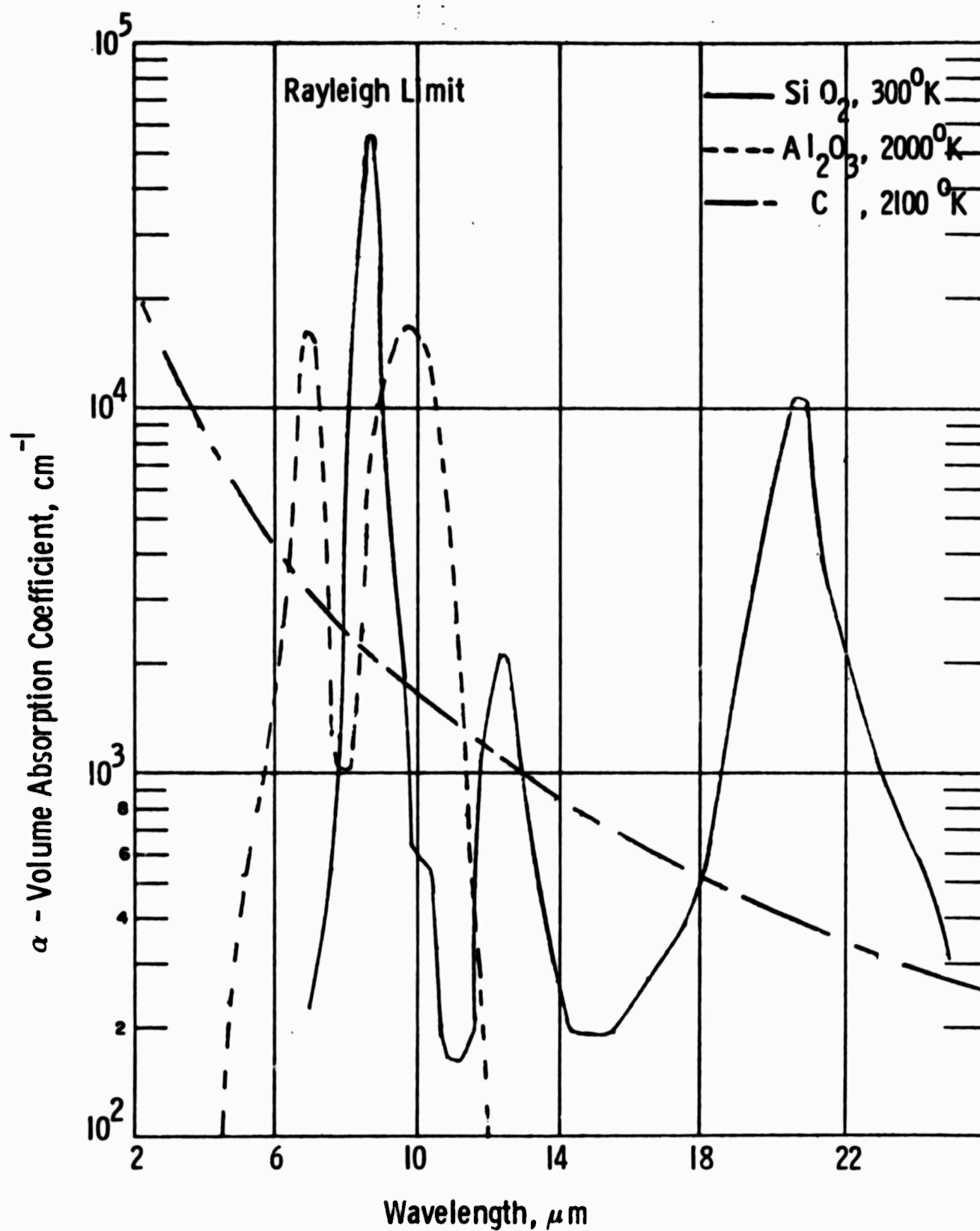
Fig. 21   Volume Absorption Coefficients of Al_2O_3, SiO_2 and Carbon vs. Wavelength   in the Rayleigh Limit.

the recent study of Steyer et al[15]; the complex index of refraction of this material is only available at room temperature. Lastly, the values for carbon were taken from the work of Stull and Platz[16] and are appropriate for a temperature of $2100^O K$.

The main point to be deduced from Fig. 21 is that the materials SiO_2 and Al_2O_3 exhibit a very structured spectra in the infrared, much like gas phase radiators, whereas species such as carbon have very smooth infrared spectra. Thus materials such as the former are candidates for use in spoofing whereas materials such as carbon would be used for masking applications. (It should be mentioned that the data shown in Fig. 21 are for pure materials and that impurities can act to wash out much of the structure in the displayed spectra). Since the desired material properties for masking are quite different than those for spoofing the two topics are discussed separately below.

1. Spoofing

The literature was reviewed in order to identify that material which both radiates strongly in the region of the 10 - 12.5 μm atmospheric window and very weakly in the 3 - 5 μm region. Unfortunately, the data base is very sparce and the optimal material has not yet been identified. The material Al_2O_3 comes close to satisfying these requirements and has been used as a representative material in the present calculations. The available data on the complex index of refraction of Al_2O_3 has recently been reviewed by Gal and Kirch[14] and is reasonably well defined for temperatures below the melting point, $2320^O K$, although it is quite uncertain at higher temperatures.

The predicted spectral variation of the volume absorption coefficient of Al_2O_3 in the region of the 10 - 12.5 μm atmospheric window is shown in Fig. 22. The predictions are for a temperature of $2000^O K$ and particle radii varying from 0.5 - 5 μm and were deduced from the Mie theory absorption efficiency calculations of Gal and Kirch[14]. These calculations were performed at 1 μm intervals and have been arbitrarily connected by straight lines thus causing the jagged appearance of the curves. Note that
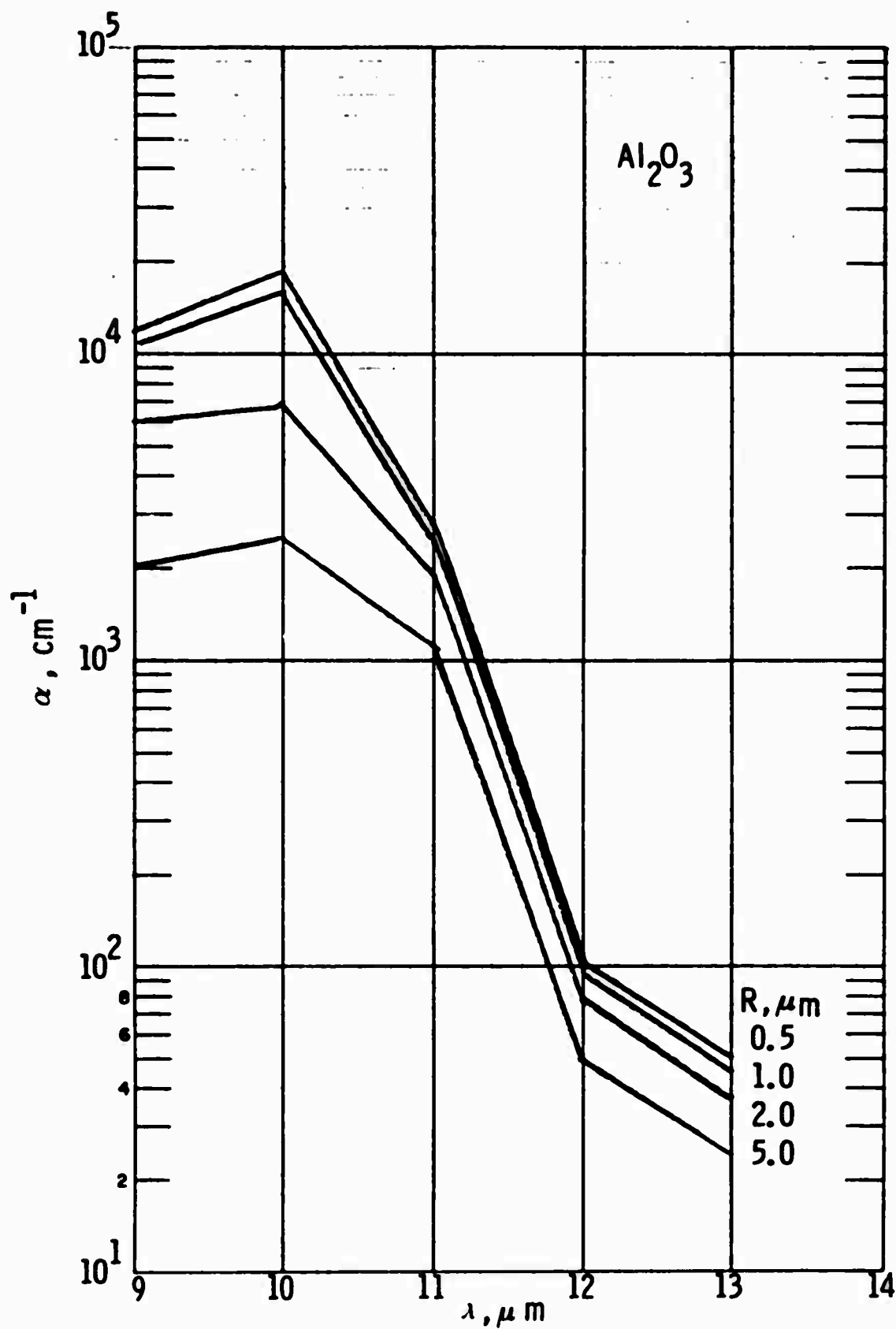
Fig. 22   Volume Absorption Coefficient of Al_2O_3 vs. Wavelength for
Several Particle Sizes, $T = 2000°K$

for particle rad i larger than 1.0 μm the absorption coefficient decreases approximately inversely with particle size. This decrease is due to optical thickness effects and thus true volume absorption is only obtained with Al_2O_3 for particle radii ≤ 1 μm.

This effect may also be seen in the temperature dependent emissivity of Al_2O_3 shown for particle sizes between 0.5 - 5 μm in Fig. 23. These predictions were also taken from the work of Gal and Kirch[14]. The dashed line intercepts to the predictions for radii of 0.5 μm and 5.0 μm represent the extent of the previously alluded to uncertainty in the index of refraction at temperatures above $2000^{\circ}K$. It is to be noted that the emissivities of 2 and 5 μm radius particles are approximately equal, a behaviour appropriate for "gray" bodies. For 1 μm and below however the emissivity scales approximately inversely with particle radius as would be expected for a volume absorber.

Although the Al_2O_3 absorption coefficient does not peak in the 10 - 12.5 μm region, see Fig. 22, it is still fairly large in the region of 10 - 11 μm and thus can provide significant radiation in the desired band-pass. From Figs. 22 and 23 it may be deduced that optimum radiation/unit mass may be obtained for particle radii 1 μm or smaller. It will be recalled from Table III that the flow of 1 μm particles will be in the free molecular regime at altitudes ≥ 38 km.

A series of predictions for the heating and radiation histories of 1 μm radius alumina particles have been developed over the altitude range of 69 - 38 km. The scenario considered was that of cold particles (T = $300^{\circ}K$) injected initially at rest relative to the body into a constant temperature and velocity laminar wake. The gas properties were taken to be that of heated air of temperature $2500^{\circ}K$. A nominal reentry velocity of U_{∞} = 6.6 km/sec was chosen which, assuming that $U_w \approx 0.1\ U_{\infty}$, corresponds to an initial body centered gas velocity of $U_g \approx$ 6 km/sec. The thermodynamic properties of alumina were taken from the JANAF tables[17]. The heat of vapori-

-52-
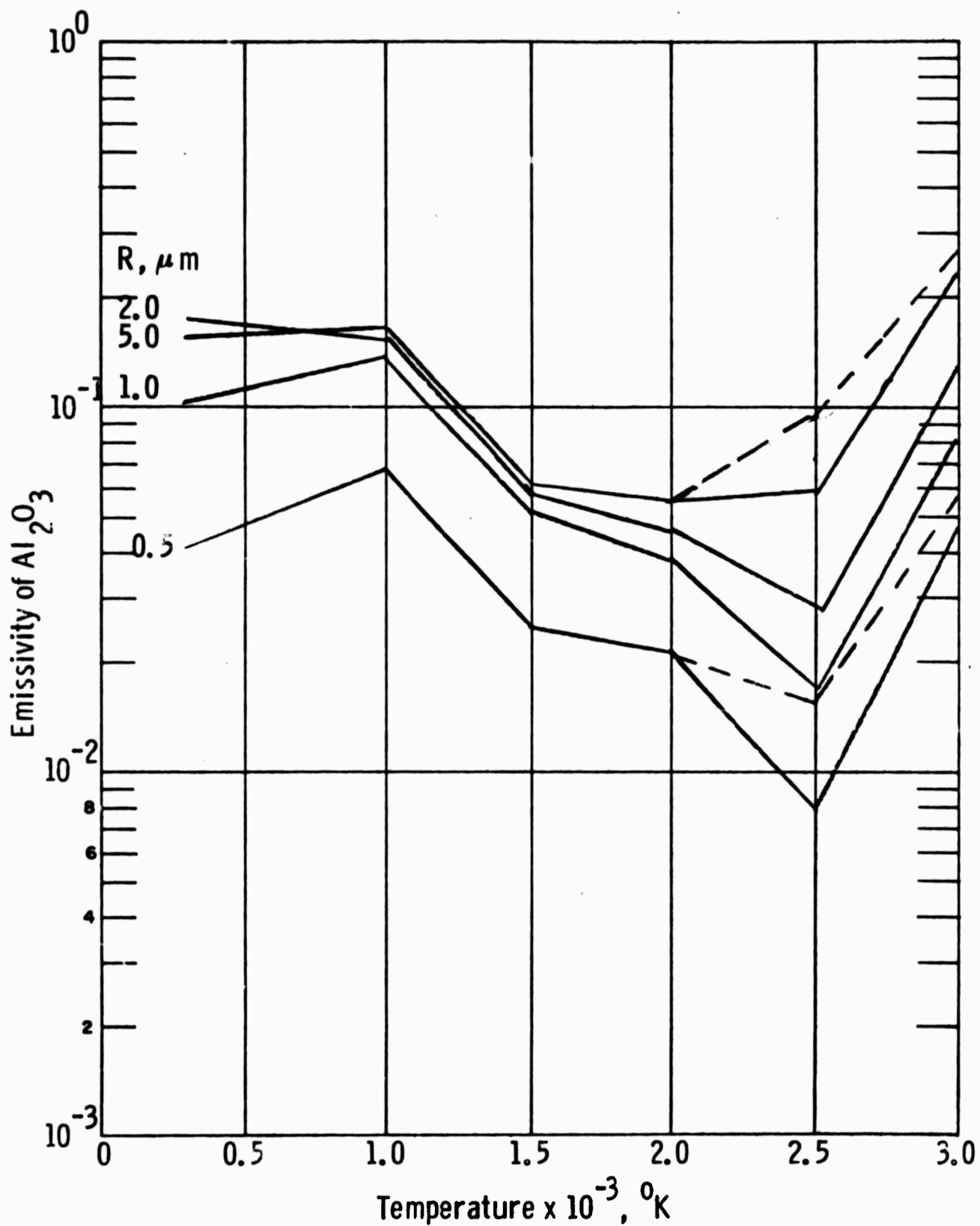
Fig. 23 Total Emissivity of Al_2O_3 vs. Temperature for Several Particle Sizes

ization of Al_2O_3 was not readily available and was estimated from Trouton's rule [18] to be 860 cal/gm for a boiling temperature of $3600^\circ K$. One feature peculiar to alumina is a very high enthalpy of melting, ~280 cal/gm. Since the intention of the calculations is to provide an estimate of the generic behaviour of typical materials the heat of melting was taken to be zero in the present calculations.

Predicted particle temperature histories for the altitudes of 69, 53 and 38 km are displayed in Figs. 24 - 26 respectively. These predictions have been performed under the assumption that the thermal accommodation coefficient α_T is unity. At all three altitudes three distinct cases were considered in order to delineate the importance of the various losses. In each figure the highest temperature curve corresponds to the case of no radiation or vaporization losses, the next lowest curve to radiative loss only, employing the Al_2O_3 emissivity shown in Fig. 22, and lastly, the lowest temperature curve corresponds to the inclusion of both vaporization and radiation losses with the sticking coefficient α_v taken to be unity. The particle velocity scale shown at the top of each figure is specific to the case of both radiation and vaporization losses. However, the velocity histories of the other two cases are not significantly different.

Examining first Fig. 24, corresponding to an altitude of 69 km, it can be seen that the initial particle heating is approximately the same for all three cases with losses not becoming important until the particle temperature reaches ~ $1800^\circ K$. Furthermore, if there were no losses the particle temperature would continue to increase to temperatures well above the wake temperature. As can be seen this behaviour is severely affected by the inclusion of radiative losses. Indeed the temperature profile for this case peaks about 40 meters downstream even though there is still a large velocity difference between the gas and particle. The inclusion of vaporization decreases the temperature even more, so that at this altitude the peak particle temperature remains below the wake temperature.
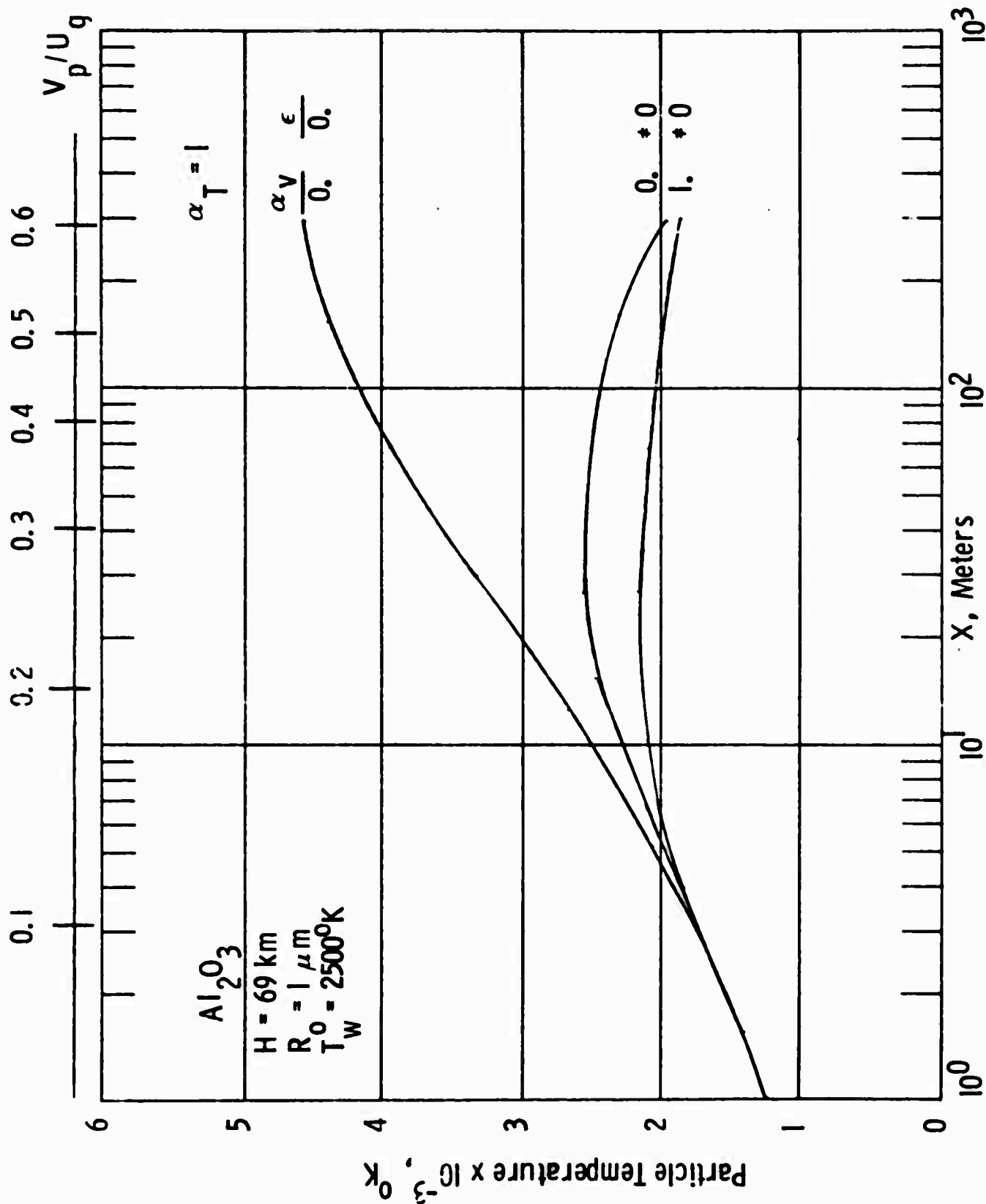
Fig. 24 Predicted Al_2O_3 Particle Temperature vs. Distance, $H = 69$ km
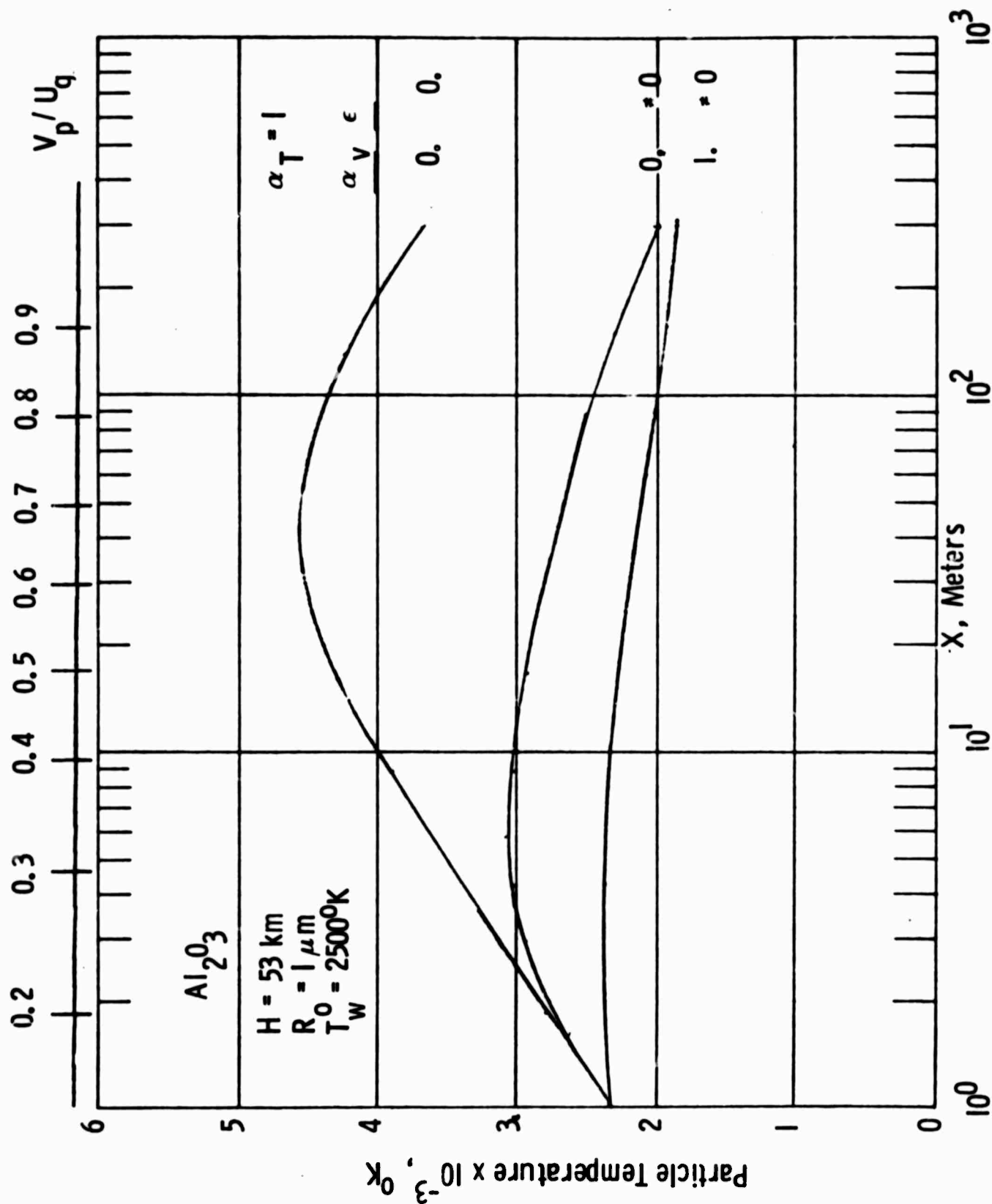
Fig. 25 Predicted Al_2O_3 Particle Temperature vs. Distance, $H = 53$ km
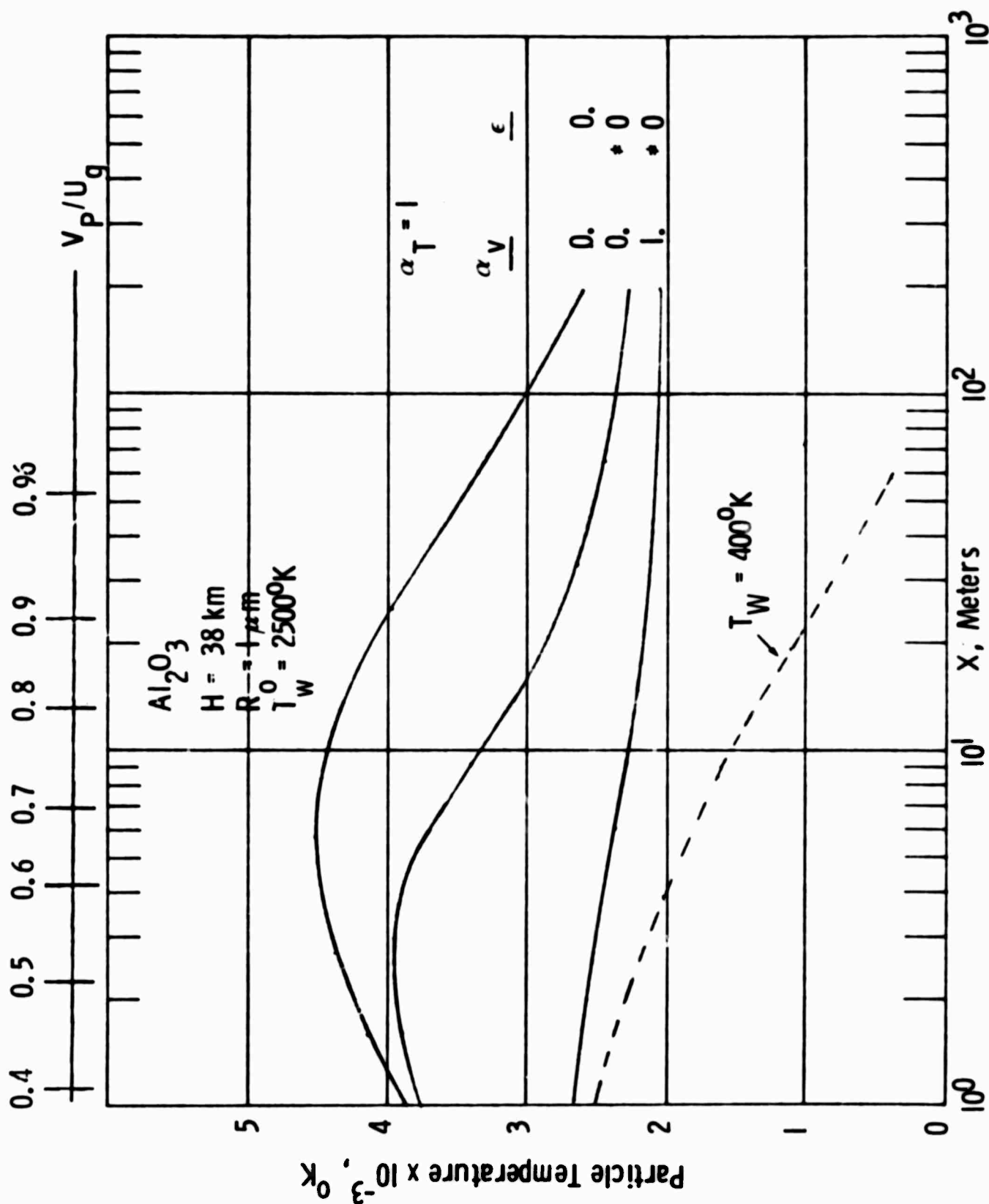
Fig. 26 Predicted Al_2O_3 Particle Temperature vs. Distance, $H = 38$ km

In Fig. 25, corresponding to an altitude of 53 km, the differences between the three curves are enhanced. Because of the increased gas density the velocity difference between particle and gas diminishes more rapidly with distance. It can be seen that even the predicted temperature for the case of no losses reaches a peak value and then decreases. This occurs because the particle temperature is higher than that of the wake and thus the particles can lose energy by increasing the molecule temperature in perfectly accommodating collisions. If this calculation had been carried to larger distances the particle temperature would of course asymptote to the wake temperature.

It is interesting to note that the predicted temperature history for the case of radiative losses only is actually higher at this altitude than at 69 km. This seemingly contradictory behavior occurs because the particle velocity equilibrates more rapidly with decreasing altitude. Thus a particle takes less time to reach a given distance downstream as the altitude decreases and therefore has less time to radiate the excess particle heat energy away. This effect is not so apparent when vaporization is included since a small change in temperature can produce a large change in vapor pressure and thus in the vaporization rate. Indeed this latter effect which is controlled by the heat of vaporization and the boiling temperature of the material, see Eqs. (23) - (25), ultimately provides the limitation on maximum achievable Al_2O_3 particle temperatures.

Similar behaviour is shown in Fig. 26 for an altitude of 38 km. An additional prediction for a wake temperature of $400^{\circ}K$ has been provided at this altitude as a simulation for possible particle behaviour in a turbulent wake. Note that in this case the particle is rapidly heated to temperatures of $\sim 2500^{\circ}K$ and then slowly decays to the wake temperature within the first one hundred meters of wake. The velocity scale shown on this figure is only appropriate for the laminar wake cases since the "turbulent" wake prediction necessarily corresponds to a higher gas density .

-58-

These calculations may now be applied to the prediction of particle radiation. (In performing such predictions it is to be remembered that the particles decrease in size through vaporization. For the range of altitudes shown the particles decrease at most to 70% of their original size in the first 100 meters of wake.) The total particle radiation in the 10 - 12.5 μm bandwidth for optically thin particles is defined by the relationship

$$I_p = 4/3 \ \pi \ R_p^3 \int_{10\mu m}^{12.5\mu m} \alpha \ j \ (\lambda, \ T_p) \ d\lambda \tag{35}$$

where

$$j = 2 \ h c^2 \ \lambda^{-5} \ e^{-hc/(\lambda k T)} \tag{36}$$

and where the spectral variation of α is as shown in Fig. 22. For purposes of calculation it is convenient to express the intensity in terms of an average value of α over the bandpass, i.e.,

$$I_p = 4/3 \ \pi R_p^3 \ \overline{\alpha} \ j \ (11.25 \ \mu m, \ T_p) \ \Delta\lambda \tag{37}$$

where $\Delta\lambda$ is the bandwidth. It can be shown that for Al_2O_3 at temperatures of a few thousand degrees $^{\circ}K$ the average value of α satisfying Eqs. (35) - (37) is 5000 cm^{-1}. (Note however that some 93% of this radiation will fall between 10 - 11 μm.)

The predicted 10 - 12.5 μm particle radiation histories for the altitudes considered are displayed in Fig. 27. The particle radiation is
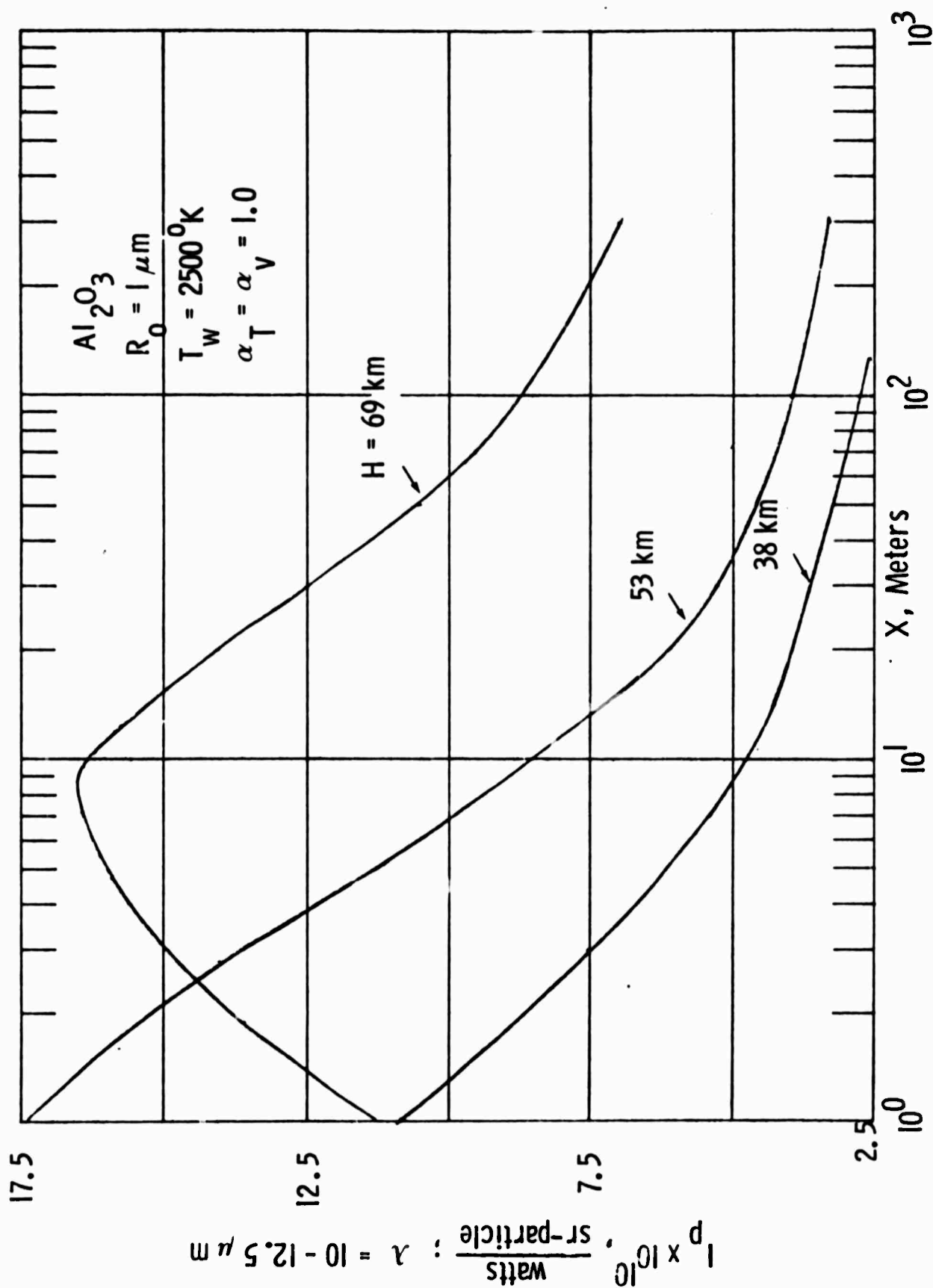
Fig. 27 Radiation Per Particle in the 10 - 12.5 μm Bandwidth vs. Distance. Both radiation and vaporization losses included.

highest in the near wake and decreases with increasing distance. This decrease is not primarily due to decreasing particle temperature. Indeed it can be seen from Figs. 24 - 26 that the particle temperature varies only slightly in the first 100 meters of wake. Rather it is due to the decreasing particle size since the radiation scales as the cube of radius. This phenomenon of particle shrinkage has obvious advantages for applications where it is desired to enhance the infrared radiation in the near wake but not in the far wake.

One additional matter that can be addressed is the particle radiation resulting from the injection of a constant mass flow $\dot{m}_p$ of particles into the wake. This cannot be deduced by a simple scaling of the results in Fig. 27. Although the particle mass flux is not conserved in the wake, because of vaporization, the total number flux of particles $\dot{N}_p$ is conserved. However, since the particle velocity varies with distance, the local particle density N_p must also, i.e.,

$$\dot{N}_p = N_p \, V_p \, \overline{A} \tag{38}$$

where $\overline{A}$ is the cross-sectional area over which the particles are disseminated. Thus for a constant mass flow injection rate the number of radiating particles per unit length of wake will scale inversely with particle velocity.

As a numerical example radiation predictions have been provided at various altitudes for initial injection rates which produce a total irradiation of 20 w/sr in the first 30 meters of wake. The required $\dot{m}_p$ to satisfy this criterion is deduced from the relationship

$$\dot{N}_p \int_0^{30\,m} I_p / V_p \, dx = 20 \text{ w/sr} . \tag{39}$$

The resulting radiation histories along with the required injection mass flows for 1 μm alumina particles are displayed in Fig. 28. It can be seen that the
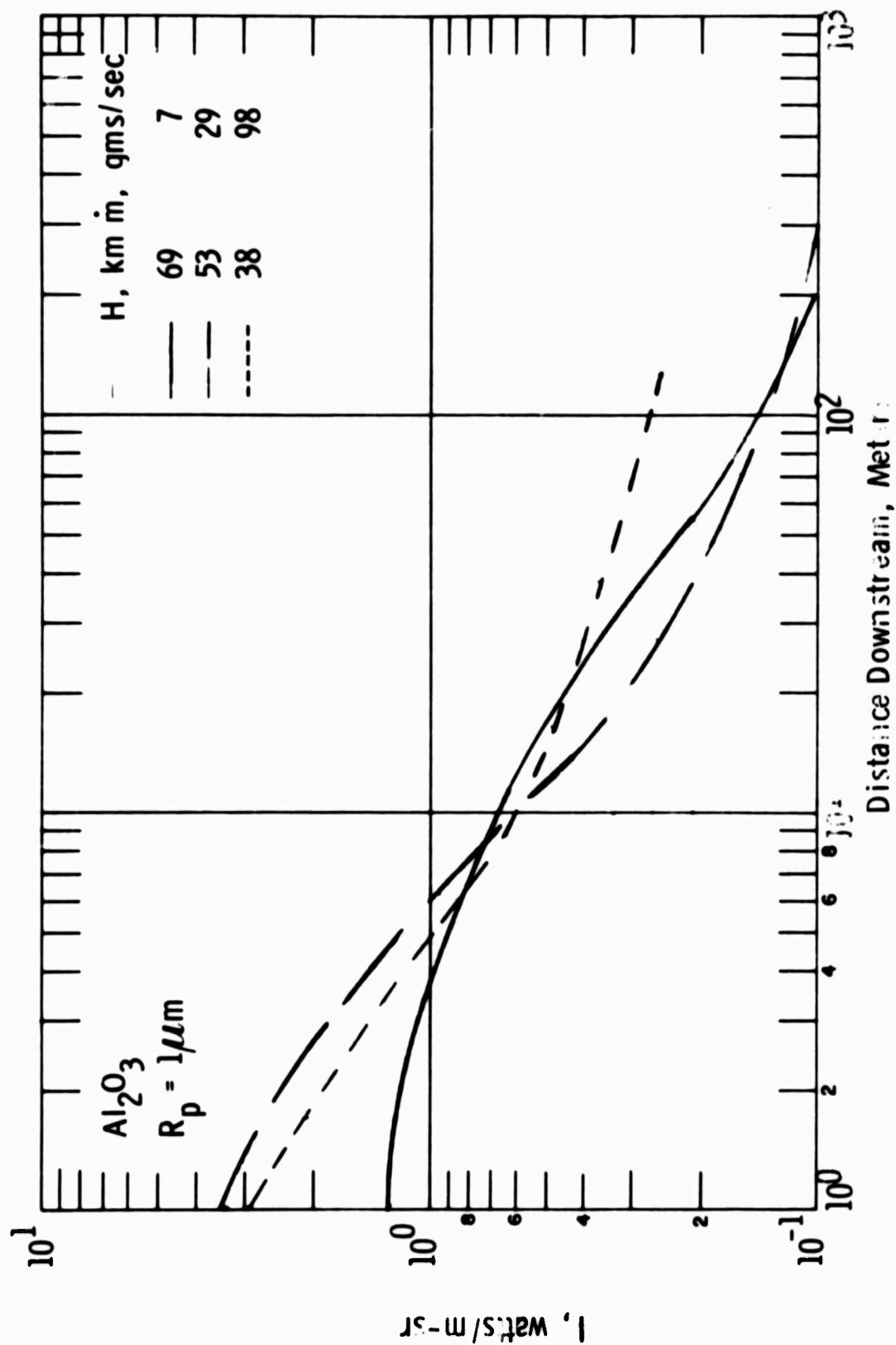
Fig. 28 Al_2O_3 Particle Radiation in the 10-12.5 um Bandwidth vs. Distance for the Case of Constant Mass Flow.   Mass injection rates as specified.

required $\dot{m}_p$ scales inversely with altitude reflecting the increased rates of
both velocity equilibration and vaporization which occur with decreasing altitude.

2. Masking

There has to date been no detailed study performed to determine which
particle properties such as size, emissivity and specific density, will lead to
optimum radiation per unit mass for masking applications. In the present
analysis two specific particle types have been arbitrarily chosen in order to
examine the altitude dependent infrared radiation histories of strongly
radiating particles. The two cases considered are (1) 5 um radius carbon
particles which exhibit an emissivity of approximately unity throughout the
IR and (2) 0.55 μm radius zirconia particles having a characteristic constant
emissivity of 0.22 in the IR.

The thermodynamic properties of these two materials were taken from
the JANAF tables[17]. Carbon has a boiling temperature (more properly sub-
limation) of $4500^{o}K$ and a heat of vaporization of 171 kcal/mole while the
respective values for ZrO_2 are $4550^{o}K$ and 149 kcal/mole. It was found
in the course of the calculations that these boiling temperatures are suffi-
ciently high so that vaporization plays essentially no role in the particle
heating phenomenology.

The approach taken in performing the masking predictions was quite
distinct from that of the spoofing analysis of the previous section. Masking
is best achieved by employing a device for the generation of hot particles
so that a radiation signature can be provided at very high altitudes (exo-
atmospheric) where heating by the particle/gas interaction is negligible.
In this high altitude vacuum limit the total radiation attainable from the
particle is essentially equal to its initial heat content at the time of injection.
The present calculations were directed towards determining the degree of
enhancement of this vacuum limit radiation which can result from the gas/
particle interaction under endo-atmospheric conditions. To this end calcula-
tions were performed over the altitude range of 91 - 61 km under the assump-
tions of an initial particle temperature of $1840^{o}K$ and an initial particle
separation velocity (from the body) of 0.6 km/sec. Wake conditions were

-63-

taken to be those of 2500°K air with U_g = 6 km/sec (see Eqs. (32) - (33)).

The predicted temperature histories for 5 μm radius carbon particles at altitudes of 91, 76 and 61 km, and in the vacuum limit are shown in Fig. 29. As can be seen there is little difference between the predictions at 91 km and the vacuum limit implying that the gas/particle interaction is unimportant at this altitude. The particle temperatures are enhanced at the lower altitudes shown although the particle temperature is everywhere lower than the wake temperature.

IR radiation predictions for these altitudes for wavelengths of 1, 5 and 15 μm are shown in Figs. 30 - 32 respectively. These predictions are for the total integrated radiation at a given wavelength per unit particle mass flow K_λ vs. distance, where

$$K_\lambda = \frac{3\epsilon}{\rho_p R_p} \int_0^X N_\lambda / V_p \, dx \tag{40}$$

where ϵ is the emissivity and N_λ the black body function (the units of K_λ are joules/(gm-sr-μm)). As can be seen the radiation enhancement factor is a strong function of wavelength being as large as a factor of 6 at 1 μm and close to unity at 15 μm. This wavelength dependence is primarily a result of the spectral variation in the black body function at the temperatures of interest.

Predicted temperature histories for 0.55 μm ZrO_2 particles are shown in Fig. 33 for the same altitude range. The displayed zirconia temperatures are somewhat higher than those shown earlier for carbon. Indeed, close to the body, the particle temperature exceeds the wake temperature at 61 km altitude. The corresponding mass flow normalized radiation predictions for wavelengths of 1 and 5 μm are shown in Figs. 34 and 35 respectively. It can be seen that the radiation enhancement factor is considerable in this case, being as much as a factor of 60 at 1 μm. Although not shown the radiation predictions at 15 μm exhibit negligible radiation enhancement much like the predictions for carbon particles.

Fig. 29 Predicted Carbon Particle Temperature vs. Distance at
Several Altitudes.
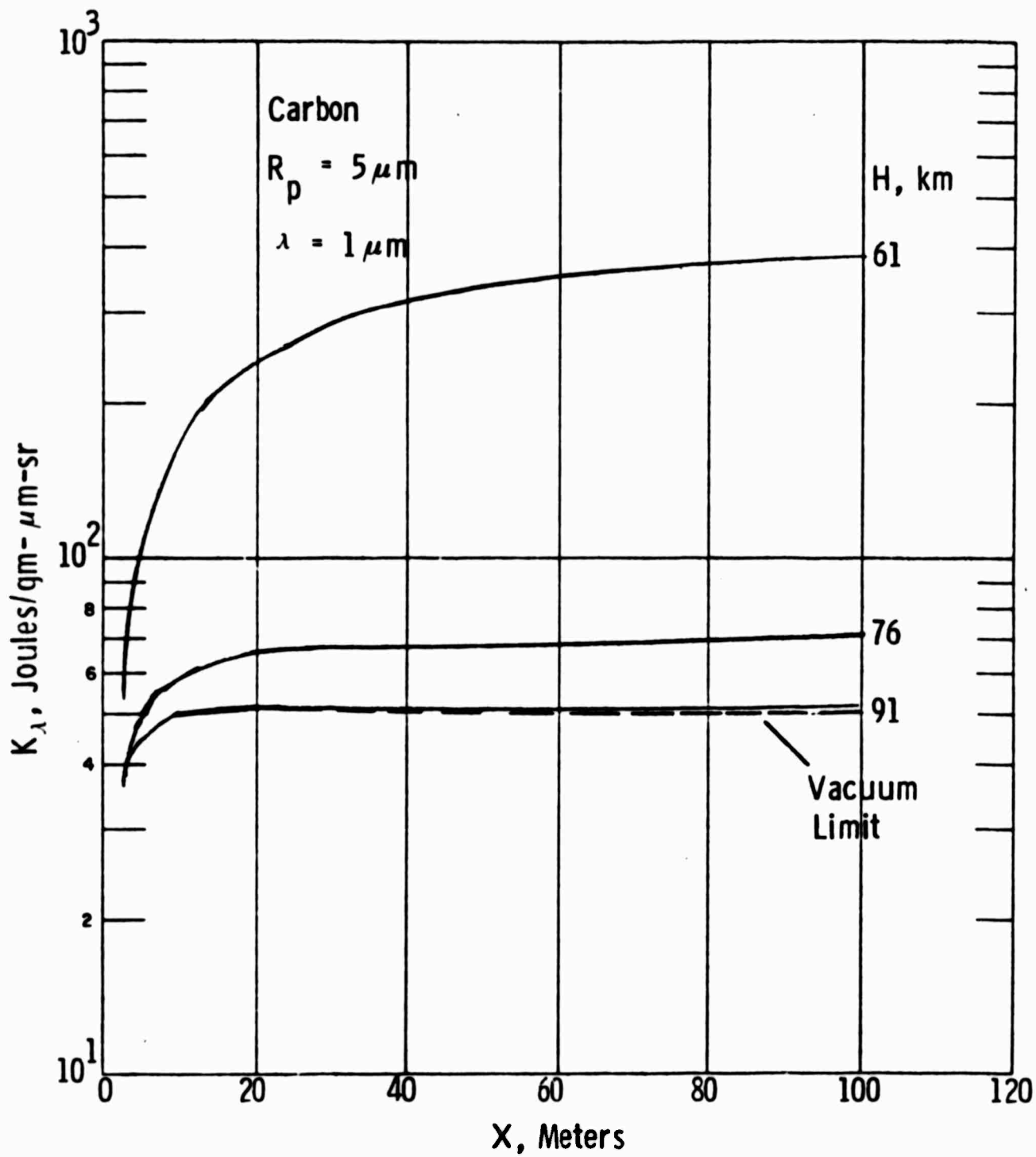
Fig. 30   Integrated Carbon Particle Radiation Per Unit Mass Flow vs.
Distance, $\lambda = 1\,\mu m$
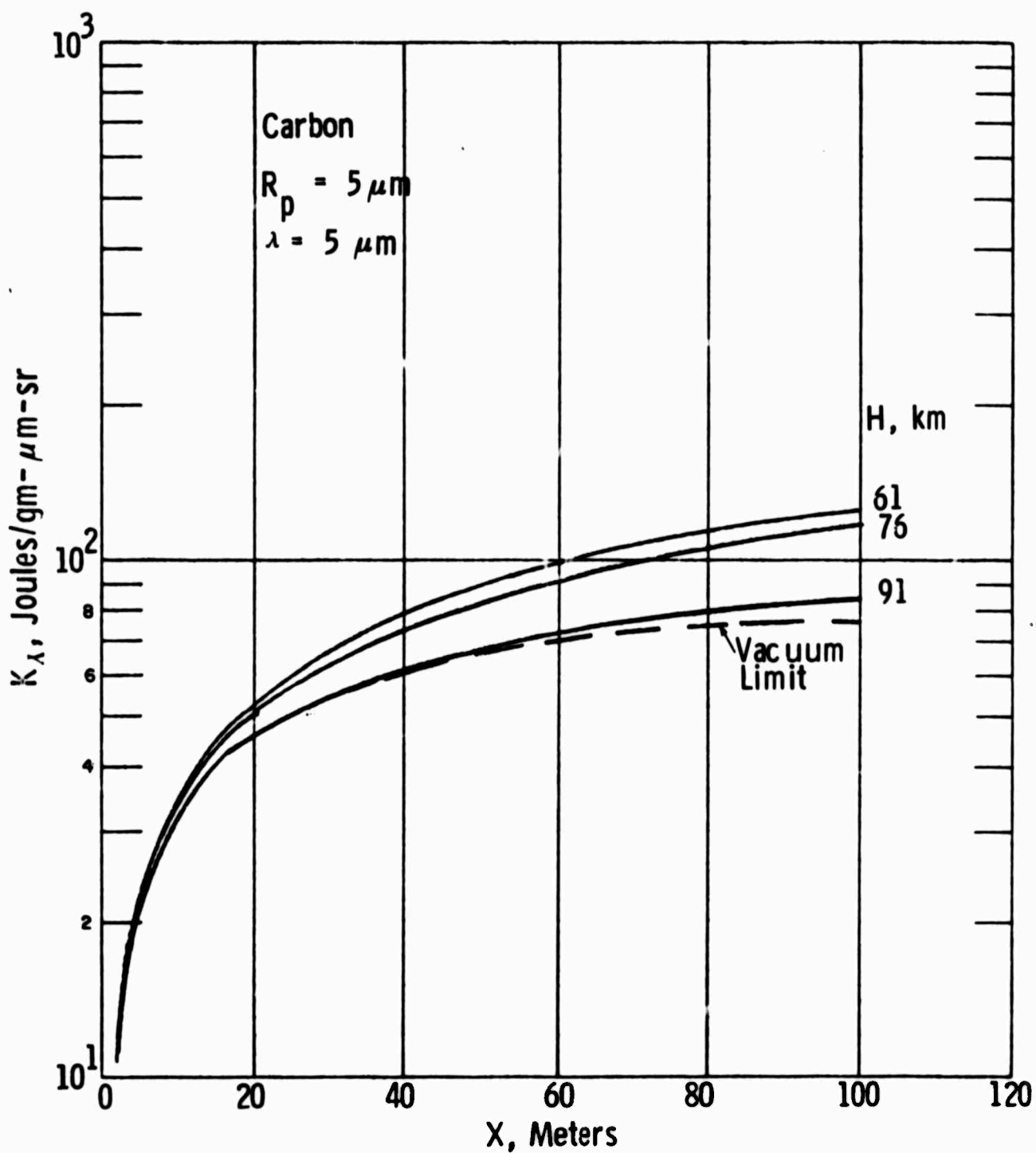
Fig. 31 Integrated Carbon Particle Radiation Per Unit Mass Flow vs.
Distance, $\lambda = 5\ \mu m$
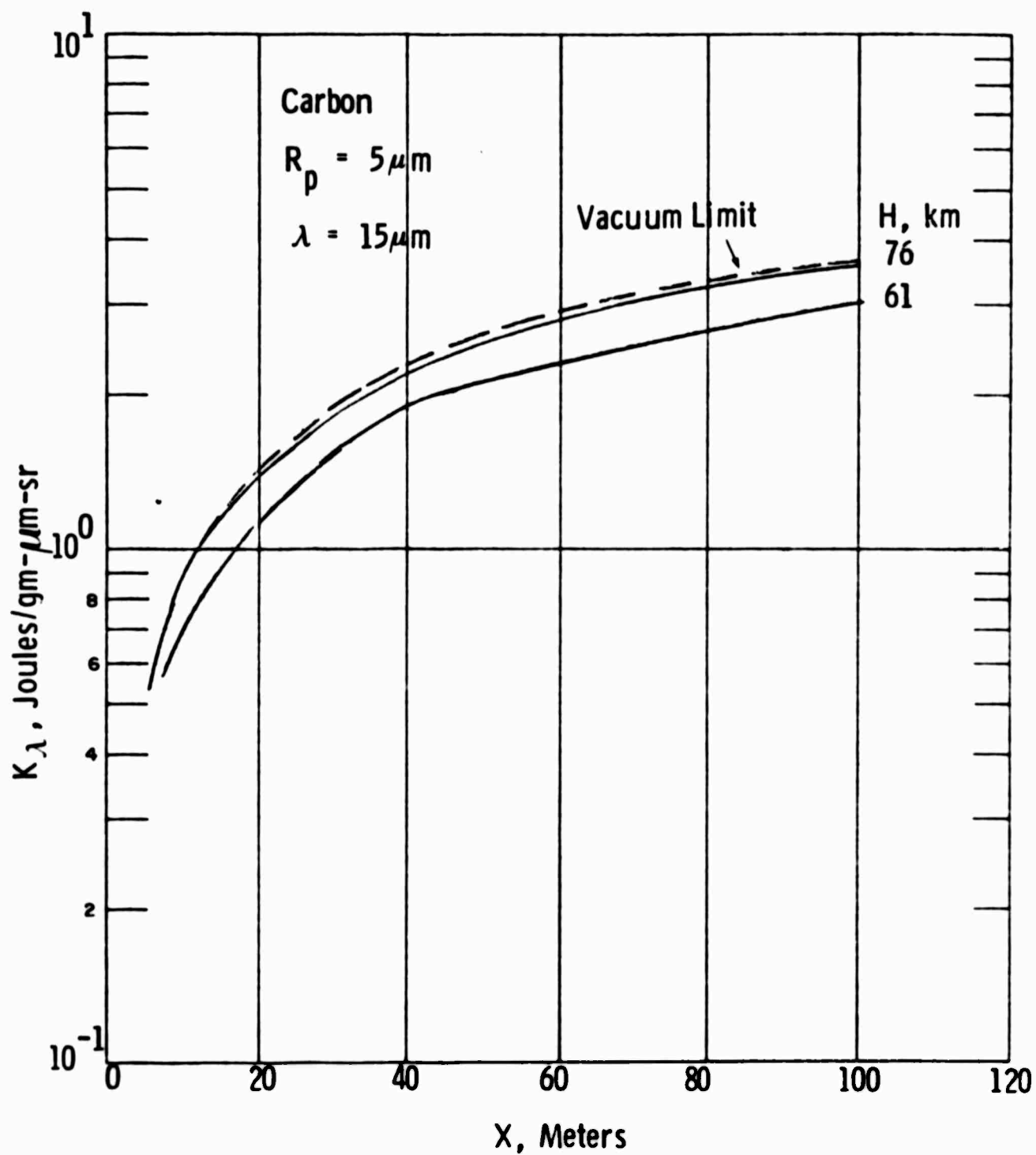
Fig. 32   Integrated Carbon Particle Radiation Per Unit Mass Flow vs. Distance, λ = 15 μm
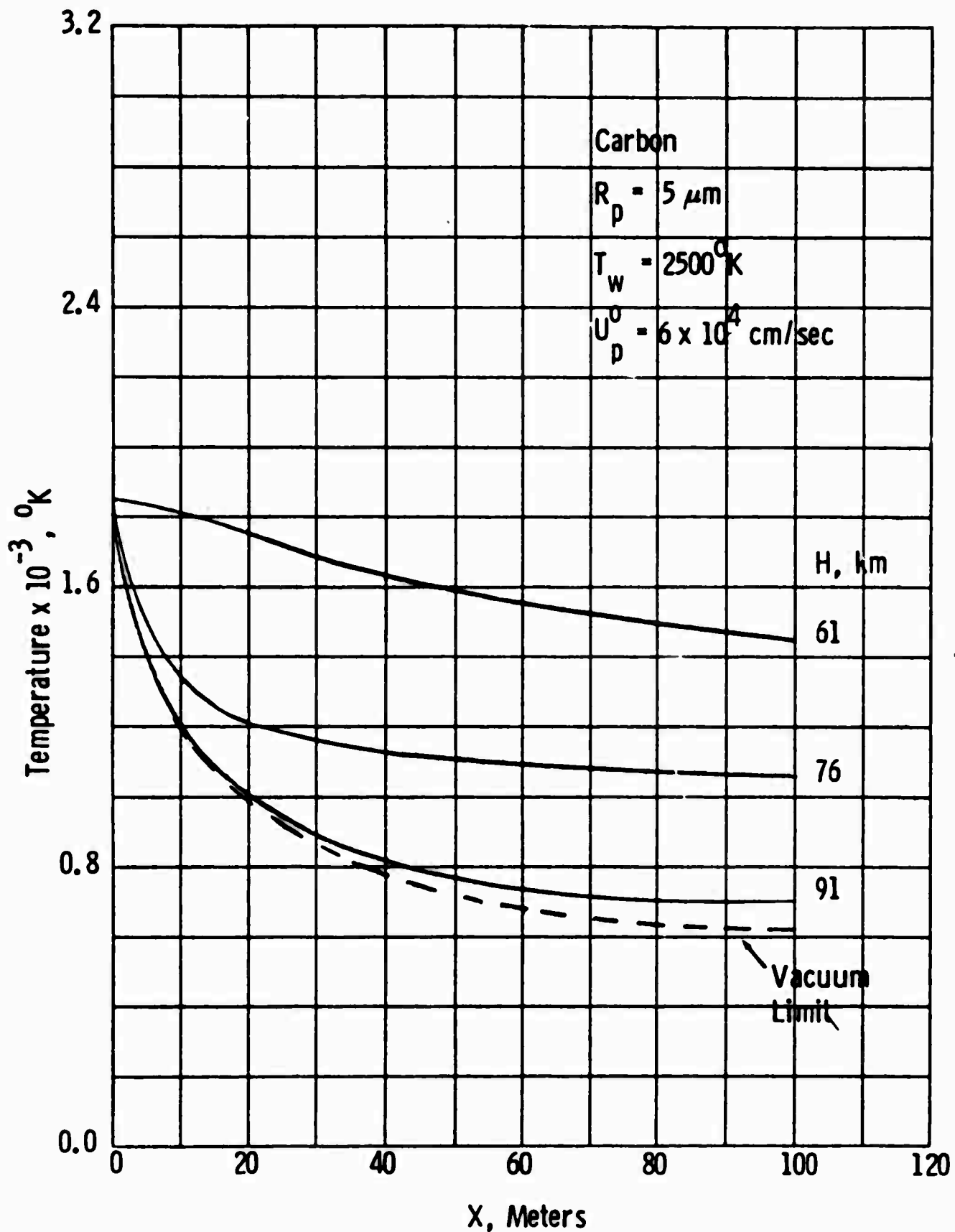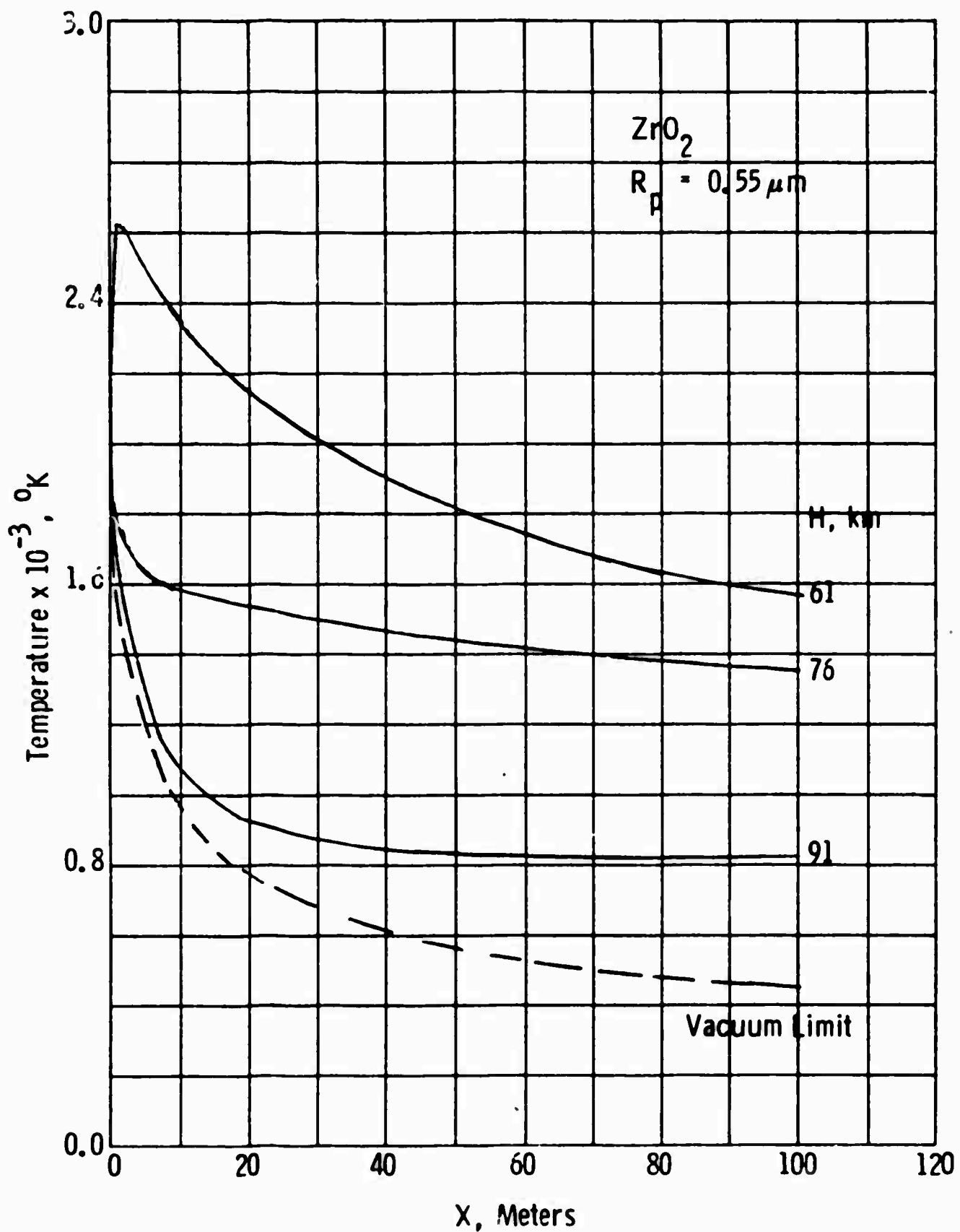
Fig. 33   Predicted Zirconia Particle Temperature vs. Distance at
Several Altitudes
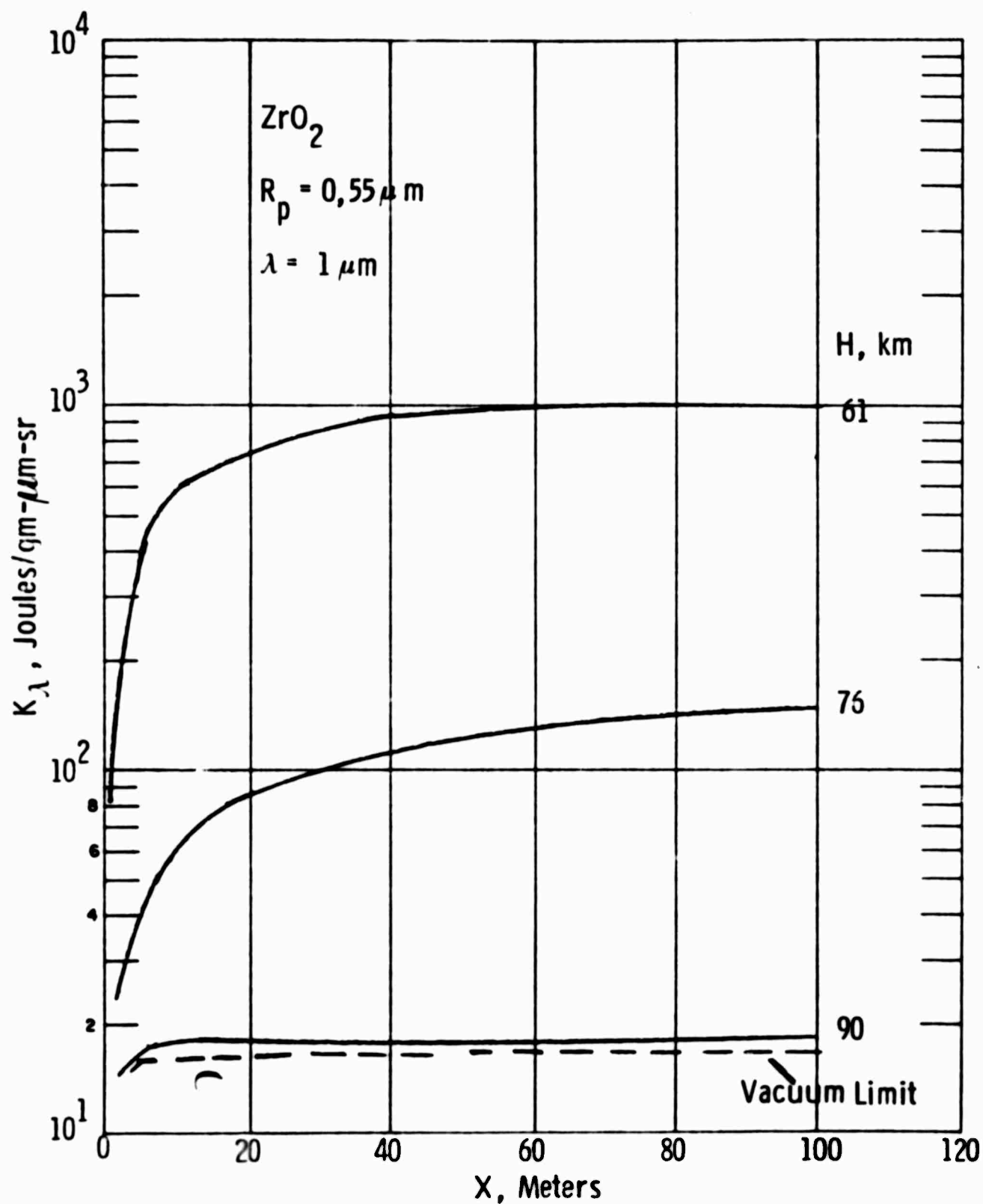
Fig. 34   Integrated Zirconia Particle Radiation Per Unit Mass Flow
vs. Distance, $\lambda = 1\,\mu m$
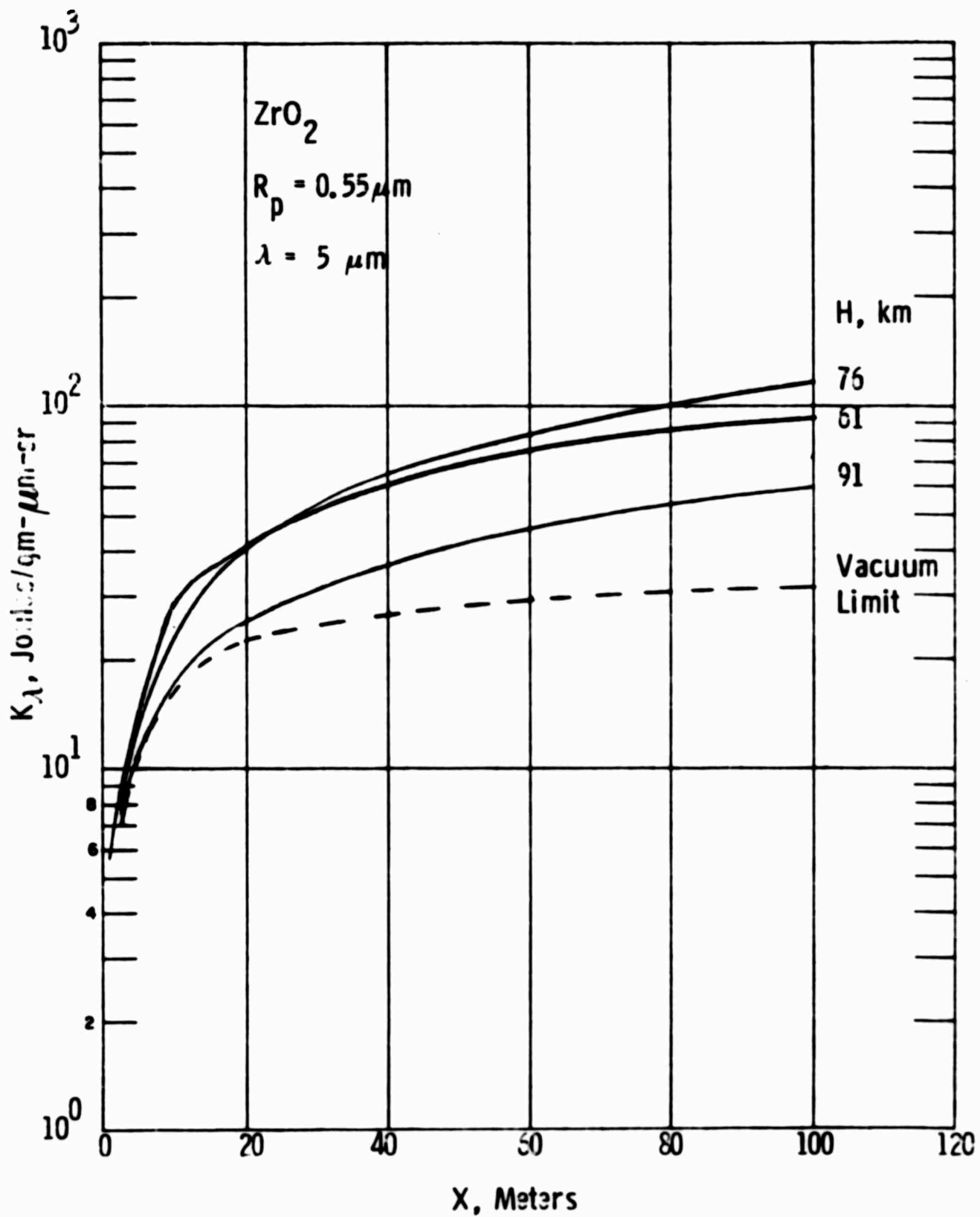
Fig. 35 Integrated Zirconia Particle Radiation Per Unit Mass Flow
vs. Distance, $\lambda = 5\ \mu m$

It should be noted that these radiation predictions can be provided for any wavelength and/or bandpass. In particular predictions for the bandpasses corresponding to atmospheric windows may be of interest for systems applications. As a specific example the predicted total normalized ZrO_2 particle radiation for the 3-5 um wavelength region is shown in Fig. 36 for both an altitude of 61 km and the vacuum limit. The radiation enhancement factor for this case is approximately a factor of five, somewhat higher than that shown for 5 um in Fig. 35 because of the increasing radiation enhancement with decreasing wavelength.

D.   Discussion and Conclusions

In summary it has been demonstrated in the spoofing analysis that, given the proper choice of particle material and size, significant infrared signatures can be produced in the near wake of a re-entry vehicle through the mechanism of introducing cold particles into the flow. These particles which are initially injected at or near the body velocity (in ground based coordinates) are heated through decelerating collisions with the wake molecules. Many materials are available which exhibit very structured molecular-like spectra in the infrared. Unfortunately, the information required to define optimum materials for specific applications is not generally available.

In the case of the masking predictions it has been demonstrated that there can be a significant enhancement in the IR radiation signatures from PCM generated particles when endo-atmospheric effects become important. The level of radiation enhancement is both altitude and wavelength dependent and is most prominent in the near infrared. The particle properties required for optimal radiation enhancement have not yet been defined.

In extrapolating the results of this modeling effort to particular systems there is one limitation which must be considered, dealing with
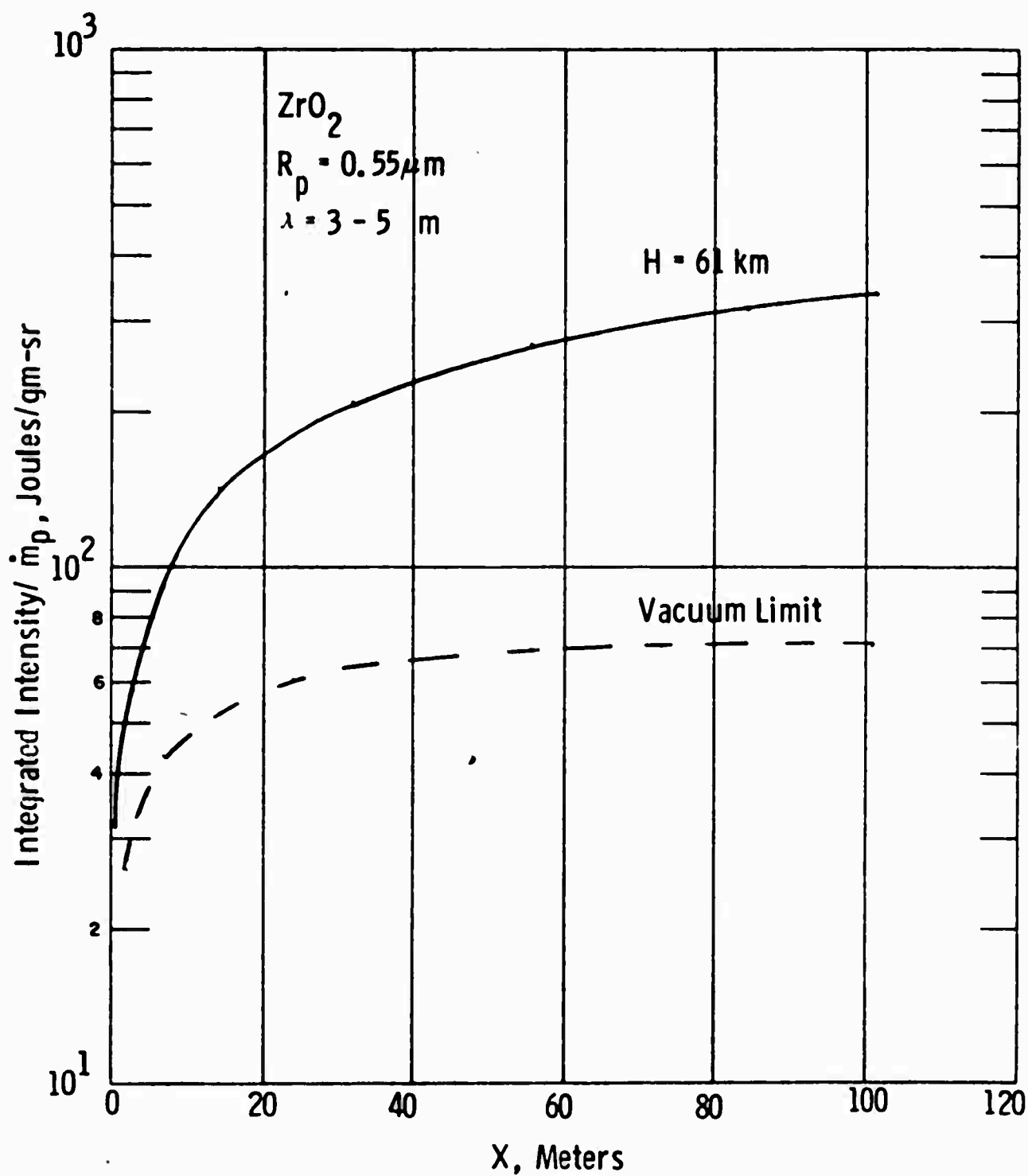
Fig. 36   Integrated Zirconia Particle Radiation Per Unit Mass Flow
vs. Distance, $\lambda = 3 - 5 \mu m$

the total particulate mass flow required to produce a desired radiation intensity. The model used in this work assumes that the wake may be treated as a constant bath. However, the particles initially have a high kinetic energy and it can be shown that $> 75\%$ of this energy is transferred to the wake molecules with the remainder being dissipated among radiation and vaporization losses and the sensible heat content of the particles. Thus, if the particle mass flow rate is such that the initial particulate enthalpy flow is of the same order or greater than the wake molecular enthalpy flow the particle/gas interaction could produce a significant perturbation on wake temperature and velocity. Although this effect would not invalidate the basic heating/radiation phenomenology described in this work it could provide for a variation in radiation per unit mass as a function of $\dot{m}_p$.

IV. ACKNOWLEDGEMENTS

V. REFERENCES

1. S. Glickler, L. Popper, K. Wray and L. Young, "Modeling and Radiation Predictions", in AVCO Everett Research Lab. Final Report, "Infrared Radiation Sources (U)", SAMSO-TR-71-270, June 1971 (SECRET).

2. G. E. Caledonia and R. Sheppard, Jr., "Prediction of Non-Equilibrium IR Radiation from Teflon/Carbon Phenolic Contaminated Wakes", in AVCO Everett Research Lab. REP Final Technical Progress Report, SAMSO-TR-73-282, July 1973 (SECRET).

3. S. L. Glickler, "Documentation of Wake Computer Codes", in AVCO Everett Research Lab. REP Final Technical Progress Report, Contract F04701-74-C-0319, to be published, 1975.

4. F. H. Hals and P. F. Lewis, "Control Techniques for Nitrogen Oxides in MHD Power Plants", in Proceedings of the 12th Symposium, Engineering aspects of Magnetohydrodynamics, Argonne, Illinois, 1972.

5. P. F. Lewis, "The Forward Marching Solution of Coupled Differential Equations, Physical Sciences Inc. Report TR-19, February 1975.

6. P. F. Lewis and D. W. Trainor, "Survey of Vibrational Relaxation Data for O_2, N_2, H_2, CO, HF, HCl, CO_2 and H_2O, AVCO Everett Research Lab. AMP 422, November 1974.

7. R. L. Taylor, "Energy Transfer Processes in the Stratosphere", Can. J. Chem. 52, 1436 (1974).

8. S. N. Suchard, R. L. Kerber, G. Emanuel and J. S. Whittier, "Effect of H_2 Pressure on Pulsed H_2 and F_2 Laser Experiment and Theory", J. Chem. Phys., 57, 5065 (1972).

9. S. L. Valley, ed., "Handbook of Geophysics and Space Environments", McGraw-Hill Book Co., New York, N.Y., 1965.

10. C. duP. Donaldson and K. E. Gray, "Theoretical and Experimental Investigation of the Compressible Free Mixing of Two Dissimilar Gases," AIAA J. 4, 2017 (1966).

11. G. E. Caledonia, "Infrared Signature Modifications, Vol. II (U)", Physical Sciences Inc. TR-49, March 1976 (SECRET).

12. R. F. Probstein, "Shock Wave and Flow Field Development in Hypersonic Re-entry", Amer. Rock. Soc. J. 31, 185 (1961).

Preceding page blank

References (Cont'd)

13.   S. A. Schaaf and P. L. Chambre, "Flow of Rarefied Gases", in "Funda-
      mentals of Gas Dynamics", H. W. Emmons, Ed., Sec. H, (Vol. III of
      "High Speed Aerodynamics and Jet Propulsion"), Princeton University
      Press, Princeton, 1958, pp. 687-739.

14.   G. Gal and H. Kirch, "Particulate Optical Properties in Rocket Plumes",
      Lockheed Palo Alto Research Lab. Report AFRPL-TR-73-99, November
      1973.

15.   J. R. Steyer, K. L. Day and D. R. Huffman, "Infrared Absorption by
      Small Amorphous Quartz Spheres", App. Opt. 13, 1586 (1974).

16.   V. R. Stull and G. N. J. Plass, "Emissivity of Dispersed Carbon Particles",
      J. Opt. Soc. Amer. 50, 121 (1960).

17.   D. R. Stull and H. Prophet, Eds., "JANAF Thermochemical Tables",
      2nd Edition, U. S. Dept. of Commerce NSRDS-NBS37, Washington, D. C.

18.   S. Glasstone, "Thermodynamics for Chemists", D. Van Nostrand Co.,
      New York, N. Y., (1950).

APPENDIX A

CHEMICAL/VIBRATIONAL KINETIC PACKAGE

The chemical/vibrational kinetic scheme employed in the calculations is listed on the following pages. With the exception of OH, NO and F_2, each of the important vibrational modes of a molecule were carried as distinct species. The code used in designating those species is listed in Table I.

It will be noted that in several cases a specific reaction will be listed twice. In these instances the total rate constant for the reaction is the sum of the two listed rate constants. All rate constants are specified in units of cm^3/sec or cm^6/sec^{-1}. The rates for spontaneous radiation are listed in units of sec^{-1}.

TABLE I

SPECIES DESIGNATION CODE

	CODE NAME	SPECIES
1	CO	CO $(v = 0)$
2	CO^*	CO $(v = 1)$
3	H_2	H_2 $(v = 0)$
4	H_2^*	H_2 $(v = 1)$
5	HF	HF $(v = 0)$
6	HF^*	HF $(v = 1)$
7	N_2	N_2 $(v = 0)$
8	N_2^*	N_2 $(v = 1)$
9	O_2	O_2 $(v = 0)$
10	O_2^*	O_2 $(v = 1)$
11	C000	CO_2 (000)
12	C100	CO_2 (100)
13	C010	CO_2 (010)
14	C020	CO_2 (020)
15	C030	CO_2 (030)
16	C001	CO_2 (001)
17	H000	H_2O (000)
18	H100	H_2O (100)
19	H010	H_2O (010)
20	H020	H_2O (020)
21	H001	H_2O (001)

TABLE II

Vibrational Kinetics $k = AT^B \exp(C/T + D/T^{1/3} + E/T^{2/3})$

	REACTION	A	B	C	D	E
1.	$CO^* + CO \rightleftarrows CO + CO$	6.67×10^{-8}	0	0	-208.3	0
2.	$N_2 + N_2 \rightleftarrows N_2 + N_2$	1.00×10^{-20}	0	0	0	0
3.	$CO^* + O_2 \rightleftarrows CO + O_2$	6.67×10^{-8}	0	0	-208.3	0
4.	$CO^* + N_2 \rightleftarrows CO + N_2$	6.67×10^{-8}	0	0	-208.3	0
5.	$CO^* + H_2 \rightleftarrows CO + H_2$	9.00×10^{-9}	0	0	-118.8	0
6.	$CO^* + H000 \rightleftarrows CO + H000$	2.55×10^{-10}	0	0	-32.4	0
7.	$CO^* + H \rightleftarrows CO + H$	1.80×10^{-3}	0	0	-208.3	0
8.	$CO^* + O \rightleftarrows CO + O$	2.70×10^{-9}	0	0	-69.7	0
9.	$CO^* + F \rightleftarrows CO + F$	5.05×10^{-9}	0	0	-95.91	0
10.	$N_2^* + N_2 \rightleftarrows N_2 + N_2$	8.53×10^{-7}	0	0	-273.1	0
11.	$N_2^* + O_2 \rightleftarrows N_2 + O_2$	8.53×10^{-7}	0	0	-273.1	0
12.	$N_2^* + CO \rightleftarrows N_2 + CO$	8.53×10^{-7}	0	0	-273.1	0
13.	$N_2^* + H_2 \rightleftarrows N_2 + H_2$	3.92×10^{-8}	0	0	-164.2	0
14.	$N_2^* + O \rightleftarrows N_2 + O$	1.10×10^{-10}	0	0	-69.9	0
15.	$N_2^* + F \rightleftarrows N_2 + F$	5.50×10^{-11}	0	0	-69.9	0
16.	$N_2^* + H000 \rightleftarrows N_2 + H000$	1.10×10^{-10}	0	0	-69.9	0
17.	$O_2^* + O_2 \rightleftarrows O_2 + O_2$	1.20×10^{-9}	0	0	-133.1	0
18.	$O_2^* + N_2 \rightleftarrows O_2 + N_2$	4.81×10^{-8}	0	0	-169.6	0
19.	$O_2^* + CO \rightleftarrows O_2 + CO$	4.81×10^{-8}	0	0	-169.6	0
20.	$O_2^* + H_2 \rightleftarrows O_2 + H_2$	1.30×10^{-9}	0	0	-76.8	0
21.	$O_2^* + H000 \rightleftarrows O_2 + H000$	4.10×10^{-9}	0	0	-76.8	0
22.	$O_2^* + O \rightleftarrows O_2 + O$	4.50×10^{-15}	0.5	0	0	0
23.	$O_2^* + F \rightleftarrows O_2 + F$	2.20×10^{-15}	0.5	0	0	0
24.	$H_2^* + H_2 \rightleftarrows H_2 + H_2$	2.20×10^{-9}	0	0	-118.9	0

TABLE II (Cont'd)

	REACTION	A	B	C	D	E
25.	$H_2^* + H \rightleftarrows H_2 + H$	1.70×10^{-14}	0.5	0	0	0
26.	$H_2^* + N_2 \rightleftarrows H_2 + N_2$	8.60×10^{-9}	0	0	-148.4	0
27.	$H_2^* + H000 \rightleftarrows H_2 + H000$	1.70×10^{-15}	0.5	0	0	0
28.	$H010 + H000 \rightleftarrows H000 + H000$	1.60×10^{-12}	0.5	0	0	0
29.	$H020 + H000 \rightleftarrows H010 + H000$	3.20×10^{-12}	0.5	0	0	0
30.	$H010 + O \rightleftarrows H000 + O$	1.00×10^{-11}	0.5	0	0	0
31.	$H010 + F \rightleftarrows H000 + F$	5.00×10^{-12}	0.5	0	0	0
32.	$H020 + O \rightleftarrows H010 + O$	2.00×10^{-11}	0.5	0	0	0
33.	$H020 + F \rightleftarrows H010 + F$	1.00×10^{-11}	0.5	0	0	0
34.	$H010 + H \rightleftarrows H000 + H$	1.00×10^{-11}	0.5	0	0	0
35.	$H020 + H \rightleftarrows H010 + H$	2.00×10^{-11}	0.5	0	0	0
36.	$H010 + N_2 \rightleftarrows H000 + N_2$	4.80×10^{-11}	0	0	-43.0	0
37.	$H020 + N_2 \rightleftarrows H010 + N_2$	9.60×10^{-11}	0	0	-43.0	0
38.	$C010 + C000 \rightleftarrows C000 + C000$	4.64×10^{-10}	0	0	-76.75	0
39.	$C020 + C000 \rightleftarrows C010 + C000$	9.28×10^{-10}	0	0	-76.75	0
40.	$C030 + C000 \rightleftarrows C020 + C000$	1.39×10^{-9}	0	0	-76.75	0
41.	$C010 + N_2 \rightleftarrows C000 + N_2$	6.69×10^{-10}	0	0	-84.07	0
42.	$C020 + N_2 \rightleftarrows C010 + N_2$	1.34×10^{-9}	0	0	-84.07	0
43.	$C030 + N_2 \rightleftarrows C020 + N_2$	2.01×10^{-9}	0	0	-84.07	0
44.	$C010 + O_2 \rightleftarrows C000 + O_2$	6.69×10^{-10}	0	0	-84.07	0
45.	$C020 + O_2 \rightleftarrows C010 + O_2$	1.34×10^{-9}	0	0	-84.07	0
46.	$C030 + O_2 \rightleftarrows C020 + O_2$	2.01×10^{-9}	0	0	-84.07	0
47.	$C010 + H000 \rightleftarrows C000 + H000$	3.22×10^{-13}	0	0	22.91	0
48.	$C020 + H000 \rightleftarrows C010 + H000$	6.44×10^{-13}	0	0	22.91	0
49.	$C030 + H000 \rightleftarrows C020 + H000$	9.66×10^{-13}	0	0	22.91	0

TABLE II (Cont'd)

	REACTION	A	B	C	D	E
50.	$C010 \cdot H_2 \rightleftarrows C000 \cdot H_2$	7.60×10^{-12}	0	0	-7.13	0
51.	$C020 \cdot H_2 \rightleftarrows C010 \cdot H_2$	1.52×10^{-11}	0	0	-7.13	0
52.	$C030 \cdot H_2 \rightleftarrows C020 \cdot H_2$	2.28×10^{-11}	0	0	-7.13	0
53.	$C010 \cdot O \rightleftarrows C000 \cdot O$	2.32×10^{-9}	0	0	-76.75	0
54.	$C010 \cdot F \rightleftarrows C000 \cdot F$	1.16×10^{-9}	0	0	-76.75	0
55.	$C020 \cdot O \rightleftarrows C010 \cdot O$	4.64×10^{-9}	0	0	-76.75	0
56.	$C020 \cdot F \rightleftarrows C010 \cdot F$	2.32×10^{-9}	0	0	-76.75	0
57.	$C030 \cdot O \rightleftarrows C020 \cdot O$	6.96×10^{-9}	0	0	-76.75	0
58.	$C030 \cdot F \rightleftarrows C020 \cdot F$	3.48×10^{-9}	0	0	-76.75	0
59.	$C010 \cdot CO \rightleftarrows C000 \cdot CO$	6.69×10^{-10}	0	0	-84.07	0
60.	$C020 \cdot CO \rightleftarrows C010 \cdot CO$	1.34×10^{-9}	0	0	-84.07	0
61.	$C030 \cdot CO \rightleftarrows C020 \cdot CO$	2.01×10^{-9}	0	0	-84.07	0
62.	$HF^* \cdot HF \rightleftarrows HF \cdot HF$	1.30×10^{-12}	0	0	0	0
63.	$HF^* \cdot HF \rightleftarrows HF \cdot HF$	2.00×10^{-8}	0	0	-121.81	0
64.	$HF^* \cdot N_2 \rightleftarrows HF \cdot N_2$	1.24×10^{-11}	0	0	-57.56	0
65.	$HF^* \cdot O_2 \rightleftarrows HF \cdot O_2$	2.08×10^{-11}	0	0	-68.02	0
66.	$HF^* \cdot NO \rightleftarrows HF \cdot NO$	1.20×10^{-10}	0	0	-60.20	0
67.	$HF^* \cdot F \rightleftarrows HF \cdot F$	1.40×10^{-8}	0	0	-70.88	0
68.	$H010 \cdot O_2 \rightleftarrows O_2^* \cdot H000$	1.00×10^{-12}	0	0	0	0
69.	$C001 \cdot CO \rightleftarrows CO^* \cdot C000$	1.56×10^{-11}	0	0	-30.12	0
70.	$N_2^* \cdot O_2 \rightleftarrows O_2^* \cdot N_2$	1.74×10^{-10}	0	0	-124.00	0
71.	$C001 \cdot N_2 \rightleftarrows N_2^* \cdot C000$	1.71×10^{-6}	0	0	-175.30	0
72.	$C001 \cdot N_2 \rightleftarrows N_2^* \cdot C000$	6.07×10^{-14}	0	0	15.27	0
73.	$N_2^* \cdot CO \rightleftarrows CO^* \cdot N_2$	1.78×10^{-6}	0	0	-209.90	0
74.	$N_2^* \cdot CO \rightleftarrows CO^* \cdot N_2$	6.98×10^{-13}	0	0	-25.60	0

TABLE II (Cont'd)

	REACTION	A	B	C	D	E
75.	$CO \cdot O_2 \rightleftarrows O_2 \cdot CO$	1.00×10^{-10}	0	0	-104.00	0
76.	$H_2 \cdot H000 \rightleftarrows H001 \cdot H_2$	1.67×10^{-19}	2.00	0	0	0
77.	$H_2 \cdot H000 \rightleftarrows H100 \cdot H_2$	1.67×10^{-19}	2.00	0	0	0
78.	$O_2 \cdot C000 \rightleftarrows O_2 \cdot C020$	1.40×10^{-18}	1.50	0	0	0
79.	$H_2 \cdot HF \rightleftarrows H_2 \cdot HF$	1.50×10^{-12}	0	0	0	0
80.	$HF \cdot C000 \rightleftarrows C001 \cdot HF$	1.20×10^{-12}	0	0	0	0
81.	$HF \cdot H000 \rightleftarrows HF \cdot H001$	5.00×10^{-11}	0	0	0	0
82.	$C001 \cdot H000 \rightleftarrows C030 \cdot H000$	4.71×10^{-40}	4.54	2082.	454.06	-1729.2
83.	$C001 \cdot H_2 \rightleftarrows C030 \cdot H_2$	4.27×10^{17}	-6.34	-3013.	-378.66	1415.8
84.	$C001 \cdot N_2 \rightleftarrows C030 \cdot N_2$	4.12×10^{23}	-5.89	-4223.	-672.67	2682.9
85.	$C001 \cdot O_2 \rightleftarrows C030 \cdot O_2$	4.12×10^{23}	-5.89	-4223.	-672.67	2682.9
86.	$C001 \cdot CO \rightleftarrows C030 \cdot CO$	6.87×10^{23}	-5.89	-4223.	-672.67	2682.9
87.	$C001 \cdot C000 \rightleftarrows C030 \cdot C000$	9.16×10^{23}	-5.89	-4223.	-672.67	2682.9
88.	$C001 \cdot O \rightleftarrows C030 \cdot O$	1.20×10^{-14}	0.50	0	0	0
89.	$C001 \cdot F \rightleftarrows C030 \cdot F$	1.90×10^{-13}	0.50	0	0	0
90.	$C001 \cdot H \rightleftarrows C030 \cdot H$	6.00×10^{-15}	0.50	0	0	0
91.	$C001 \cdot HF \rightleftarrows C030 \cdot HF$	4.00×10^{-13}	0	0	0	0
92.	$H100 \cdot H000 \rightleftarrows H020 \cdot H000$	1.60×10^{-12}	0.50	0	0	0
93.	$H001 \cdot H000 \rightleftarrows H020 \cdot H000$	1.60×10^{-12}	0.50	0	0	0
94.	$H100 \cdot O \rightleftarrows H020 \cdot O$	1.00×10^{-11}	0.50	0	0	0
95.	$H100 \cdot F \rightleftarrows H020 \cdot F$	5.00×10^{-12}	0.50	0	0	0
96.	$H001 \cdot O \rightleftarrows H020 \cdot O$	1.00×10^{-11}	0.50	0	0	0
97.	$H001 \cdot F \rightleftarrows H020 \cdot F$	5.00×10^{-12}	0.50	0	0	0
98.	$H100 \cdot H \rightleftarrows H020 \cdot H$	2.00×10^{-11}	0.50	0	0	0
99.	$H001 \cdot H \rightleftarrows H020 \cdot H$	2.00×10^{-11}	0.50	0	0	0

TABLE II (Cont'd)

	REACTION	A	B	C	D	E
100.	$H020 \cdot H000 \rightleftharpoons H010 \cdot H010$	1.00×10^{-12}	0.50	0	0	0
101.	$H100 \cdot N_2 \rightleftharpoons H020 \cdot N_2$	4.80×10^{-11}	0	0	-43.00	0
102.	$H100 \cdot M \rightleftharpoons H001 \cdot M$	1.00×10^{-12}	0.50	0	0	0
103.	$H001 \cdot N_2 \rightleftharpoons H020 \cdot N_2$	4.80×10^{-11}	0	0	-43.00	0
104.	$C100 \cdot M \rightleftharpoons C020 \cdot M$	1.80×10^{-12}	0.50	0	0	0
105.	$C030 \cdot C000 \rightleftharpoons C020 \cdot C010$	6.00×10^{-13}	0.50	0	0	0
106.	$C020 \cdot C000 \rightleftharpoons C010 \cdot C010$	4.00×10^{-13}	0.50	0	0	0
107.	$C030 \cdot C010 \rightleftharpoons C020 \cdot C020$	1.20×10^{-12}	0.50	0	0	0

TABLE III

Spontaneous Radiative Decay

	REACTION	$A_{v \to 1}$, sec^{-1}
1.	$CO^a \to CO \cdot h\nu$	3.03×10^1
2.	$C001 \to C000 \cdot h\nu$	3.92×10^2
3.	$C010 \to C000 \cdot h\nu$	1.55×10^0
4.	$C020 \to C010 \cdot h\nu$	3.10×10^0
5.	$C030 \to C020 \cdot h\nu$	4.65×10^0
6.	$H010 \to H000 \cdot h\nu$	2.24×10^1
7.	$H020 \to H010 \cdot h\nu$	4.45×10^1
8.	$H100 \to H000 \cdot h\nu$	3.55×10^1
9.	$H001 \to H000 \cdot h\nu$	3.55×10^1
10.	$HF^a \to HF \cdot h\nu$	2.00×10^2

TABLE IV

Chemical Kinetics $k = AT^B \exp(C/T)$

	REACTION	A	B	C
1.	$O \cdot O \cdot O_2 \rightleftarrows O_2 \cdot O_2$	3.0×10^{-30}	-1.0	0
2.	$O \cdot O \cdot O_2 \rightleftarrows O_2 \cdot O_2$	3.00×10^{-30}	-1.0	-2240
3.	$C \cdot O \cdot N_2 \rightleftarrows O_2 \cdot N_2$	7.50×10^{-31}	-1.0	0
4.	$O \cdot O \cdot N_2 \rightleftarrows O_2 \cdot N_2$	7.50×10^{-31}	-1.0	-2240
5.	$CO \cdot OH \rightleftarrows C000 \cdot H$	6.00×10^{-12}	-0.5	-300
6.	$CO \cdot OH \rightleftarrows C001 \cdot H$	6.00×10^{-12}	-0.5	-3680
7.	$CO \cdot OH \rightleftarrows C100 \cdot H$	6.00×10^{-12}	-0.5	-2300
8.	$CO \cdot OH \rightleftarrows C010 \cdot H$	1.20×10^{-11}	-0.5	-1260
9.	$CO \cdot OH \rightleftarrows C020 \cdot H$	1.20×10^{-11}	-0.5	-2180
10.	$CO \cdot OH \rightleftarrows C030 \cdot H$	1.20×10^{-11}	-0.5	-3080
11.	$CO \cdot OH \rightleftarrows C000 \cdot H$	6.00×10^{-12}	-0.5	-300
12.	$CO \cdot OH \rightleftarrows C001 \cdot H$	6.00×10^{-12}	-0.5	-3680
13.	$CO \cdot OH \rightleftarrows C100 \cdot H$	6.00×10^{-12}	-0.5	-2300
14.	$CO \cdot OH \rightleftarrows C010 \cdot H$	1.20×10^{-11}	-0.5	-1260
15.	$CO \cdot OH \rightleftarrows C020 \cdot H$	1.20×10^{-11}	-0.5	-2180
16.	$CO^* \cdot OH \rightleftarrows C030 \cdot H$	1.20×10^{-11}	-0.5	-3080
17.	$O \cdot CO \cdot M \rightleftarrows C000 \cdot M$	3.00×10^{-33}	0	-2170
18.	$O \cdot CO \cdot M \rightleftarrows C001 \cdot M$	3.00×10^{-33}	0	-2170
19.	$H \cdot H \cdot M \rightleftarrows H_2 \cdot M$	2.50×10^{-30}	-1.0	0
20.	$H \cdot H \cdot M \rightleftarrows H_2 \cdot M$	2.50×10^{-30}	-1.0	-6000
21.	$H \cdot OH \rightleftarrows H_2 \cdot O$	1.40×10^{-14}	1.0	-3500
22.	$H \cdot OH \rightleftarrows H_2^* \cdot O$	1.40×10^{-14}	1.0	-9500

TABLE IV (Cont'd)

	REACTION	A	B	C
23.	$H_2 + OH \rightleftarrows H000 + H$	6.00×10^{-11}	0	-2600
24.	$H_2 + OH \rightleftarrows H010 + H$	6.00×10^{-11}	0	-4900
25.	$H_2 + OH \rightleftarrows H020 + H$	6.00×10^{-11}	0	-9400
26.	$H_2^* + OH \rightleftarrows H000 + H$	6.00×10^{-11}	0	-2600
27.	$H_2^* + OH \rightleftarrows H010 + H$	6.00×10^{-11}	0	-4900
28.	$H_2^* + OH \rightleftarrows H020 + H$	6.00×10^{-11}	0	-9400
29.	$OH + OH \rightleftarrows H000 + O$	8.20×10^{-11}	-0.33	-550
30.	$OH + OH \rightleftarrows H010 + O$	8.20×10^{-11}	-0.33	-2850
31.	$OH + OH \rightleftarrows H020 + O$	8.20×10^{-11}	-0.33	-5000
32.	$OH + OH \rightleftarrows H100 + O$	8.20×10^{-11}	-0.33	-5800
33.	$OH + OH \rightleftarrows H001 + O$	8.20×10^{-11}	-0.33	-5950
34.	$H + OH + M \rightleftarrows H000 + M$	6.70×10^{-26}	-2.0	0
35.	$H + O_2 \rightleftarrows O_2 + OH$	3.70×10^{-10}	0	-8450
36.	$H + O_2^* \rightleftarrows O + OH$	3.70×10^{-10}	0	-8450
37.	$F + H_2 \rightleftarrows HF^* + H$	2.60×10^{-10}	0	-800
38.	$H + F_2 \rightleftarrows HF^* + F$	2.20×10^{-10}	0	-1200
39.	$F_2 + M \rightleftarrows F + F + M$	8.30×10^{-11}	0	-17600
40.	$HF + M \rightleftarrows H + F + M$	1.80×10^{-5}	-1.0	-67500

END